Fakultät für Mathematik und Naturwissenschaften

RWTH AACHEN UNIVERSITY

Altered podocyte compartmentalization as a pathomechanism driving focal segmental glomerulosclerosis

Von der Fakultät für Mathematik und Naturwissenschaften
der RWTH Aachen University zur Erlangung des akademischen Grades
einer Doktorin der Naturwissenschaften genehmigte Dissertation

vorgelegt von

Yingying Gao, Master of Science

aus
Zibo, China

Berichter: Prof. Dr. rer. nat. Tammo Ostendorf
Univ. Prof. Dr. phil. nat. Gabriele Pradel

Tag der mündlichen Prüfung: 01.06.2026

Diese Dissertation ist auf den Internetseiten der Universitätsbibliothek verfügbar.

Content

Table of Content 1
Summary 5
Zusammenfassung 6
List of Abbreviations 7
List of Figures 12
List of Tables 14
1 Introduction 15
1.1 Podocyte Injury in Glomerular Diseases 15
1.2 Focal Segmental Glomerulosclerosis (FSGS) 17
1.2.1 Mechanisms of Sclerotic Lesion Development in FSGS 17
1.2.2 Classification of FSGS 18
1.2.2.1 Classification Based on Etiology of Podocyte Injury 18
1.2.2.2 Columbia Classification System 19
1.2.3 Treatment of FSGS 20
1.3 Available FSGS Animal Models 21
1.3.1 Renal Ablation Model 21
1.3.2 Chemical or Toxin-Induced Models 21
1.3.3 Genetically Engineered Models 21
1.3.4 Models with spontaneous FSGS 22
1.4 The Nuclear Pore Complex 23
1.5 Nuclear Pore Complex Defects and Diseases 26
1.5.1 NPCs in Embryonic Development 26
1.5.2 NPCs in Neurological Disorders 26
1.5.3 NPCs in Cancer Development and Progression 26
1.5.4 NPCs in Viral Infection 27

1.5.5 NPCs in Kidney Diseases: Focus on FSGS 28
1.6 Aim of This Work 29
2 Materials 31
2.1 Devices 31
2.2 Consumables 32
2.3 Reagents 33
2.4 Kits 36
2.5 Antibodies 36
2.5.1 Primary Antibodies 36
2.5.2 Secondary Antibodies 38
2.6 Software 39
2.7 Pod-rtTA/histone-eGFP Mouse Line 39
2.8 Munich Wistar Froemter (MWF) Rats 40
3. Methods 41
3.1 Procedures Common to Mouse and Rat Experiments 41
3.1.1 Animal Husbandry and Care 41
3.1.2 Animal Anesthesia 41
3.1.3 Paraffin Tissue Block Preparation 41
3.2 Mouse Experiments 41
3.2.1 Kidney Tissue Clearing and 3D Imaging 41
3.2.2 Histochemistry and Immunofluorescence 42
3.2.3 Labeling of Podocytes 43
3.2.4 Isolation of Primary Podocytes from Pod-rtTA/Histone-eGFP Mice at Different Ages 43
3.2.5 Nuclear and Cytoplasmic Protein Extraction 45
3.2.6 Protein Concentration Measurement 46
3.2.7 Western Blot 47

3.2.8 Mass Spectrometry Analysis of Different Protein Fractions.....48
3.3 Rat Experiments.....49
3.3.1 *In Vitro* Drug Testing.....49
3.3.1.1 Cell Culture, Plasmids and siRNA Transfection.....49
3.3.1.2 Western Blot.....49
3.3.2 *In Vivo* Intervention in an FSGS Rat Model by Using the Nuclear Transport Inhibitor KPT-330.....50
3.3.3 Serum and Urine Collection, Biochemical Analyses, and Blood Pressure Monitoring.....52
3.3.4 Histochemistry, Immunohistochemistry and Immunofluorescence.....53
3.3.5 Microscopy and Image Analyses.....54
3.4 Statistical Analysis.....56
4 Results.....57
4.1 Characteristics of Aging Mouse Kidneys with a Focus on Mislocalized Podocyte Biomarkers.....57
4.1.1 Structural and Functional Changes in the Aging Kidney.....57
4.1.1.1 Kidney 3D Imaging Reveals a Decrease in Podocyte Number During Aging.....57
4.1.1.2 Mice Develop Age-Related Glomerular Synechiae.....58
4.1.1.3 Kidney Function Declines Slightly with Aging.....59
4.1.2 Identification of Known and Novel Mislocalized Podocyte Biomarkers in Aging Mouse Kidneys.....59
4.1.2.1 Establishment of an Imaging Analysis Work Flow for Calculating Nuclear-to-Cytoplasmic Ratios of Proteins.....59
4.1.2.2 Analysis of Nuclear to Cytoplasmic Intensity Ratio (N/C) of Known Candidate Proteins.....62
4.1.2.3 Screening for Podocyte-Specific Mislocalized Proteins During Aging.....66
4.1.2.3.1 Optimization of the Podocyte Isolation Protocol.....66

4.1.2.3.2 Validation of Nuclear and Cytoplasmic Fractionation from Podocytes of Different Ages 69

4.1.2.3.3 Mass Spectrometry Data 70

4.2 Nuclear Export Inhibitor Selinexor (KPT-330) Improves Kidney Function in a Rat Model of Focal Segmental Glomerulosclerosis 77

4.2.1 Restoration of Impaired NPC Function by KPT-330 *In Vitro* 77

4.2.2 Histological and Functional Characterization of MWF Rats During Aging 78

4.2.3 KPT-330 Alters General Physiological Parameters in MWF Rats 81

4.2.4 KPT-330 Treatment Increases Podocytic NPC Numbers 83

4.2.5 KPT-330 Treatment Promotes Nuclear Retention of XPO1 and P53 85

4.2.6 KPT-330 Treatment Improves Renal Function and Reduces Serum Lipids 87

4.2.7 KPT-330 Does Not Halt FSGS Progression 89

5 Discussion 93

5.1 Aging Predisposes Mice to FSGS-like Pathology and Is Accompanied by Loss of Podocytes 93

5.2 Methodological Considerations for Primary Podocyte Isolation in Aging Research 94

5.3 Age-dependent Remodeling of the Podocyte Spatial Proteome 95

5.4 Proteomic Identification of Podocyte-specific Spatial Remodeling Markers 97

5.5 KPT-330 Enhanced Renal Function in MWF rats but Could Not Halt the Histological Damage Progression in the Current Setting 99

6 Outlook 101

References 105

Appendix 124

Acknowledgments 129

Declaration of Authorship 131

Summary

Focal segmental glomerulosclerosis (FSGS), a major cause of chronic kidney disease, is characterized by podocyte injury and loss. Podocytes are terminally differentiated, post-mitotic cells. Mutations in components of the nuclear pore complex (NPC) in podocytes have previously been associated with the development of FSGS, but detailed mechanistic insights and potential therapeutic implications have remained unclear. This study therefore investigated the hypothesis that age-dependent accumulation of NPC defects, leading to impaired nucleocytoplasmic transport (NCT) in podocytes, contributes to the development of FSGS, particularly in older individuals. The key findings were as follows:

Advancing age in mice was associated with a progressive decline in podocyte number and the appearance of segmental glomerulosclerosis, closely mirroring human age-related glomerular deterioration. Spatial proteomic profiling of nuclear and cytoplasmic fractions from primary podocytes revealed coordinated, age-dependent remodeling of the podocyte spatial proteome. Notable alterations included nuclear accumulation of mitochondrial and redox-associated proteins, together with cytoplasmic displacement of metabolic and structural enzymes. These changes indicate impaired mitochondrial protein import, disturbed mitochondrial-nuclear communication, and altered metabolic compartmentalization as central molecular features of podocyte aging and early contributors to cellular dysfunction.

To assess therapeutic relevance, nuclear export was inhibited using the XPO1 inhibitor selinexor (KPT-330) in the Munich Wistar Frömter rat model of spontaneous FSGS. Short-term treatment improved renal functional markers, including serum creatinine, lipids, and cystatin C, indicating partial restoration of podocyte homeostasis. Despite these benefits, structural glomerular damage continued to progress, indicating that inhibition of nuclear export alone is insufficient to halt chronic podocyte injury under the tested conditions.

Collectively, these findings show how aging reshapes podocyte nuclear-cytoplasmic organization and identify NCT impairment as a potential early driver of podocyte failure. This work provides both mechanistic insight and an experimental foundation for developing future therapeutic strategies that target nuclear transport pathways in age-related glomerular disease and FSGS.

Zusammenfassung

Die fokal-segmentale Glomerulosklerose (FSGS), eine Hauptursache der chronischen Nierenerkrankung, ist durch Schädigung und Verlust von Podozyten gekennzeichnet. Diese terminal differenzierten, postmitotischen Zellen sind essenziell für die glomeruläre Filtrationsbarriere. Mutationen in Komponenten des Kernporenkomplexes (NPC) in Podozyten wurden bereits mit FSGS in Verbindung gebracht, während mechanistische Zusammenhänge und therapeutische Implikationen bislang unzureichend verstanden sind. Ziel dieser Studie war es daher zu untersuchen, ob eine altersabhängige Akkumulation von NPC-Defekten mit gestörtem nukleozytoplasmatischem Transport (NCT) zur FSGS-Entstehung beiträgt, insbesondere im höheren Lebensalter.

In alternden Mäusen zeigte sich ein progressiver Rückgang der Podozytenzahl sowie die Entwicklung einer segmentalen Glomerulosklerose, was die altersassoziierte glomeruläre Degeneration beim Menschen widerspiegelt. Räumlich aufgelöste Proteomanalysen nukleärer und zytoplasmatischer Fraktionen primärer Podozyten zeigten eine koordinierte, altersabhängige Reorganisation des Podozyten-Proteoms. Charakteristisch waren eine nukleäre Akkumulation mitochondrialer und redoxassoziierter Proteine sowie eine Verlagerung metabolischer und struktureller Enzyme in das Zytoplasma. Diese Veränderungen weisen auf eine gestörte mitochondriale Proteinimportmaschinerie, beeinträchtigte mitochondriale–nukleäre Kommunikation und eine veränderte metabolische Kompartimentierung als frühe molekulare Merkmale der Podozytenalterung hin.

Zur Prüfung der therapeutischen Relevanz wurde im Munich-Wistar-Frömter-Rattenmodell der spontanen FSGS der nukleäre Export durch den XPO1-Inhibitor Selinexor gehemmt. Die kurzzeitige Behandlung verbesserte renale Funktionsmarker, konnte jedoch die fortschreitende strukturelle glomeruläre Schädigung nicht verhindern. Insgesamt identifizieren diese Ergebnisse eine Störung des NCT als potenziellen frühen Treiber des altersassoziierten Podozytenversagens und liefern eine Grundlage für zukünftige therapeutische Ansätze bei FSGS.

List of Abbreviations

Aldh7a1	Aldehyde Dehydrogenase 7 Family Member A1
Aldoa	Fructose-Bisphosphate Aldolase A
Aldoc	Fructose-Bisphosphate Aldolase C
Anxa3 / Anxa5 / Anxa6	Annexin A3 / A5 / A6
Atp5if1	ATP Synthase Inhibitory Factor Subunit 1
BRCA1	Breast Cancer Type 1 Susceptibility Protein
BRCA2	Breast Cancer Type 2 Susceptibility Protein
BSA	Bovine serum albumin
BUN	Blood urea nitrogen
C9orf72	Chromosome 9 Open Reading Frame 72
Cap1	Adenylate Cyclase-associated Protein 1
CD44	Cluster of Differentiation 44
Cfl1	Cofilin-1
CKD	Chronic kidney disease
CLC-1	Chloride Voltage-gated Channel 1
Cox5b	Cytochrome c Oxidase Subunit 5B
Cox7c	Cytochrome c Oxidase Subunit 7C
Cre/LacZ	Cre recombinase/LacZ reporter
CRM1	Chromosome maintenance protein 1
DAB	Diaminobenzidine
DAPI	4′,6-Diamidine-2-phenylindole
Dbi	Diazepam-Binding Inhibitor
Dox	Doxycycline
DRG2	Developmentally Regulated GTP-binding protein 2

DTT	Dithiothreitol
EDTA	Ethylenediaminetetraacetic acid
EGTA	Ethylene glycol tetraacetic acid
eIF4E	Eukaryotic initiation factor 4E
FACS	Fluorescence-activated cell sorting
FBS	Fetal bovine serum
FDA	Food and Drug Administration
FDR	False discovery rate
FG	Phenylalanine-glycine (FG repeat nucleoporins)
FSGS	Focal segmental glomerulosclerosis
FSGS-UC	Focal segmental glomerulosclerosis of undetermined causes
G	Gauge
GAPDH	Glyceraldehyde-3-phosphate dehydrogenase
GBM	Glomerular basement membrane
GFP	Green fluorescent protein
GFP-NLS	Green fluorescent protein-nuclear localization signal
Glom.	Glomerulus
GO	Gene ontology
HBSS	Hank’s balanced salt solution
HEPES	4-(2-Hydroxyethyl)-1-piperazineethanesulfonic acid
HIV	Human immunodeficiency virus
HRP	Horseradish peroxidase
IF	Immunofluorescence
Ig	Immunoglobulin
IHC	Immunohistochemistry
KPT-330	Selinexor

Ldha	Lactate dehydrogenase A
LMB	Leptomycin B
Mab414	Anti-NPC Antibody Clone 414
MCH	Mean corpuscular hemoglobin
MCV	Mean corpuscular volume
Mff	Mitochondrial fission factor
Micu1	Mitochondrial calcium uptake protein 1
min	Minute
MWF	Munich Wistar Frömter
NAD	Nicotinamide adenine dinucleotide
NADH	Reduced nicotinamide adenine dinucleotide
NAD(P)H	Reduced nicotinamide adenine dinucleotide (phosphate)
NCR	Nuclear-to-cytoplasmic ratio
Ndufa2	NADH:Ubiquinone Oxidoreductase Subunit A2
Ndufb8	NADH:Ubiquinone Oxidoreductase Subunit B8
NE	Nuclear envelope
NEP25	Nephrin promoter-driven human CD25
NLS	Nuclear localization signal
NPCs	Nuclear pore complexes
NTRs	Nuclear transport receptors
OD	Optical density
p21	Cyclin-dependent kinase inhibitor 1A
p27	Cyclin-dependent kinase inhibitor 1B
p53	Tumor protein p53
PBS	Phosphate buffered saline
PECs	Parietal epithelial cells
PFA	Paraformaldehyde

PKM	Pyruvate kinase M
pRb	Retinoblastoma protein
PVP	Polyvinylpyrrolidone
Ran	Ras-related nuclear protein
Ran-GDP	Ran bound to GDP
Ran-GTP	Ran bound to GTP
Rho GTPases	Rho family of small GTPases
rpm	Revolutions per minute
RPMI	Roswell Park Memorial Institute medium
RTTA	Reverse tetracycline-controlled transactivator
SARS-CoV-2	Severe acute respiratory syndrome coronavirus 2
SD	Standard deviation or Slit diaphragm
SDS	Sodium dodecyl sulfate
SDS-PAGE	Sodium dodecyl sulfate-polyacrylamide gel electrophoresis
Sec13	Secretory pathway component 13
Serpinb6	Serine protease inhibitor, clade B, member 6
SMCR8	Smith-Magenis syndrome chromosome region candidate 8
SRNS	Steroid-resistant nephrotic syndrome
STED	Stimulated emission depletion
Th2	Type 2 helper T cell
TNF	Tumor necrosis factor
TOM/TIM	Translocase of outer/inner mitochondrial membrane
Tomm40	Translocase of outer mitochondrial membrane 40
Tomm70	Translocase of outer mitochondrial membrane 70
Tpr	Translocated promoter region protein
TRE	Tetracycline-responsive element
TSA	Tyramide signal amplification

TTBS	Tris-buffered saline + Tween-20
U	Unit
ULK1	Unc-51-like autophagy activating kinase 1
V	Volt
VDAC1-3	Voltage-dependent anion channel 1-3
VEGF	Vascular endothelial growth factor
v/v	Volume/volume
W	Week
w/v	Weight/volume
WT-1	Wilms Tumor Protein 1
XPO1	Exportin 1

List of Figures

Figure 1. Overview of the glomerular architecture and the filtration barrier.....16

Figure 2. Pathogenesis of sclerotic lesions in FSGS 18

Figure 3. Structural features of nuclear pore complexes in vertebrates and budding yeast 24

Figure 4. Defective NPCs lead to protein mislocalization 30

Figure 5. Schematic representation of doxycycline-inducible expression of histone-eGFP in podocytes using the Pod-rtTA/histone-eGFP transgenic mouse line 40

Figure 6A. Experimental design for the 20-week group 51

Figure 6B. Experimental design for the 40-week group 51

Figure 6C. Experimental design for the untreated control group.....52

Figure 7. Blood pressure measurement and sample collection 52

Figure 8. Quantification of the average number of podocytes per glomerulus in 3D reveals a marked podocyte loss at 80 weeks of age.....57

Figure 9. Age-related increase in the formation of glomerular synechiae without a significant change in the severity of glomerulosclerosis.....58

Figure 10. Kidney function remains largely preserved during aging 59

Figure 11. A workflow was established in CellProfiler to enable compartment-specific quantification of protein intensity in podocytes in triple-labeled kidney sections.....61

Figure 12. SMCR8 exhibits progressive nuclear translocation in podocytes during aging.....63

Figure 13. Ran shows age-dependent redistribution toward the nucleus while maintaining a predominant cytoplasmic localization in podocytes 64

Figure 14. eIF4E maintains a stable cytoplasmic-predominant localization in podocytes during aging.....65

Figure 15. DRG2 exhibits transient nuclear enrichment during mid-age followed by partial cytoplasmic redistribution in aged podocytes 66

Figure 16. Doxycycline administration via drinking water induces stronger transgene expression in podocytes than intraperitoneal injection 67

Figure 17. Nuclear and cytoplasmic protein fractions from isolated podocytes show high purity 70

Figure 18A. Volcano plot of differential nuclear-to-cytoplasmic (N/C) ratios between 80- and 11-week-old podocytes 73

Figure 18B-D. Gene Ontology enrichment analyses of proteins showing age-dependent shifts in nuclear-to-cytoplasmic (N/C) ratios 74

Figure 19. XPO1 inhibition alleviates nucleocytoplasmic transport defects following Nup93 depletion in HeLa cells expressing 2xGFP-NLS 78

Figure 20. Increased glomerular synechiae in 40-week-old MWF rats 79

Figure 21. Development of FSGS in aged MWF is associated with podocyte loss, PEC activation, and glomerular matrix deposition.....80

Figure 22. Longitudinal assessment of kidney function in control MWF rats.....81

Figure 23. KPT-330 reduces body weight gain in MWF rats 82

Figure 24. KPT-330 alters general physiological parameters in MWF rats 83

Figure 25. KPT-330 increases podocyte nuclear pore complex (NPC) density at week 20 84

Figure 26. KPT-330 enhances Nup93 staining intensity in podocytes 85

Figure 27. KPT-330 increases nuclear localization of XPO1 86

Figure 28. KPT-330 promotes nuclear accumulation of P53 in podocytes.....87

Figure 29. KPT-330 treatment modestly improves renal function and reduces hyperlipidemia.....88

Figure 30. Serum phosphate, potassium, and sodium levels during disease progression are not significantly affected by KPT-330 treatment 89

Figure 31. KPT-330 fails to prevent FSGS progression 90

Figure 32. Podocyte depletion, PEC activation, and glomerular matrix deposition continue after KPT-330 treatment 91

List of Tables

Table 1: List of devices 31

Table 2: List of consumables 32

Table 3: List of reagents 33

Table 4: List of kits 36

Table 5: List of primary antibodies 36

Table 6: List of secondary antibodies 38

Table 7: List of used software 39

Table 8: Optimization of podocyte isolation and eGFP+ cell yield under different experimental conditions 69

Supplementary Table 1: Complete list of proteins exhibiting significant age-dependent changes in nuclear-to-cytoplasmic (N/C) ratios in primary mouse podocytes 124

1 Introduction

1.1 Podocyte Injury in Glomerular Diseases

The kidneys serve as the primary excretory organs in mammals, responsible for the removal of metabolic waste products from the body [1]. Nephrons, the functional units of the kidney, mediate urine formation through three fundamental processes: glomerular filtration, tubular reabsorption, and tubular secretion [2]. In 1844, Ludwig first proposed that the initial stage of urine formation involves the passive filtration of a protein-free fluid within the glomeruli, driven by the hydrostatic pressure of the blood [3]. Building upon this foundational concept, subsequent research has elucidated the structural and functional characteristics of the glomerulus, which serves as the anatomical site of this primary filtration process. Structurally, the glomerulus consists of a tuft of fenestrated capillaries enclosed within the double-layered Bowman's capsule, as illustrated in Figure 1A [4]. It functions as a highly specialized filtration barrier that selectively removes metabolic waste products from the bloodstream while retaining essential macromolecules such as proteins. The resulting protein-free ultrafiltrate is subsequently processed along the nephron to ultimately form urine [5].

Within this filtration apparatus, podocytes play a pivotal role in maintaining both the structure and selectivity of the glomerular barrier. These terminally differentiated epithelial cells cover the outer surface of the glomerular basement membrane (GBM) [6]. Podocytes exhibit a complex morphology characterized by large cell bodies and numerous cytoplasmic extensions-primary processes and interdigitating foot processes (FPs)-facing Bowman's space (Fig. 1B) [7, 8]. Together with the fenestrated endothelium of glomerular capillaries and the GBM, podocytes constitute the glomerular filtration barrier (Fig. 1 A'), a structure further stabilized by mesangial cells [9]. The foot processes of neighboring podocytes form an interdigitating network, separated by narrow gaps known as filtration slits. These are bridged by the slit diaphragm (SD), a specialized junctional complex essential for maintaining selective permeability and ensuring the structural and functional integrity of the glomerular barrier [10].

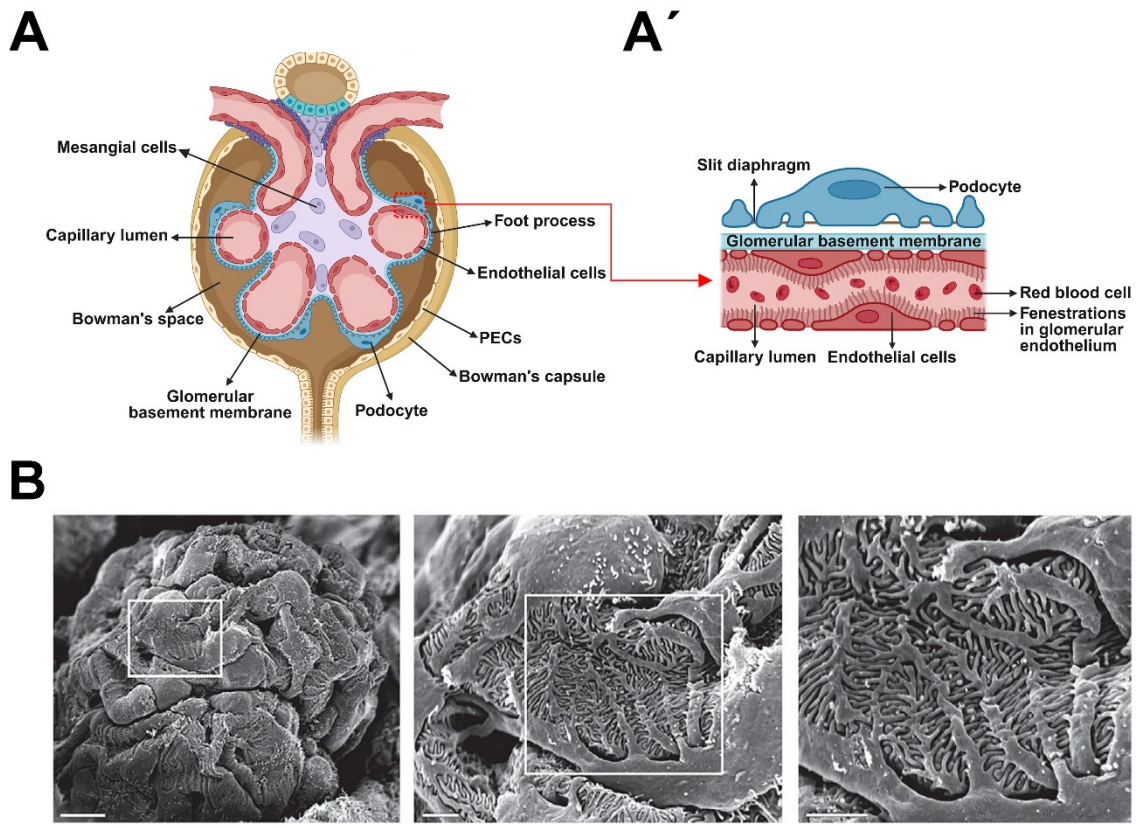


Figure 1. Overview of the glomerular architecture and the filtration barrier. **(A)** Schematic representation of a renal glomerulus showing the main cellular components, including podocytes, endothelial cells, parietal epithelial cells (PECs), and mesangial cells. The capillary loops are enclosed within Bowman's capsule, and the space between them forms Bowman's space. **(A′)** Magnified view of the glomerular filtration barrier, composed of the fenestrated glomerular endothelium, the glomerular basement membrane, and podocyte foot processes connected by slit diaphragms. **(B)** Scanning electron microscopy (SEM) images showing the architecture of the glomerular tuft. From left to right: low-, medium-, and high-magnification views reveal the complex interdigitating morphology of podocyte foot processes covering the capillary loops. White boxes indicate the corresponding zoomed-in regions in the subsequent panels. Scale bars (from left to right): 10 µm, 2 µm and 2 µm. Figure B was taken from [8].

Due to their unique anatomical position, podocytes are simultaneously exposed to signaling molecules from the urinary space and to mechanical and biochemical cues transmitted through the GBM [4]. To maintain glomerular homeostasis, podocytes continuously respond to these dynamic stimuli. However, maladaptive responses or sustained exposure to injurious stimuli, such as hyperfiltration-induced shear stress [11], toxins, or inflammation, can cause podocyte injury, detachment from the GBM, and the onset of glomerular diseases. Furthermore, genetic mutations affecting podocyte-specific genes can disrupt structural or functional integrity, leading to similar pathological consequences [12, 13]. Critically, as terminally differentiated cells lacking proliferative capacity, podocytes are irreplaceable once lost, making the glomerular filtration barrier particularly vulnerable to irreversible damage [14].

Podocyte injury has been recognized as a central pathological feature in various glomerular diseases, including focal segmental glomerulosclerosis (FSGS), diabetic nephropathy, and minimal change disease [15]. Despite differences in their histopathological features under light microscopy, these conditions frequently share a common clinical feature: significant proteinuria, which reflects disruption of the filtration barrier primarily due to podocyte dysfunction [16].

Although significant progress has been made in elucidating the molecular mechanisms of podocyte injury, the precise signaling pathways remain incompletely characterized, and clinically effective therapeutic targets are still lacking. Therefore, uncovering the underlying mechanisms of podocyte injury and developing novel pharmacological interventions represent urgent and high-priority objectives in glomerular disease research.

1.2 Focal Segmental Glomerulosclerosis (FSGS)

FSGS is not a single disease entity, but rather a histopathological pattern of glomerular injury. It is defined by the presence of sclerotic lesions that are segmental (involving less than 50% of the glomerular tuft) and focal (involving fewer than 50% of all glomeruli) on light microscopy [17]. Under electron microscopy, FSGS is characterized by varying degrees of podocyte foot process effacement and denuded segments of the GBM [18]. Accurately determining the incidence and prevalence of FSGS remains challenging due to limited access to renal biopsies globally [19]. Nevertheless, the estimated global incidence of FSGS is approximately 7 per 1 million individuals per year, with a prevalence of around 4% [20]. FSGS accounts for roughly 20% of nephrotic syndrome (NS) cases in children and up to 40% in adults [21]. Sex differences have been shown to influence disease occurrence, with men exhibiting a higher incidence of FSGS. Moreover, affected males often present with more severe proteinuria, a higher risk of relapse, and a reduced rate of remission compared to females [22]. Racial and ethnic disparities are also evident. For instance, an analysis of the United States Renal Data System revealed that black individuals have a fourfold greater risk of progressing to end-stage renal disease (ESRD) due to FSGS compared to white or Asian individuals [23].

1.2.1 Mechanisms of Sclerotic Lesion Development in FSGS

The formation of sclerotic lesions in FSGS has been intensively investigated over the past decade, and it is now well recognized that podocyte injury or loss represents the initial triggering event (see Figure 2B) [24]. Following podocyte depletion, mesangial cells and parietal epithelial cells (PECs) become activated. Mesangial cells increase the production of extracellular matrix components, while normally quiescent PECs begin to proliferate and/or migrate. This pathological response leads to the formation of cellular bridges or adhesions between the glomerular capillary tuft and Bowman's capsule [25] (Figure 2B).

If this pathological process continues untreated, activated PECs continue their dysregulated migration and proliferation, depositing extracellular matrix along the GBM and invading the glomerular tuft (Figure 2C). This promotes the development of segmental sclerotic lesions and capillary collapse, primarily due to disrupted vascular endothelial growth factor signaling (VEGF) [26]. Ultimately, portions of the glomerular capillary network become non-functional (Figure 2D). With ongoing progression, these segmental lesions may extend to involve the entire glomerulus, ultimately leading to global glomerulosclerosis.

Clinically, FSGS typically presents with nephrotic-range proteinuria and progressive renal function decline, consistent with other glomerular diseases that originate from podocyte injury or depletion [27].

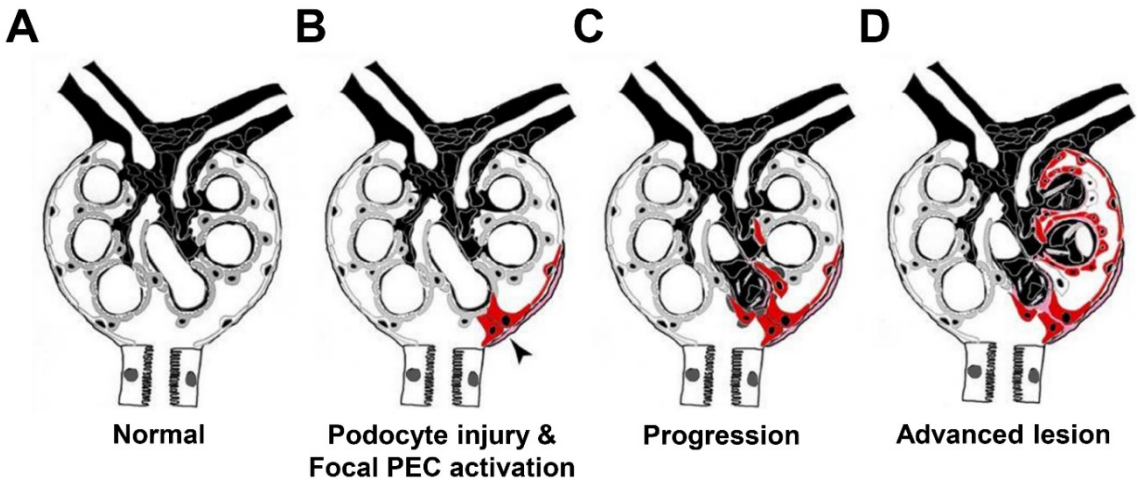


Figure 2. Pathogenesis of sclerotic lesions in FSGS. (A) Normal glomerulus. Light gray, podocytes; white, PECs. **(B)** Podocyte injury or loss triggers focal PEC activation (red), PECs form an adhesion to the capillary tuft (arrow). **(C)** PECs take over parts of the capillary segment, capillaries are lost. **(D)** Advanced stage. Figure taken from [24] with modification.

1.2.2 Classification of FSGS

1.2.2.1 Classification Based on Etiology of Podocyte Injury

FSGS can be classified into four major categories based on the etiology of podocyte injury: primary FSGS, secondary FSGS, genetic FSGS, and FSGS of undetermined causes (FSGS-UC) [20].

Primary FSGS is thought to result from circulating permeability factors that directly injure podocytes and disrupt the glomerular filtration barrier. Several candidate factors, such as CLC-1, VEGF, hemopexin, TNF, and suPAR, have been proposed. However, none have been conclusively validated as the singular pathogenic agent [28].

Secondary FSGS develops in response to conditions that either reduce the number of functioning nephrons or subject the remaining nephrons to abnormal stress. Notable causes include virus-associated FSGS (e.g., HIV, parvovirus B-19, cytomegalovirus, SARS-CoV-2) and drug-induced FSGS, which results from podocyte toxicity caused by medications such as pamidronate, lithium, and mTOR inhibitors [29, 30, 31].

Genetic FSGS arises from mutations in genes encoding key structural or regulatory proteins in podocytes. These mutations can manifest in both childhood and adulthood. Genetic testing is recommended in patients with a family history of chronic kidney disease, steroid-resistant nephrotic syndrome, or poor treatment response [32]. Over 50 genes have been implicated in FSGS pathogenesis, including genes for the proteins Nephrin (*NPHS1*), Podocin (*NPHS2*), Inverted Formin-2 (*INF2*), and Apolipoprotein L1 (*APOL1*) [33]. These play crucial roles in maintaining podocyte integrity, cytoskeleton organization, slit diaphragm function, and the glomerular filtration barrier.

1.2.2.2 Columbia Classification System

In addition to the etiological classification system, the Columbia Classification System, proposed by Vivette D'Agati in 2003, categorizes FSGS into five morphological variants: (1) collapsing variant, (2) tip variant, (3) cellular variant, (4) perihilar variant, and (5) not otherwise specified (NOS) variant [34]. Although this histological framework enhances the understanding of morphological heterogeneity, its clinical applicability is limited due to the variable etiologies, incomplete pathophysiological insights, weak correlations between histopathological subtypes and clinical outcomes. Thus, the classification of FSGS should be viewed as a multidimensional process that integrates clinical

history, laboratory parameters, renal biopsy, and, when appropriate, genetic testing [18].

1.2.3 Treatment of FSGS

Treatment strategies for FSGS are largely determined by its underlying etiology. In primary FSGS, particularly cases presenting with nephrotic syndrome, high-dose corticosteroids, such as prednisone or methylprednisolone, remain the first-line therapy. For patients who are resistant to corticosteroids, alternative immunosuppressive agents, such as calcineurin inhibitors, may be employed [35]. Additional therapeutic options encompass alkylating agents, anti-proliferative drugs like mycophenolate mofetil, and biological agents such as rituximab. However, the overall efficacy of these treatments remains suboptimal, and their use is still the subject of clinical debate [18, 37].

In secondary FSGS, management centers on treating the inciting condition. For instance, antiviral therapy may be appropriate in virus-associated FSGS, while withdrawal of nephrotoxic agents is warranted in drug-induced cases [38].

Given the heterogeneous and often overlapping etiologies of FSGS, supportive therapy forms an essential component of management in all patients, particularly those with persistent proteinuria. This includes nonspecific renoprotective measures aimed at controlling blood pressure and reducing proteinuria [39]. Blood pressure management typically involves a combination of dietary modifications (e.g., restriction of sodium, potassium, and calcium) and antihypertensive therapy. Among these, agents that inhibit the renin-angiotensin-aldosterone system, including angiotensin-converting enzyme inhibitors and angiotensin II receptor blockers, are particularly effective [40]. These agents not only reduce systemic blood pressure but also lower intraglomerular pressure, thereby mitigating proteinuria and providing long-term renal protection [41].

Despite its increasing recognition as a leading glomerular cause of kidney failure worldwide, FSGS remains a therapeutic challenge due to its complex etiology, overlapping clinical features, and variable response to treatment [42]. Continued research into its pathogenesis and the development of targeted therapies is essential for improving patient outcomes.

1.3 Available FSGS Animal Models

A wide range of animal models has been developed to reproduce different pathological aspects of human focal segmental glomerulosclerosis (FSGS) [43]. These conventional FSGS models can be summarized into four major categories: renal ablation model, chemical or toxin-induced models, genetically modified models, and spontaneous FSGS models [44].

1.3.1 Renal Ablation Model

The 5/6 nephrectomy model is created by removing one kidney and excising 2/3 of the remaining kidney. The substantial loss of renal tissue results in progressive hyperfiltration and proteinuria over time, with more than half of the glomeruli exhibiting sclerotic lesions by the seventh week [44]. However, most animals begin to succumb to uremia between the 12th and 16th week after surgery [43]. Moreover, postoperative complications such as bleeding and infection are relatively common, posing challenges both to model reproducibility and animal welfare. These factors make the PNx model technically demanding and ethically constrained.

1.3.2 Chemical or Toxin-Induced Models

Two classic nephrotoxic agents-adriamycin and puromycin aminonucleoside-are frequently used to induce podocyte injury. Most rat strains are susceptible to these compounds, whereas most mouse strains are resistant, with the notable exception of Balb/c mice, which are sensitive to adriamycin-induced FSGS [45]. Both drugs trigger renal injury within several days of administration, leading to predictable and reproducible patterns of glomerular damage [46]. Nevertheless, their systemic toxicity often complicates data interpretation, and their narrow therapeutic window means that even slight variations in dosage can produce substantial differences in disease severity [46].

1.3.3 Genetically Engineered Models

With the advent of molecular genetics, multiple transgenic and knockout models have been generated to mimic human FSGS. Among these, the Thy-1.1 transgenic mouse is one of the most widely used. These mice spontaneously develop albuminuria by the eighth week after birth, and by six months, roughly 20% of glomeruli exhibit sclerotic lesions [47]. The onset and severity of renal damage can be experimentally accelerated in heterozygous mice by injecting

anti-Thy-1.1 monoclonal antibodies, which cause acute proteinuria through direct, dose-dependent podocyte injury [48]. This system provides a valuable platform for investigating the cascade from podocyte damage to albuminuria and FSGS progression [44]. Other engineered models include the NEP25 transgenic mouse, transient receptor potential cation channel 6 overexpression model, HIV-associated nephropathy model, and α-actinin-4 knock-in mutation model, among others. Owing to technical limitations, genetic manipulation is more feasible in mice than in rats. Nevertheless, the rat nephropathy model remains the one most closely reflecting human glomerular pathophysiology [49].

1.3.4 Models with spontaneous FSGS

Several inbred rat strains develop FSGS spontaneously without any experimental induction [50]. Among these, Buffalo/Mna and Munich Wistar Frömter (MWF) rats are the most extensively characterized. Despite sharing a spontaneous onset of glomerular injury, the underlying mechanisms differ between the two strains. In Buffalo/Mna rats, FSGS appears to arise from an immune-mediated disorder involving macrophages and Th2 lymphocytes. During the prealbuminuric phase, early macrophage infiltration and Th2 polarization have been reported [50]. By contrast, MWF rats display a congenital deficit in nephron number, which drives persistent glomerular hyperfiltration, podocyte overload, and progressive podocyte loss, eventually resulting in proteinuria and glomerulosclerosis [51]. From a temporal perspective, Buffalo/Mna rats generally develop proteinuria at 3-4 months of age, which limits their applicability in short-term studies [44]. In contrast, MWF rats exhibit proteinuria by approximately 10 weeks of age, and by 9 months, marked glomerulosclerotic changes become evident. The moderate pace of disease progression in MWF rats makes them more practical and time-efficient for experimental research, as it enables observation of disease development within a manageable experimental timeframe. Notably, this strain also shows gender dimorphism, with males typically presenting more severe pathological alterations than females. Furthermore, unlike models in which podocyte injury is acutely induced, the gradual and progressive pathology in MWF rats offers an extended window for studying the dynamic processes of podocyte injury and repair in FSGS.

1.4 The Nuclear Pore Complex

The development of the nuclear membrane represents a key innovation in the evolution of eukaryotic cells from prokaryotic ancestors [52]. With this membrane in place, the genomic content of eukaryotic cells became physically separated from the cytoplasm, enabling the evolution of a more compartmentalized and tightly regulated cellular system. In this advanced system, nuclear pore complexes (NPCs) govern bidirectional exchange of molecules between the nucleus and the cytoplasm [53]. The mammalian NPC is a ~120 MDa protein complex composed of multiple copies of approximately 30 different nucleoporins (Nups) [54]. It exhibits a tripartite ring architecture: the inner ring (Figure 3, green) is positioned where the inner and outer nuclear membranes fuse, forming a central channel lined with phenylalanine-glycine (FG) repeat proteins. These FG repeats form the selective permeability barrier and mediate active cargo transport [55]. The two outer rings (Figure 3, orange) serve as structural scaffolds. The cytoplasmic ring, located on the cytoplasmic side of the nuclear envelope, anchors cytoplasmic filaments (Figure 3, brown) that extend into the cytoplasm. In contrast, the nuclear ring faces the nucleoplasm and supports the nuclear basket (Figure 3, blue), a filamentous structure that projects into the nuclear interior [56]. The Nup composition of each region, and differences between human and yeast NPCs, are detailed in Figure 3. While small metabolites and ions can freely diffuse through the NPCs, the nuclear import and export of most proteins and RNA-protein complexes require specific transport signals that are recognized by nuclear transport receptors (NTRs) [57]. These receptors, either alone or in complex with their cargos, traverse the NPCs via facilitated diffusion [58]. Beyond transport, NPCs also play critical roles in a range of cellular processes, including gene expression [59, 60], cell cycle regulation [61], and cellular stress responses [62]. Notably, SUMOylation of the nuclear basket components has been implicated in modulating the NPC’s role in sensing and responding to cellular stress [63].

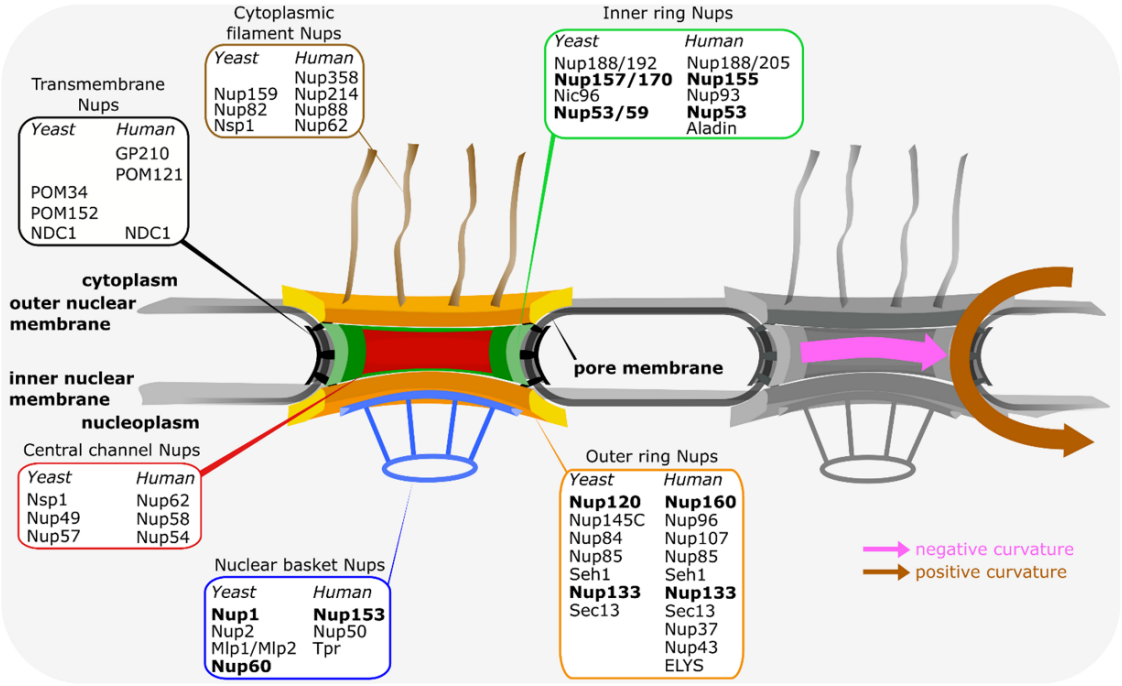


Figure 3. Structural features of nuclear pore complexes in vertebrates and budding yeast. The nuclear pore complex (NPC) of vertebrates and budding yeast shares several key structural characteristics. A schematic depiction of the NPC illustrates its ring-shaped and peripheral assemblies. The inner ring (shown in green) is positioned between the two outer rings-the cytoplasmic and nucleoplasmic rings (colored yellow/orange). Extending outward from these outer rings are the cytoplasmic filaments (in brown) and the nuclear basket (in blue). The inner ring (green) functions as the central scaffold that links the membrane-anchored nucleoporins (in black) with those forming the central transport channel (in red), which are vital for the selective permeability and transport properties of the NPC. The spatial organization of nucleoporins-based on human and budding yeast nomenclature-is indicated within each structural subcomplex. Nucleoporins that make direct contact with the pore membrane are highlighted in bold. The diagram on the right illustrates regions of positive and negative curvature within the pore membrane. Figure taken from [58].

In proliferating cells, NPCs disassemble in coordination with the breakdown of the nuclear envelope (NE) during the prophase. This process is driven by extensive phosphorylation of multiple Nups, which disrupts critical protein-protein interactions at key contact points within the NPC [64]. Rather than disassembling into individual protein components, the NPCs break down into subcomplexes or smaller structural modules, which remain soluble in the mitotic cytosol [65]. This modular breakdown allows for the rapid and efficient reassembly of NPCs at the end of mitosis, typically within a few minutes [66]. This cyclical breakdown and reconstruction of NPCs is referred to as postmitotic reassembly. In contrast, interphase assembly occurs during the interphase of the cell cycle and involves the de novo insertion of new NPCs into an intact nuclear envelope through a membrane fusion process. Unlike postmitotic reassembly, this process is

constructive rather than reconstructive, proceeds more slowly, and does not require prior disassembly of existing NPCs [67, 68].

Postmitotic reassembly has been more extensively studied, particularly in rapidly dividing cells, where it accounts for the majority of NPC biogenesis. A notable area of interest is the dynamic or stable association of nucleoporins with NPCs [68]. Using stable cell lines expressing GFP-tagged Nups, Gwénaël Rabut et al. tracked the behavior of 19 Nups and revealed a broad spectrum of residence times, from mere seconds to several days [69]. Nups located in the central scaffold region tend to be highly stable, consistent with their structural scaffold roles, while more peripheral components exhibit dynamic turnover, suggesting functions in cargo regulation and adaptor activity [70]. In dividing cells, the periodic turnover of NPC components facilitates quality control, allowing replacement or repair of damaged or defective parts during each cycle [71]. However, this regenerative mechanism is absent in postmitotic cells, which no longer undergo division. This raises important questions regarding how NPC structural integrity and functionality are maintained over extended periods in non-dividing, differentiated cells.

In yeast, studies have shown that during replicative aging, NPC protein components lose their stoichiometric balance, despite no corresponding change at the transcript level [72]. Subsequent research confirmed this discrepancy and further identified a decline in NPC assembly factors during aging. These changes were accompanied by reduced nucleocytoplasmic trafficking efficiency, such as slower shuttling of transcription factors, and increased nuclear compartmentalization. These findings suggest that the rates of NPC renewal and NPC quality control are not always synchronized throughout the lifespan of mitotic cells, potentially leading to gradual functional decline [71].

In postmitotic cells, which lack mitotic NPC renewal, evidence suggests that aging is associated with NPC deterioration [73]. Using Caenorhabditis elegans, a nematode model with easily separable developmental stages, and rat brain tissue, Maximiliano A. D'Angelo et al. discovered a dramatic increase in nuclear envelope "leakiness" during aging. Furthermore, specific Nups such as Nup93 and Nup153 were found to be oxidatively damaged in aged, differentiated cells, implying that NPCs accumulate molecular damage over time. This degradation

may contribute to age-related nuclear transport defects and cellular dysfunction [74].

1.5 Nuclear Pore Complex Defects and Diseases

The study of NPCs, Nups, and the nucleocytoplasmic transport they mediate has yielded important insights into the pathogenesis of various diseases. These findings have unveiled an unexpected level of molecular complexity, offering new perspectives on both disease onset and progression.

1.5.1 NPCs in Embryonic Development

NPCs play a crucial role in embryonic development, and disruptions in NPC components often result in severe developmental abnormalities. Studies in mice have shown that homozygous knockout of specific Nups typically leads to embryonic lethality or death shortly after birth. In rare cases where null mice survive, they commonly exhibit profound physiological defects, including infertility and significantly reduced lifespan [75].

1.5.2 NPCs in Neurological Disorders

NPCs have been extensively studied in the context of neurological disorders, particularly neurodegenerative diseases [76]. Disruptions in NPC function and the associated nucleocytoplasmic transport machinery-such as nuclear transport receptors (NTRs), Ran GTPase, and its regulatory protein RNA GTPase-activating protein 1-have been identified as key pathogenic factors in several neurodegenerative conditions, such as amyotrophic lateral sclerosis, Alzheimer's disease, Parkinson's disease, frontotemporal dementia, and Huntington's disease [76]. Notably, NPCs also play critical roles in mammalian brain development [77] and in the response to brain injury [78], further underscoring their essential contribution to central nervous system homeostasis and integrity.

1.5.3 NPCs in Cancer Development and Progression

The role of NPCs in cancer has emerged as a major focus of recent research. Several components of the NPC, such as Tpr, Nup98, Nup358, and Nup214, have been implicated in chromosomal translocations that give rise to oncogenic fusion proteins in various malignancies, for example T cell acute lymphocytic leukemia, acute myeloid leukemia, Blast crisis of chronic myeloid leukemia and so on [75, 79]. However, the precise mechanisms by which these fusion proteins

contribute to tumorigenesis remain incompletely understood. In addition, altered expression levels of nucleoporins have been frequently observed in cancerous tissues compared to their healthy counterparts. For instance, Nup88, which interacts with mitotic spindles, is often overexpressed in cancer cells and has been associated with tumor progression and poor clinical outcomes [80, 81]. Likewise, Nup62 expression is significantly elevated in both metastatic and localized prostate cancer compared to benign prostate tissue [82]. A wide array of other nucleoporins and nucleocytoplasmic transport factors, such as Nup210, Nup133, Nup107, Sec13, Nup188, Nup93, Nup153, RanGap1, and Rae1, are also dysregulated across multiple cancer types [83, 84].

Beyond their structural or fusion-related roles, the nucleocytoplasmic transport processes themselves have become therapeutic targets in oncology. One notable example is KPT-330 (Selinexor), an inhibitor of the nuclear export protein XPO1 (also known as chromosome maintenance protein 1, CRM1). Selinexor received Food and Drug Administration approval for the treatment of relapsed or refractory multiple myeloma in 2019 and diffuse large B-cell lymphoma in 2020 [85]. XPO1 mediates the export of over 200 known cargo proteins from the nucleus to the cytoplasm, including key tumor suppressors such as p53, p21, p27, BRCA1/2, pRB, FOXO family members [86, 87]. By inhibiting XPO1, Selinexor induces the nuclear retention and reactivation of these tumor suppressors, thereby restoring cell cycle checkpoints, inhibiting tumor proliferation, and promoting apoptosis in malignant cells [88]. Ongoing clinical trials are now investigating Selinexor’s efficacy in additional cancer types, including advanced or recurrent endometrial cancer [89] and myelofibrosis [90], highlighting the promise of targeting nuclear export pathways as a novel therapeutic strategy in cancer.

1.5.4 NPCs in Viral Infection

NPCs also play a key role in viral infections, particularly in facilitating the nuclear entry of viruses. Many viruses rely on interactions with the NPCs, either directly or indirectly, depending largely on the size and structural properties [91, 92]. Some viruses are small enough to traverse the NPC intact, while others must partially disassemble or interact with nuclear transport machinery to gain access to the nuclear compartment. Furthermore, viruses have evolved mechanisms to exploit NPCs and manipulate their selectivity, thereby enhancing viral replication

and evasion of host defenses. For example, studies have shown that human immunodeficiency virus type 1 (HIV-1) can bypass the tightly regulated barrier function of NPCs, which typically allows selective transport of host macromolecules. Although the intact HIV-1 virus is too large to pass through NPCs, its capsid, which encloses the viral genome, can interact with host nucleoporins at the cytoplasmic side, within the pore, and even inside the nucleus [93, 94]. These interactions appear to facilitate the nuclear import of the viral genome, potentially by mimicking host transport processes or hijacking transport receptors. However, the precise molecular mechanisms underlying these events remain poorly understood, and are an area of ongoing investigation.

1.5.5 NPCs in Kidney Diseases: Focus on FSGS

The role of NPCs in kidney diseases, particularly in steroid-resistant nephrotic syndrome (SRNS), has attracted increasing attention in recent years. Notably, kidney biopsy findings indicate that FSGS is present in approximately 89% of patients with nucleoporin-associated SRNS [95]. In 2015, Miyake et al. identified biallelic mutations in the nucleoporin gene *NUP107* in nine affected individuals from five unrelated families diagnosed with early-onset SRNS. Histopathological examination revealed FSGS as the underlying lesion. Functional studies demonstrated that knockdown of *Nup107* in zebrafish resulted in hypoplastic glomeruli and abnormal podocyte foot processes, implicating this nucleoporin in podocyte integrity and glomerular development [96]. Subsequent studies have identified similar disease associations with other NPC components. Mutations in *NUP93* and its interacting partners *NUP205* and *exportin 5* (*XPO5)* genes were reported in eight families with SRNS, with affected individuals also exhibiting FSGS [97]. In a later study, Hussain et al. reported the presence of a new heterozygous missense variant in *XPO5* gene among two families exhibiting FSGS and chronic kidney disease [98]. Further research extended these findings by identifying mutations in *NUP107*, *NUP85*, *NUP133*, and *NUP160* in 13 families with SRNS. Functional knockdown of these genes in Xenopus models led to disrupted glomerulogenesis, further supporting their essential role in kidney development [99]. A case study from Japan described a woman with persistent proteinuria, hypoalbuminemia, and biopsy-confirmed FSGS who carried two heterozygous mutations in *NUP93*. Reduced NUP93 expression was detected in both glomerular and tubulointerstitial compartments, emphasizing its importance

in maintaining glomerular structure and function [100]. In recent years, an increasing number of mutations in NUP genes have been identified in patients with FSGS [101, 102, 103, 104].

However, despite growing evidence that defects in the NPC contribute to FSGS development, how its disruption compromises podocyte homeostasis is still largely unknown [105]. To date, three major signaling pathways have been proposed to be involved in nucleoporin-associated SRNS: the Rho family of small GTPases (Rho GTPases), the Smad family member 4 (Smad4) signaling pathway, and the Hippo signaling pathway, all of which provide new opportunities for therapeutic intervention in SRNS [94].

These findings have led to the proposal of a new disease concept termed "NUP nephropathy," which posits that mutations or functional defects in nucleoporins can directly contribute to glomerular injury and kidney dysfunction [106]. This emerging concept highlights the critical role of NPC integrity in renal homeostasis and suggests that disruptions in nucleocytoplasmic transport may be a previously underrecognized mechanism in the pathogenesis of FSGS and other podocytopathies.

1.6 Aim of This Work

The aim of this study was to investigate the diagnostic and therapeutic potential of the nuclear-to-cytoplasmic ratio (NCR) of specific proteins in podocytes, in the context of cellular aging and development of FSGS. The underlying hypothesis is that dysfunction of the NPC barrier leads to impaired nucleo-cytoplasmic compartmentalization, particularly affecting post-mitotic cells such as podocytes. This impairment may contribute to age-related kidney dysfunction and the pathogenesis of FSGS.

Based on this hypothesis, the study focused on the following research objectives:

1. Evaluate the diagnostic value of NCR in post-mitotic podocytes: The NCR was established and analyzed using selected marker proteins known to exhibit age-dependent mislocalization in other post-mitotic cells, such as neurons.
2. Identify novel and potentially more sensitive NCR markers in podocytes: This involved the establishment of an advanced podocyte isolation

protocol in mice, followed by a comparative analysis of the subcellular proteome (nuclear vs. cytoplasmic) in podocytes from young and aged mice.

3. Explore a novel approach to restore proper compartmentalization: The NPC barrier was experimentally manipulated *in vitro* using a cellular assay to assess the potential for correcting NCR defects.
4. Investigate a therapeutic approach to modulate NPC barrier function *in vivo*: The impact of NPC permeability modulation was tested in a rat model of FSGS to evaluate its potential as a treatment strategy.

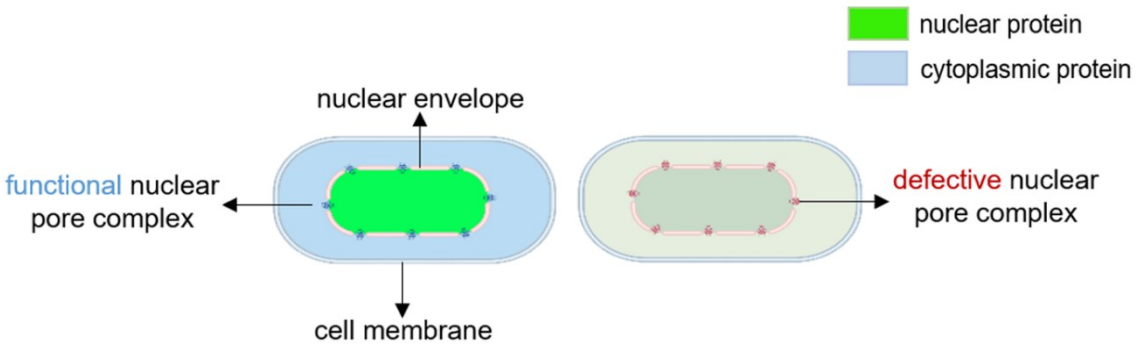


Figure 4. Defective NPCs lead to protein mislocalization. Under healthy conditions, NPCs control nucleocytoplasmic transport to maintain proper nucleo-cytoplasmic compartmentalization. However, mutations in nucleoporins or progressive defects in NPCs - specifically in post-mitotic cells - can compromise this barrier function, resulting in disrupted compartmentalization between the nucleus and cytoplasm.

Collectively, this work is expected to identify loss of nucleocytoplasmic compartmentalization as a previously underappreciated hallmark of podocyte aging and FSGS. By linking NPC barrier dysfunction to spatial proteome remodeling and mitochondrial stress, this study aims to provide a conceptual framework that may enable the development of mechanism-based biomarkers and therapeutic strategies targeting nuclear transport integrity in chronic glomerular disease.

2 Materials

2.1 Devices

Table 1: List of devices

Device	Manufacturer
- BX50 Light microscope	Olympus, Hamburg (DE)
- Celltac α VET (MEK-6550)	Nihon Kohden, Tokyo (Japan)
- Centrifuge 5417 R	Eppendorf AG, Hamburg (DE)
- Coda blood pressure measurement system	Kent Scientific Corporation, Torrington (CT, USA)
- Environmental controller system UNO-T-H-CO2	Okolab, Ottaviano (IT)
- FACSCanto II™	BD Biosciences, San José (CA, USA)
- Biorevo BZ-9000 Fluorescence microscope	Keyence Deutschland GmbH, Neu-Isenburg (DE)
- FiveEasy Plus pH meter	Mettler Toledo, Greifensee (CH)
- FV1000MPE 2-photon microscope	Olympus Corp., Tokyo (Japan)
- Leica SP8 Tau-STED3X microscope	Leica Biosystems Nussloch GmbH, Nußloch (DE)
- SpectraMax iD3 Multi-Mode Microplate Reader	Molecular devices, LLC, San José (CA, USA)
- Nikon Ti2-E confocal microscope	Nikon, Melville (NY, USA)
- Pipets	Eppendorf AG, Hamburg (DE)
- Pipetboy	Integra Biosciences GmbH, Bibertal (DE)
- Precision balance ST77E	Seifert Instruments GmbH, Bachmehring (DE)

- VITROS XT 3400 Chemistry System	Ortho Clinical Diagnostics, Neckargemuend (DE)
- Vortex-Genie 2 Shaker	Scientific Industries, Bohemia (NY, USA)
- Sterile bench Hera safe	Heraeus, Hanau (DE)
- Thermomixer comfort	Eppendorf AG, Berzdorf (DE)
- Warming platform	Kent Scientific Corporation, Torrington (CT, USA)
- Western blot developing machine	Bio-Rad, Hercules (CA, USA)
- Western blot equipment	Bio-Rad, Hercules (CA, USA)
- Zeiss LSM 710 microscope	Carl Zeiss, Oberkochen (DE)

2.2 Consumables

Table 2: List of consumables

Consumable	Manufacturer
- 5 ml Polystyrene Round-Bottom Tube with Cell-Strainer Cap	Corning Inc., Corning (NY, USA)
- Amersham Protran WB Membranes (0,45 µm)	Cytiva, Marlborough (MA, USA)
- Venofix® A needle	B. Braun Melsungen SE, Melsungen (DE)
- Cell strainer	Corning Inc., Corning (NY, USA)
- Eppendorf tubes	Eppendorf AG, Hamburg (DE)
- Falcon 15/50 ml High Clarity PP Centrifuge Tubes	Corning Inc., Corning (NY, USA)
- Feeding needle (curved, 1.2*60 mm)	Henry Schein Vet GmbH, Hamburg (DE)
- Microscope slides	Thermo Scientific, Waltham (MA, USA)
- Omnican® F syringes	B. Braun Melsungen SE, Melsungen (DE)

- Petri dishes	Nunc ™, Nürtingen (DE)
- Scalpel No. 11	Feather Safety Razor Co., Osaka (Japan)
- 10% SDS-PAGE Gel	Bio-Rad, Hercules (CA, USA)
- Stripette®	Corning Inc., Corning (NY, USA)
- Spectra Multicolor Broad Range Protein Ladder	Thermo Fisher, Waltham (MA, USA)

2.3 Reagents

Table 3: List of reagents

Reagent	Manufacturer
- 1,6-hexanediol	Sigma-Aldrich Chemie, Darmstadt (DE)
- 4′,6-Diamidine-2-phenylindole (DAPI)	Roche Diagnostics GmbH, Mannheim (DE)
- 8-well high µ-Slide	Ibidi, Graefelfing (DE)
- Ethanol absolute	Sigma-Aldrich Chemie, Darmstadt (DE)
- Albumin bovine Fraction V, pH 7.0 (BSA)	SERVA Electrophoresis GmbH, Heidelberg (DE)
- Buprenovet	Elanco Animal Health Inc, Greenfield (IN, USA)
- Citric Acid-Based Antigen unmasking solution	Vector Laboratories, Newark (CA, USA)
- Clarity™ Western ECL Substrate	Bio-Rad, Hercules (CA, USA)
- Collagenase Type II	Worthington Biochemical Corporation, Lakewood (NJ, USA)
- Diaminobenzidine (DAB)	Sigma-Aldrich Chemie, Darmstadt (DE)
- Dithiothreitol (DTT)	Bio-Rad, Hercules (CA, USA)

- DNase I	AppliChem GmbH, Darmstadt (DE)
- Doxycycline hyclate	Fagron GmbH, Glinde (DE)
- Dulbecco's Modified Eagle Medium	Gibco, Waltham (MA, USA)
- Ethyl cinamate	Sigma-Aldrich Chemie, Darmstadt (DE)
- Ethylenediaminetetraacetic acid (EDTA)	Sigma-Aldrich Chemie, Darmstadt (DE)
- Ethylene glycol tetraacetic acid (EGTA)	Sigma-Aldrich Chemie, Darmstadt (DE)
- Fetal bovine serum (FBS)	Gibco, Waltham (MA, USA)
- Formaldehyde solution, 4%	Sigma-Aldrich Chemie, Darmstadt (DE)
- Glycien	AppliChem GmbH, Darmstadt (DE)
- Hank's Balanced Salt Solution (HBSS, with calcium and magnesium, no phenol red)	Life Technologies, Grand Island (NY, USA)
- Coverslip, #1.5 H	Paul Marienfeld GmbH & Co. KG, Lauda-Königshofen (DE)
- Hematoxylin	Merck KGaA, Darmstadt (DE)
- HEPES Buffer Solution, 1M	Gibco, Waltham (MA, USA)
- Histokitt	Carl Roth GmbH + Co. KG, Karlsruhe (DE)
- Halt Protease & Phosphatase Inhibitor Cocktail (100x)	Thermo Fisher, Waltham (MA, USA)
- Immu-Mount	Thermo Electron Corp., Pittsburgh, PA, USA
- Ketamine, 10%	Serumwerk Bernburg AG, Bernburg (DE)
- Leptomycin B	Enzo Life Sciences, Lörrach (DE)
- Lipofectamine RNAiMAX	Thermo Fisher, Waltham (MA, USA)
- Magnesium chloride ($MgCl_2$)	Merck Schuchardt OHG, Hohenbrunn (DE)

- Methyl green	Sigma-Aldrich Chemie, Darmstadt (DE)
- Non-targeting control siRNA	Ambion Life Technologies, Austin (TX, USA)
- Paraformaldehyde (PFA)	Sigma-Aldrich Chemie, Darmstadt (DE)
- Penicillin/Streptomycin	Life Technologies, Grand Island (NY, USA)
- Periodic acid	Sigma-Aldrich Chemie, Darmstadt (DE)
- Phosphate buffered saline (PBS)	Life Technologies, Grand Island (NY, USA)
- Pluronic F-68	Life Technologies, Grand Island (NY, USA)
- Polyvinylpyrrolidone (PVP) K30	Sigma Aldrich, Darmstadt (DE)
- Potassium chloride (KCl)	Carl Roth GmbH + Co. KG, Karlsruhe (DE)
- Protease from Streptomyces griseus (Pronase E)	Sigma-Aldrich Co, St. Louis (MO, USA)
- Roswell Park Memorial Institute (RPMI) 1640 Medium with L-glutamine	Life Technologies, Grand Island (NY, USA)
- Schiff's reagent	Sigma-Aldrich Chemie, Darmstadt (DE)
- Selinexor (KPT-330, used in *in vivo* experiments)	Adooq Bioscience, Irvine (CA, USA)
- Selinexor (KPT-330, used in *in vitro* experiments)	Selleckchem GmbH, Houston (TX, USA)
- SiR-DNA	Spirochrome, Stein am Rhein (CH)
- siRNA against Nup93	Eurofins, Luxembourg (LU)
- Sodium chloride solution, 0.9%	B. Braun Melsungen SE, Melsungen (DE)
- Sodium deoxycholate	Sigma-Aldrich Chemie, Darmstadt (DE)
- Sodium dodecyl sulfate (SDS)	Bio-Rad, Hercules (CA, USA)

- Sucrose	Sigma-Aldrich Chemie, Darmstadt (DE)
- Tris	Bio-Rad, Hercules (CA, USA)
- Xylazine	Wirtschaftsgenossenschaft deutscher Tierärzte eG, Garbsen (DE)
- Xylene	Otto Fischar GmbH, Saarbrücken (DE)

2.4 Kits

Table 4: List of kits

Kit	Manufacturer
- Mouse & Rat Cystatin C ELISA Kit – Quantikine	R&D Systems, Minneapolis (MN, USA)
- NanoOrange™ Protein Quantitation Kit	Thermo Fisher, Waltham (MA, USA)
- Nephrat™ II (Rat Albuwell™/Albumin ELISA)	Ethos Biosciences, Logan Township (NJ, USA)
- TSA Biotin System	Akoya Biosciences, Marlborough (MA, USA)
- VECTASTAIN® ABC kit	Vector Laboratories, Neward (CA, USA)
- VITROS Chemistry Products Calibrator Kit 10	Ortho Clinical Diagnostics, Neckargemuend (DE)

2.5 Antibodies

2.5.1 Primary Antibodies

Table 5: List of primary antibodies

Target	Assay	Species, clone	Dilution	Manufacturer/Source
- CD44	IHC	Mouse, monoclonal	1:50	Bio-Rad, MCA 643

-Collagen IV	IHC	Goat, polyclonal	1:50	Southern Biotech, 1340-01
- Crm 1	IF	Rabbit, polyclonal	1:50	Received from [107]
- DRG2	IF	Rabbit, polyclonal	1:50	GeneTex, GTX118599
- eIF4E	IF	Rabbit, monoclonal	1:50	Cell Signaling Technology, 2067
- GAPDH	WB	Mouse, monoclonal	1:1000	Novus Biologicals, NB 300-221
- Histone-H3	WB	Rabbit, monoclonal	1:1000	Cell Signaling Technology, 4499P
- Lamin A+C	WB	Rabbit, monoclonal	1:1000	Biorbyt, orb866297
- Mab414	IF	Mouse, monoclonal	1:50	Covance, MMS-120R
- Nestin	IF	Chicken, polyclonal	1:200	Novus Biologicals, NB 100-1604
- Nup 93	IF	Rabbit, polyclonal	1:50	Received from Prof. Dr. W. Antonin (Uniklinik Aachen)
- P53	IF	Mouse, monoclonal	1:50	Cell Signaling Technology, 2524
- P57	IF	Goat, polyclonal	1:50	Santa Cruz Biotech, sc-1039
- Ran	IF	Mouse, monoclonal	1:50	BD Biosciences, 610341
- SMCR8	IF	Rabbit, polyclonal	1:50	Sigma-Aldrich, HPA021557
- Vinculin	WB	Mouse, monoclonal	1:1000	Fitzgerald, RDI-CBL233

- WT-1	IHC, IF	Mouse, monoclonal	1:50	Santa Cruz Biotech, sc-7385
- WT-1	IF	Rabbit, monoclonal	1:200	Abcam, ab 89901

2.5.2 Secondary Antibodies

Table 6: List of secondary antibodies

Target	Assay	Conjugate	Source	Dilution	Manufacturer
- Anti-Chicken	IF	Alexa-555	Goat	1:200	Invitrogen, A 32932
- Anti-Goat	IHC	Biotinylated	Rabbit	1:200	Vector, BA 5000
- Anti-Mouse	IF	Alexa-488	Goat	1:200	Invitrogen, A 11001
- Anti-Mouse	IF	Alexa-674	Goat	1:200	Invitrogen, A 21237
- Anti-Mouse	IF	STAR RED		1:200	Abberior, STRED-1009
- Anti-Mouse	IHC	Biotinylated	Horse	1:200	Vector, BA 2001
- Anti-Mouse	WB	HRP	Sheep	1:10000	
- Anti-Rabbit	IF	Alexa-488	Goat	1:200	Invitrogen, A 11008
- Anti-Rabbit	IF	Alexa-647	Donkey	1:200	Invitrogen A 31573
- Anti-Rabbit	IHC	HRP	Goat	1:200	Vector
- Anti-Rabbit	WB	HRP	Goat	1:10000	

2.6 Software

Table 7: List of used software

Software	Manufacturer
- Adobe Photoshop CS3	Adobe, San José (CA, USA)
- BZ II Viewer/Analyzer	Keyence Deutschland GmbH, Neu-Isenburg (DE)
- CellProfiler	Broad Institute of MIT and Harvard, Cambridge (MA, USA)
- GraphPad Prism	GraphPad Software, San Diego (CA, USA)
- ImageJ	National Institutes of Health (NIH), Bethesda (MD, USA)
- Imaris	Oxford Instruments Imaris, Zurich (Switzerland)
- Microsoft Office 2016 (Word, Excel)	Microsoft Corporation, Redmond (WA, USA)

2.7 Pod-rtTA/histone-eGFP Mouse Line

The Pod-rtTA/histone-eGFP transgenic mouse line was kindly provided by Prof. Marcus J. Moeller (University Hospital Aachen, Germany). A schematic representation of the genetic design of this mouse model is shown in Figure 5. In this model, the podocyte-specific Nphs2 promoter drives the expression of the reverse tetracycline-controlled transactivator (rtTA), which in turn induces expression of the downstream tetracycline-responsive element (TRE) in a doxycycline-dependent manner. The TRE controls the expression of a histone-eGFP fusion protein, allowing for nuclear labeling of podocytes upon doxycycline administration. In the present study, only the Pod-rtTA/histone-eGFP component of this system (depicted above the dotted line in Figure 5) was utilized to achieve podocyte-specific nuclear labeling, while the Cre/LacZ reporter modules were not employed.

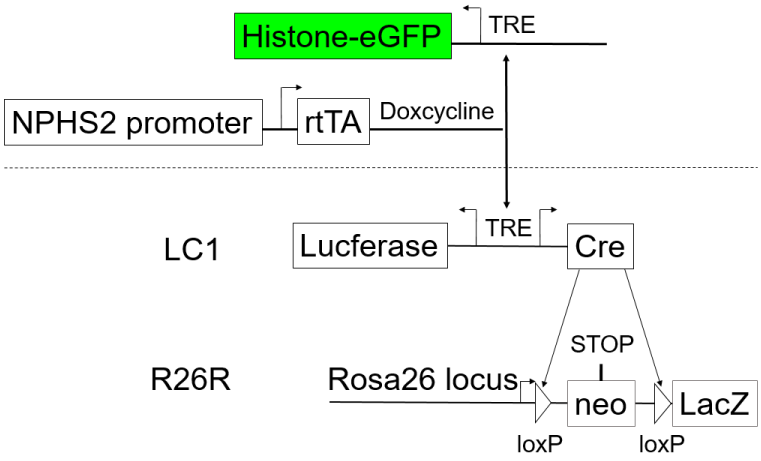


Figure 5. Schematic representation of doxycycline-inducible expression of histone-eGFP in podocytes using the Pod-rtTA/histone-eGFP transgenic mouse line. In this system, the NPHS2 promoter regulates expression of the reverse tetracycline-controlled transactivator (rtTA), which becomes active in the presence of doxycycline. rtTA binds to the tetracycline response element (TRE) and induces transcription of the Histone-eGFP reporter gene. This results in nuclear localization of eGFP specifically in podocytes. Modified from [108].

2.8 Munich Wistar Froemter (MWF) Rats

The MWF rat strain, which naturally develops focal segmental glomerulosclerosis (FSGS) as a result of genetic abnormalities, was used as an *in vivo* model to evaluate the effects of KPT-330. The first MWF mating pair was received as a gift from Dr. Angela Schulz and Prof. Reinhold Kreutz (Department of Clinical Pharmacology and Toxicology, Charité-Universitätsmedizin, Berlin, Germany).

3. Methods

3.1 Procedures Common to Mouse and Rat Experiments

3.1.1 Animal Husbandry and Care

All animal experiments were conducted in accordance with the German Animal Welfare Law and were approved by the relevant local authorities (State Agency for Nature, Environment and Consumer Protection of North Rhine-Westphalia, LANUV, NRW, Ref.-Nos. 81-02.04.2023.A015 and 81-02.04.2021.A471). The studies were performed at the Animal Facility of the University Hospital RWTH Aachen, Germany. Mice were housed under specific pathogen-free conditions, whereas rats were kept under standard housing conditions. All the animals were maintained in a 12 hour light cycle and were provided with standard mouse or rat chow and autoclaved tap water.

3.1.2 Animal Anesthesia

Mice were premedicated with Buprenovet (0.1 mg/kg body weight; subcutaneous injection volume: 3.3 ml/kg) 30 minutes before organ harvest. Anesthesia was induced by intraperitoneal injection of a ketamine/xylazine mixture (100 mg/kg and 20 mg/kg body weight, respectively; injection volume: 10 µl/g). The same procedure was followed to anaesthetize MWF rats, but a lower Buprenovet amount: 0,05 mg/kg 3,3 ml/kg bodyweight, was used.

3.1.3 Paraffin Tissue Block Preparation

After anesthesia, the kidneys were removed from the animals and carefully decapsulated. Kidney tissues were fixed in either methyl-Carnoy's solution (comprising 60% methanol, 30% chloroform, and 10% glacial acetic acid), 3% paraformaldehyde (PFA), or 4% formaldehyde, followed by paraffin embedding.

3.2 Mouse Experiments

3.2.1 Kidney Tissue Clearing and 3D Imaging

Kidney tissues were collected as described above. Approximately 1 mm-thick tissue sections were dissected and immediately immersed in 4% PFA for fixation. The samples were fixed in 4% PFA for 24 hours, followed by a 12-hour wash in phosphate-buffered saline (PBS) to remove residual fixative. Tissue dehydration was performed by incubating the samples in fresh absolute ethanol for two cycles

of 30 minutes each. All incubation steps were carried out on a shaker at room temperature. After dehydration, tissues were transferred into pure ethyl cinnamate for optical clearing until they became visibly transparent at room temperature.

Three-dimensional imaging was performed, at the two-photon imaging core facility of the Interdisciplinary Center for Clinical Research (IZKF) Aachen within the Faculty of Medicine at RWTH Aachen University, using an Olympus FV1000MPE two-photon laser scanning microscope equipped with a 25x water immersion objective (numerical aperture: 1.05) and a correction collar for refractive index adjustment. An excitation wavelength of 820 nm was applied for eGFP signal detection. Image processing and analysis were conducted using Imaris software, “Spots” function. For each experimental group, kidney tissues from 5-8 animals were analyzed, and 8-10 glomeruli per animal were evaluated.

3.2.2 Histochemistry and Immunofluorescence

For tissue overview, one-micrometer-thick sections fixed with methyl-Carnoy’s solution were stained with periodic acid-Schiff (PAS) reagent and counterstained with hematoxylin.

Immunofluorescence (IF) staining for SMCR8, Ran, eIF4E, and DRG2 was performed on 1 µm-thick PFA-fixed sections using a triple-labeling protocol that included nestin and WT-1 to quantify the podocyte-specific nuclear-to-cytoplasmic signal intensity ratio. Slides were deparaffinized in xylene and rehydrated through a graded ethanol series. Antigen retrieval was conducted by microwave heating the sections in a citrate-based unmasking solution at 600 W for three cycles of five minutes each. The sections were then allowed to cool for approximately 45 minutes and subsequently blocked with 3% bovine serum albumin (BSA) in PBS for 1 hour in a humidified chamber. For primary staining, the sections were incubated overnight at 4 °C with WT-1 together with SMCR8, Ran, eIF4E, or DRG2 primary antibodies, followed by 30 minutes of incubation with fluorophore-conjugated secondary antibodies on the following day at room temparature. The sections were then incubated with nestin primary antibody for 1 hour at room temperature, followed by the same secondary antibody incubation step. All the primary and secondary antibodies were diluted in PBS containing 3% bovine serum albumin (BSA). Between each primary and secondary antibody incubation, the sections were washed twice with PBS for 5 minutes each. Finally,

nuclei were counterstained with DAPI, and the sections were mounted with Immu-Mount and covered with coverslips.

3.2.3 Labeling of Podocytes

Primary podocytes were isolated using the Pod-reverse tetracycline-controlled transactivator (Pod-rtTA)/histone-eGFP transgenic mouse line.

To evaluate the efficiency of doxycycline-induced eGFP expression in podocytes, two induction protocols were compared using mice aged approximately 35 weeks. One mouse received an intraperitoneal injection of doxycycline hyclate at a dose of 50 µg/g body weight 24 hours prior to euthanasia. The other mouse was administered doxycycline hyclate via drinking water (2% doxycycline with 5% sucrose) for 14 consecutive days. Doxycycline-containing water was protected from light and replaced every two days.

3.2.4 Isolation of Primary Podocytes from Pod-rtTA/Histone-eGFP Mice at Different Ages

For the purpose of podocyte isolation to assess age-related changes in podocyte compartmentalization, Pod-rtTA/histone-eGFP transgenic mice were categorized into three age groups: 11 ± 3 weeks (young), 35 ± 3 weeks (adult) and 80 ± 3 weeks (aged). Approximately 50 mice from each age group were used to isolate primary podocytes. Doxycycline was administered via drinking water as described in 2.2.3.1.

After anesthesia, blood samples were collected from eyes, transcardial perfusion was performed via the left ventricle using 0.9% NaCl. The kidneys were then dissected, decapsulated, and transferred into 15 ml tubes containing RPMI 1640 complete medium. All the above procedures were performed at room temperature. The protocol for isolating primary podocytes was adapted from Boerries et al. [109] and Wang et al. [110], incorporating several modifications aimed at reducing experimental costs without compromising cell yield or purity.

Part A: Glomeruli Isolation

The kidneys were transferred into a 10 cm culture dish containing RPMI 1640 complete medium and finely minced into small fragments using a sterile scalpel at room temperature. The tissue pieces were then collected by centrifugation at 1200 rpm for 5 minutes at 4 °C. After discarding the supernatant, 3 ml of digestion buffer per animal was added to the pellet. Enzymatic digestion was carried out in

a 37 °C water bath for three cycles of 5 minutes each, with gentle pipetting up and down after every interval to facilitate dissociation.

The kidney tissue suspension was then passed through a 70 µm nylon mesh cell strainer, which was continuously rinsed with cold HBSS buffer during the filtration process to ensure efficient glomerular recovery. The filtrate was subsequently passed through a 40 µm nylon mesh cell strainer. At this step, tubular fragments passed through the mesh, while the glomeruli were retained on top of the 40 µm strainer.

To recover the glomeruli, the surface of the 40 µm mesh was gently rinsed using a syringe-needle system with cold HBSS buffer. The resulting glomeruli-containing buffer was collected into a 50 ml conical tube and subjected to centrifugation at 1200 rpm for 5 minutes at 4 °C to pellet the isolated glomeruli.

Part B: Podocyte Isolation

The glomerular pellet obtained from one mouse was resuspended in 2 ml of digestion buffer and evenly distributed into two 1.5 ml Eppendorf tubes. These tubes were placed on a thermomixer shaker at 37 °C and agitated at 1400 rpm. The digestion and mechanical dissociation process was carried out as follows:

5 min: Mixed by gentle pipetting up and down.

10 min: Brief vortexing, followed by pipetting.

15 min: Mixed by pipetting up and down.

20 min: Short vortexing, followed by pipetting.

25 min: Mixed by pipetting up and down.

30 min: Mixed by pipetting up and down.

35 min: Short vortexing, followed by pipetting.

40 min: Glomeruli were sheared using a 27G needle attached to a syringe to enhance cell dissociation.

45 min: Mixed by pipetting up and down.

50min: Final pipetting to ensure complete dissociation.

The entire digestion procedure was monitored under a fluorescence microscope to assess the detachment of eGFP-positive podocytes. Once most of the $eGFP^+$ cells were released, the cell suspension was centrifuged at 1500 rpm, 4 °C for 5

minutes. The supernatant was discarded, and the cell pellet was resuspended in 800 µl of FACS buffer per mouse. The suspension was filtered through a 35 µm cell strainer into FACS tubes. Subsequently, eGFP$^+$ cells were sorted at 37 °C using a FACS Canto II™ flow cytometer at the flow cytometry core facility of the Interdisciplinary Center for Clinical Research (IZKF) Aachen within the Faculty of Medicine at RWTH Aachen University.

Digestion buffer:

5.075 mg	Collagenase II (325 U/mg)
3.75 ml	Protease from Streptomyces griseus
500 U	DNase I

Adjusted to 5 ml final volume with cold HBSS buffer

FACS buffer:

0.5% (w/v)	BSA
2 mM	EDTA

Adjusted to final volume with HBSS buffer

Filter sterilized (0.22 µm) and stored at 4 °C until use

3.2.5 Nuclear and Cytoplasmic Protein Extraction

Sorted eGFP$^+$ podocytes were centrifuged at 1600 rpm for 5 minutes at 4 °C to remove residual FACS buffer. To minimize BSA contamination, cells were washed twice with 1 ml Buffer A supplemented with protease and phosphatase inhibitor cocktail (1x) and 0.5 µl/ml 1 M DTT. Following centrifugation, the cell pellet was resuspended in 30 µl Buffer A (supplemented as above), and the suspension was frozen at -80 °C to disrupt the plasma membrane. After rapid thawing, 0.1% NP-40 was added, and the sample was incubated on ice for 5 minutes to facilitate selective membrane permeabilization. The sample was centrifuged at 2600 rpm for 10 minutes at 4 °C, and the resulting supernatant was collected as the cytoplasmic protein fraction. The remaining nuclear pellet was washed with 1 ml Buffer A and centrifuged at 3500 rpm for 10 minutes at 4 °C. This washing step was repeated two additional times (for a total of three washes) to ensure removal of cytoplasmic contaminants. The clean nuclear pellet was then resuspended in 20 µl Buffer C, also supplemented with protease and phosphatase inhibitor cocktail (1x) and 0.5 µl/ml 1 M DTT. The sample was

incubated on ice for 15 minutes, with vigorous vortexing every 5 minutes to enhance nuclear protein solubilization. The final centrifugation step was performed at 13,000 rpm for 10 minutes at 4 °C, and the supernatant was collected as the nuclear protein fraction.

Note: All buffers (Buffer A and Buffer C) were supplemented freshly with protease and phosphatase inhibitor cocktail (1x) and 0.5 µl/ml 1 M DTT immediately prior to use.

Buffer A

Reagent	Stock solution	Volume added	Final concentration
HEPES (pH 7.9)	1 M	2.5 ml	10 mM
KCl	1 M	2.5 ml	10 mM
$MgCl_2$	1 M	375 µl	1.5 mM
H_2O	—	to 250 ml	—

Buffer C

Reagent	Stock solution	Volume or amount	Final concentration
HEPES (pH 7.9)	1 M	5 ml	50 mM
NaCl	5 M	3 ml	150 mM
EGTA	0.5 M	40 µl	0.2 mM
EDTA	0.5 M	40 µl	0.2 mM
0.5% sodium deoxycholate	—	0.5 g	0.5% (w/v)
H_2O	—	to 100 ml	—

3.2.6 Protein Concentration Measurement

The protein concentrations of cytoplasmic and nuclear fractions were determined using the NanoOrange™ Protein Quantitation Kit according to the manufacturer's protocol. Briefly, the concentrated NanoOrange protein quantitation diluent was first diluted 10-fold with distilled water to prepare a 1x protein quantitation diluent. For each assay, 2.5 ml of the 1x diluent was used. Subsequently, the 1x NanoOrange reagent working solution was prepared by diluting the NanoOrange protein quantitation reagent (Component A) 500-fold in the 1x protein quantitation

diluent prepared above. The working solution was protected from light throughout the assay to prevent photodegradation of the dye.

Bovine serum albumin (BSA) standards were then prepared as follows:

Volume of BSA solution (µl)	Volume of 1x NanoOrange Working Solution (µl)	Final BSA Concentration (µg/ml)
0	250	0
5 µl 2 mg/ml BSA stock	995	10
420 µl 10 µg/ml	280	6
300 µl 6 µg/ml	300	3
300 µl 3 µg/ml	600	1
420 µl 1 µg/ml	280	0.6
300 µl 0.6 µg/ml	300	0.3
300 µl 0.3 µg/ml	600	0.1
420 µl 0.1 µg/ml	280	0.06
300 µl 0.06 µg/ml	300	0.03
300 µl 0.03 µg/ml	600	0.01

The cytoplasmic and nuclear protein samples were diluted at a ratio of 1:220 with the prepared NanoOrange working solution. Subsequently, both the diluted protein samples and BSA standards were incubated at 90 °C for 10 minutes in the dark. After incubation, the samples were allowed to cool in dark to room temperature for 20 minutes. Following cooling, 200 µl of each sample and standard was transferred into a black 96-well microplate. Fluorescence was measured using a plate reader with excitation set at 485 nm and emission captured at 590 nm. The resulting optical density (OD) values were used to calculate protein concentrations based on the standard curve generated from the BSA standards.

3.2.7 Western Blot

To assess the quality and purity of the nuclear and cytoplasmic protein fractions, samples were first denatured by heating at 95 °C for 5 minutes. Protein concentrations were adjusted to equal levels across all samples. Equal amounts of protein were mixed with loading buffer at a 4:1 (sample: buffer) ratio and loaded onto a 10% SDS-polyacrylamide gel for electrophoresis, which was carried out at

a constant voltage of 120 V. Following separation, proteins were transferred onto a nitrocellulose membrane using a blotting chamber at 100 V for 1 hour. After transfer, the membrane was rinsed once with TTBS (Tris-buffered saline containing 0.1% Tween-20), then blocked with 2% BSA in TTBS for 1 hour on a shaker at room temperature to prevent nonspecific antibody binding. The membrane was then incubated with the appropriate primary antibody diluted in TTBS either for 1 hour at room temperature or overnight at 4 °C. This was followed by five washes with TTBS (5 minutes each). Subsequently, the membrane was incubated with a horseradish peroxidase (HRP)-conjugated secondary antibody diluted in TTBS for 1 hour at room temperature, followed by another series of five 5-minute washes with TTBS. Protein bands were visualized using the Lumi-Light Western Blotting Substrate (Chemiluminescent HRP substrate), and signal detection was performed according to the manufacturer's instructions.

Running buffer:

28.8 g	glycien
6.04 g	Tris base
2 g	SDS
ad 2 l	ddH_2O

Transfer buffer:

28.8 g	glycien
6 g	Tris
400 ml	Methanol
ad 2 l	ddH_2O

TTBS (Tris-Tween 20 buffered saline)

50 ml	1M, pH 8 Tris
60 ml	5M NaCl
8 ml	25% Tween-20 pH7.4
ad 2 l	ddH_2O

3.2.8 Mass Spectrometry Analysis of Different Protein Fractions

Mass spectroscopy analysis was performed in collaboration with proteomics facility in EMBL, Heidelberg. Following peptide digestion, the peptide fractions are labeled using TMTsixplexTM reagent and separated by immobilized pH-gradient-isoelectric focusing (IPG-IEF) using HiRIEF method. The concentrated peptides are then separated using an Ultimate 3000 RSLCnano system coupled to a Q-Exactive Plus mass spectrometer to separate the protein fractions. Peptide and protein identification is done and heat maps are generated (from three biological replicates for each condition) to visualize the data.

3.3 Rat Experiments

3.3.1 *In Vitro* Drug Testing

3.3.1.1 Cell Culture, Plasmids and siRNA Transfection

HeLa Kyoto cells stably expressing GFP-NLS were cultured in Dulbecco's Modified Eagle Medium supplemented with 10% (v/v) heat-inactivated fetal bovine serum and 1% (v/v) penicillin/streptomycin at 37°C in a humidified atmosphere containing 5% CO_2. Cells were routinely screened to confirm the absence of mycoplasma contamination. For live-cell imaging experiments, cells were transfected with either siRNA targeting Nup93 (5′-CGGCAGAUGUCAAGGCGUCdTdT-3′; 20 nM) or a non-targeting control siRNA (20 nM) using Lipofectamine RNAiMAX, following the manufacturer's protocol. Transfected cells were seeded on µ-Slide 8-well high and incubated for 48 hours at 37°C with 5% CO_2. 5x10⁴ cells from each condition were lysed in 2x SDS-sample buffer after harvested and were analyzed following the same Western Blot method described above to assess the transfection efficiency. Image analysis was performed using ImageJ.

Forty-eight hours post-transfection, cells were treated with either 5% 1,6-hexanediol, KPT-330, or leptomycin B. Treatments with KPT-330 or Leptomycin B (LMB) were performed for 2 hours prior to imaging, whereas 5% 1,6-hexanediol was applied for 5 minutes. Chromatin was labeled with silicon-rhodamine DNA probe according to the manufacturer's instructions.

3.3.1.2 Western Blot

To determine the extent to which Nup93 expression was reduced following each treatment, Western blot analysis was performed. For each condition, 5 × 10⁴ cells

were lysed in 2× SDS sample buffer containing 10 mM Tris-HCl (pH 7.5), 150 mM NaCl, 0.5 mM EDTA, 0.5% NP-40, and a protease/phosphatase inhibitor cocktail. Subsequent steps were carried out as described in Section 3.2.7, except that a 5% non-fat dry milk solution was used for both blocking and antibody dilution. Image acquisition and densitometric analysis were conducted using ImageJ software.

3.3.2 *In Vivo* Intervention in an FSGS Rat Model by Using the Nuclear Transport Inhibitor KPT-330

Male MWF rats were exclusively chosen for the experiments, since previous studies have shown that males are more prone to developing severe kidney injury and a pronounced FSGS phenotype in this strain [44, 111].

Group assignment at week 10 was based on comparable body weight. Fourteen rats received the “solvent” as a control (0.6% (w/v) poloxamer Pluronic F-68 surfactant and 0.6% (w/v) polyvinylpyrrolidone (PVP) K-29/32 Polymer) at a dose of 6.25 ml/kg body weight. Another group of fifteen rats was treated with KPT-330 in solvent solution at a dosage of 12.5 mg/kg body weight, administered orally twice per week for a duration of 10 weeks using a feeding needle. Treatment commenced at 10 weeks of age, a time point before the onset of severe histological FSGS in MWF rats, although early signs of increased blood pressure and gradual kidney function decline were already evident.

The MWF rats were assigned to two experimental approaches: Approach A involved the immediate post-treatment evaluation (also referred to as “20-week group”, Fig. 6A): To assess the direct impact of KPT-330 following the treatment period, five rats from the vehicle (= “solvent”) group and five from the KPT-330 group were euthanized at week 20 (directly after treatment stop), and their kidneys were collected for further analysis. Approach B involved an extended follow-up (also referred to as “40-week group”, Fig. 6B): Animals were treated like in approach A either with vehicle (= “solvent”, initially n=9; one rat died at week 18 due to handling during gavage, and another was excluded at week 35 due to a serious foot injury) or KPT-330 in vehicle (n=10) from week 10 to week 20, followed by a drug-free period from week 20 to week 40. At week 40, all remaining rats were euthanized, and their kidneys were collected for histological and molecular analyses.

Two completely untreated MWF control groups were included (Fig. 6C): a 10-week MWF control and a 40-week MWF control group, each comprising six rats. Kidney tissues were harvested at weeks 10 and 40, respectively, for comparative analysis.

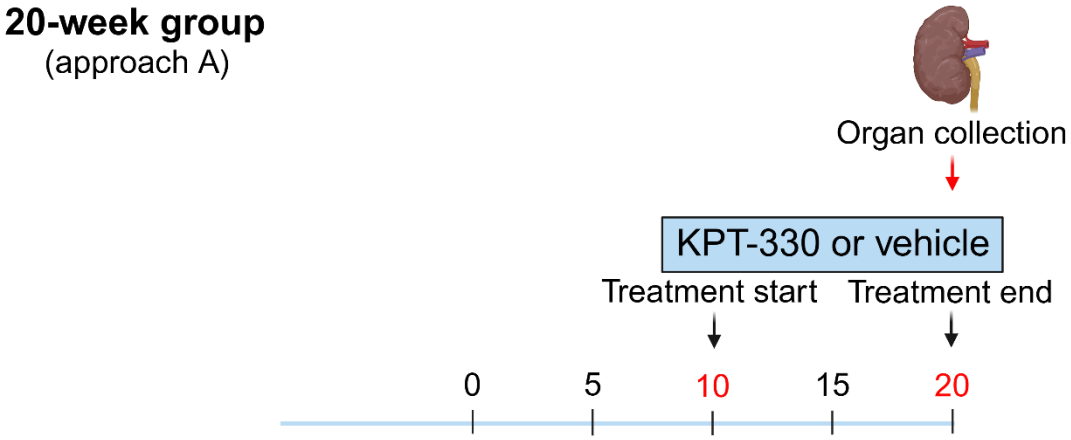


Figure 6A. Experimental design for the 20-week group. Rats were orally administered either vehicle (0.6% w/v poloxamer Pluronic F-68 + 0.6% w/v polyvinylpyrrolidone [PVP] K-29/32) or KPT-330 (12.5 mg/kg), twice weekly from week 10 to week 20. Kidneys were collected at week 20 (approach A; n=5 per treatment group).

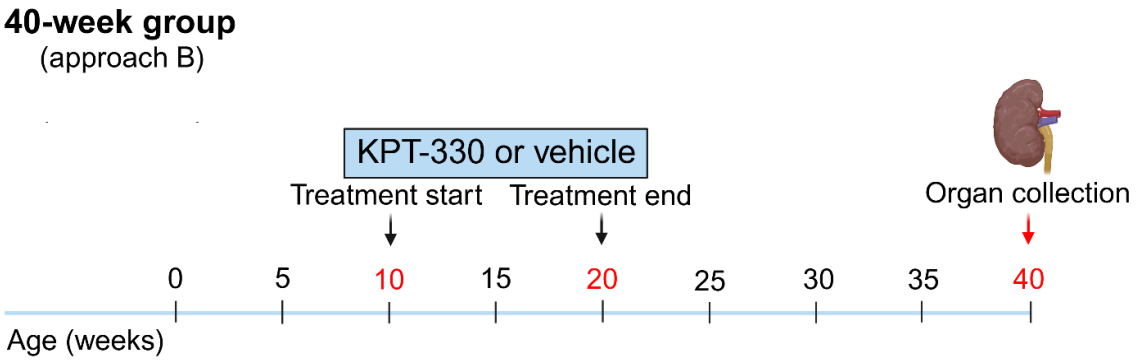


Figure 6B. Experimental design for the 40-week group. Rats were orally administered either vehicle (same formulation as in panel A) or KPT-330 (12.5 mg/kg), twice weekly from week 10 to week 20. Afterwards, animals were left untreated until week 40 (approach B; The vehicle group started with n=9, with two animals lost at weeks 18 and 35; the KPT-330 group began with n=10).

Control groups

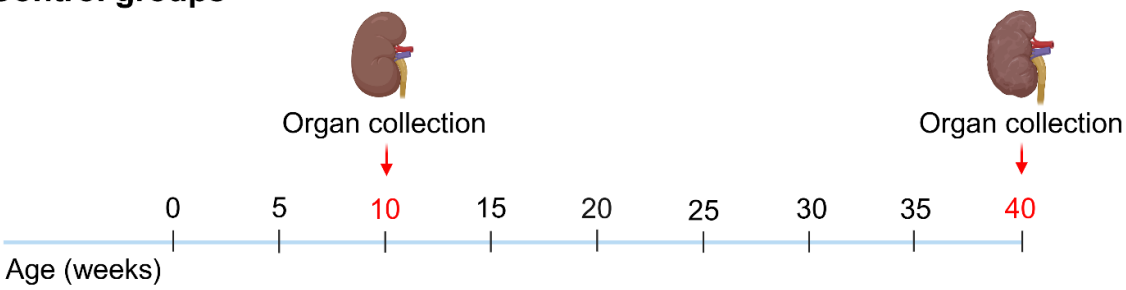


Figure 6C. Experimental design for the untreated control groups. Two untreated MWF control cohorts were included: a 10-week control group (n=6) and a 40-week control group (n=6).

3.3.3 Serum and Urine Collection, Biochemical Analyses, and Blood Pressure Monitoring

In both the approach B cohort and the 40-week control group, animals underwent assessments beginning at 5 weeks of age, with evaluations conducted at 5-week intervals until 40 weeks. Peripheral blood samples were collected from the tail vein, while urine samples were obtained via 15-hour individual housing in metabolic cages. Systolic blood pressure was measured using a noninvasive tail-cuff system connected to an automated sphygmomanometer. Body weight was recorded twice weekly following the initiation of treatment.

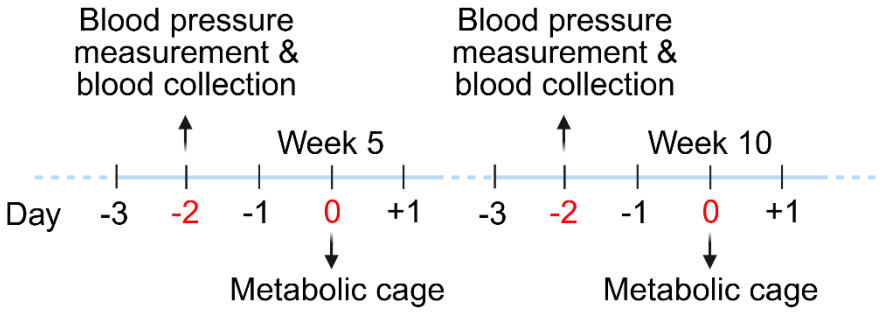


Figure 7. Blood pressure measurement and sample collection. For the approach B cohort and the 40-week untreated control group, the above procedures were performed every 5 weeks starting from week 5: blood pressure was monitored, urine and blood samples were collected for subsequent analyses.

Hematological parameters, including mean corpuscular volume (MCV) and mean corpuscular hemoglobin (MCH), were determined using an automated veterinary hematology analyzer with EDTA-anticoagulated whole blood. Serum biochemical markers, namely creatinine, blood urea nitrogen (BUN), total cholesterol, triglycerides, phosphate and electrolytes (sodium and potassium) were measured using the VITROS XT 3400 Chemistry System equipped with UPRO slides and

the VITROS Chemistry Products Calibrator Kit 10. Urinary albumin and serum cystatin C concentrations were measured using ELISA kits.

3.3.4 Histochemistry, Immunohistochemistry and Immunofluorescence

PAS staining was performed as described in Section 3.2.2. IF staining for XPO1, Nup93, and p53 was carried out using the triple-labeling protocol. Specifically, XPO1 and Nup93 staining were performed on 1 µm-thick formalin-fixed sections, whereas 1 µm-thick PFA-fixed sections were used for p53 analysis. Following a similar procedure, double staining of WT-1 and mab414 was performed on 3 µm-thick PFA-fixed sections to quantify NPCs in podocytes.

For IHC, 1 µm-thick methyl-Carnoy's-fixed sections were used for CD44 and collagen IV staining, while formalin-fixed sections of the same thickness were used for WT-1 staining. The initial steps were identical to those described for IF staining, until the blocking step. In IHC, sections were blocked with 3% hydrogen peroxide (H_2O_2) for 10 minutes to quench endogenous peroxidase activity. All sections were incubated with primary antibodiesfor 1 hour, followed by a 30-minute incubation with biotinylated or HRP-conjugated secondary antibodies. All primary and secondary antibodies were diluted in PAS containing 1% BSA. To enhance signal detection in IHC, a tyramide signal amplification (TSA) step was applied using the TSA Plus Biotin Kit for CD44 and WT-1 staining. Briefly, after the H_2O_2 blocking step, the sections were incubated with Avidin for 10 minutes, followed by two washes with PBS (5 minutes each) and incubation with Biotin for 10 minutes. Subsequent procedures were performed as described above until the completion of the secondary antibody incubation. The sections were then incubated with streptavidin-HRP (1:400 in 1% BSA/PBS) for 15 minutes, followed by a TSA incubation step (1:100 in Amplification Diluent) for 5 minutes, after which the SA-HRP incubation was repeated. All the above procedures were performed at room temperature.

Signal visualization was achieved using a diaminobenzidine (DAB) substrate in combination with the Vectastain ABC Kit at 37 °C in a shaking water bath. All subsequent steps, including counterstaining with 0.5% methyl green, dehydration through ascending ethanol concentrations (starting from 70%), clearing in xylene, and mounting with Histokitt followed by coverslipping, were performed at room temperature.

3.3.5 Microscopy and Image Analyses

Glomerulosclerosis was evaluated in PAS-stained kidney sections by scoring each glomerulus based on the proportion of sclerotic or fibrotic area within the glomerular cross-section, as follows: score 0 = 0%, score 1 = 1-25%, score 2 = 26-50%, and score 3 = 51-100%. In addition, the frequency of glomeruli exhibiting synechiae was assessed using the same PAS-stained sections. All glomeruli present in the respective sections were included in the analysis of both glomerulosclerosis and glomerular synechiae.

WT-1 positive podocyte nuclei were counted at 400x magnification across all glomeruli on each slide. For quantification of glomerular CD44 expression, approximately 20 consecutive images covering a minimum of 30 glomeruli in the renal cortex of each animal were captured at 200x magnification using a Keyence BZ9000 fluorescence microscope. The percentage of CD44-positive area within glomeruli was quantified using ImageJ software via computer-assisted morphometric analysis, and the mean stained area was calculated. Collagen IV expression was evaluated by scoring the stained area within the glomerular tuft using the following semi-quantitative scale: 0 = 0% of glomerular area stained, 1 = 1-25%, 2 = 26-50%, 3 = 51-75%, and 4 = >75% [112, 113]. All glomeruli in each sample were included in the scoring.

Live-cell imaging was carried out on a Nikon Ti2-E spinning disk confocal microscope equipped with Plan-Apochromat 10x NA 0.5 and 60x NA 1.42 oil-immersion objectives. Cells were maintained under physiological conditions using an UNO-T-H-CO2 environmental controller. Fluorescence excitation was provided by a SpectraX LED light engine with GFP and Cy5 filter sets, and images were captured with a Digital Sight 10 CCD camera. Image acquisition and initial analysis were performed with NIS-Elements, followed by processing in ImageJ and CellProfiler [114].

To quantify nuclear pore complexes (NPCs), stimulated emission depletion (STED) microscopy was applied to sections co-stained with mab414 and WT-1. Imaging was conducted using an inverted Leica SP8 Tau-STED3x microscope equipped with a Leica HC PL APO 93x NA 1.30 glycerol-immersion STED objective and appropriate filter sets. Image processing was done with ImageJ and Imaris software. For each cell, a four-slice image stack was acquired and collapsed into a single image via mean intensity projection. Podocyte nuclei were

identified based on WT-1 signals using the ‘surface’ function in Imaris with automatic thresholding, while NPCs were defined by the mab414 signal using the ‘spots’ function with a 100 nm diameter setting. Imaris was used to quantify the number of NPCs per nucleus and the distance to their three nearest neighbors. Imaging and analysis were performed at core facility for 3D Super-Resolution (3DSR) at RWTH Aachen University.

Quantification of the nuclear-to-cytoplasmic fluorescence intensity ratios for XPO1 and p53, as well as the intensity of Nup93 at the nuclear envelope, was conducted on kidney sections stained with corresponding antibodies and co-labeled with WT-1 and nestin to mark podocyte nuclei and cytoplasm, respectively. For p53 and Nup93 analysis, images were acquired at 400x magnification using a Keyence BZ9000 fluorescence microscope with a Plan-Apochromat 40x/0.75 air objective. For XPO1 analysis, images were acquired at 630x magnification using a Zeiss LSM 710 inverted confocal laser scanning microscope with a Plan-Apochromat 63x/1.4 oil-immersion objective.

All acquired images were pre-processed using a custom pipeline in ImageJ, and further quantitative analysis was performed with CellProfiler software [114]. To calculate nuclear-to-cytoplasmic fluorescence intensity ratios, color images were converted to 8-bit grayscale and smoothed using a Gaussian filter. WT-1 signal was used to identify nuclei via global robust background thresholding, with a nucleus diameter range of 15-40 pixels and a threshold between 0.6 and 1. Nestin staining defined the cytoplasm, segmented using an adaptive Otsu two-class threshold with a 15-pixel window and the Distance-B method for secondary object definition. Threshold limits ranged from 0.1 to 1. Object de-clumping and local maxima spacing were automatically determined. The “Measure Object Intensity” module was used to quantify p53 and XPO1 signals in the nucleus and cytoplasm, from which signal intensity ratios were derived. Cells that were incomplete or in contact with image borders were excluded from analysis.

For Nup93 intensity measurements at the nuclear envelope, podocyte nuclei were identified using the same parameters. The nuclear envelope region was defined by expanding and subsequently shrinking each nucleus by 2 pixels; subtraction of the shrunken area from the expanded region yielded the envelope boundary, within which signal intensity was calculated.

All histological and imaging evaluations were performed in a blinded manner unaware of group allocation.

3.4 Statistical Analysis

Data are expressed as mean ± standard deviation (SD). All statistical analyses were performed using GraphPad Prism software (version 10.4.1; GraphPad Software Inc., San Diego, CA, USA). Outliers were identified and excluded using the ROUT method with a false discovery rate (FDR) of 10% for each dataset. Subsequent analyses were conducted using the cleaned datasets.

Normality of data distribution was assessed via the Shapiro-Wilk test. Comparisons between two groups were conducted using a two-tailed unpaired Student's t-test for normally distributed data, or the Mann-Whitney U test for non-parametric data. For comparisons involving more than two groups, one-way ANOVA followed by Fisher's LSD post hoc test was applied for parametric data, whereas the Kruskal-Wallis test was used for non-parametric comparisons. Statistical significance was defined as follows: *$p < 0.05$; **$p < 0.01$; ***$p < 0.001$; ****$p < 0.0001$.

4 Results

4.1 Characteristics of Aging Mouse Kidneys with a Focus on Mislocalized Podocyte Biomarkers

4.1.1 Structural and Functional Changes in the Aging Kidney

Aging is accompanied by progressive alterations in renal architecture and function [115, 116]. To characterize these age-associated changes at both the structural and physiological levels, three-dimensional (3D) imaging analyses and functional assessments of kidneys from young and aged mice were performed in the mouse model used in this study.

4.1.1.1 Kidney 3D Imaging Reveals a Decrease in Podocyte Number During Aging

Using a tissue-clearing method, the average number of podocytes per glomerulus was quantified within 1-mm-thick kidney sections. Images were acquired by two-photon microscopy. eGFP-positive podocytes were detected and automatically marked in blue using the “spots” function in Imaris (Fig. 8A). However, due to tissue autofluorescence, not all podocytes could be accurately identified by the software. Cells that could not be distinguished from the background were therefore manually annotated in pink or white (Fig. 8A). Individual glomeruli were selected for counting. Quantitative analysis (Fig. 8B) showed that the podocyte number remained relatively stable between 11- and 35-week-old mice (74.95 ± 9.03 vs. 71.27 ± 11.33). In contrast, a significant reduction was observed between 35 and 80 weeks of age, with the average podocyte number decreasing to 48.21 ± 13.68 per glomerulus.

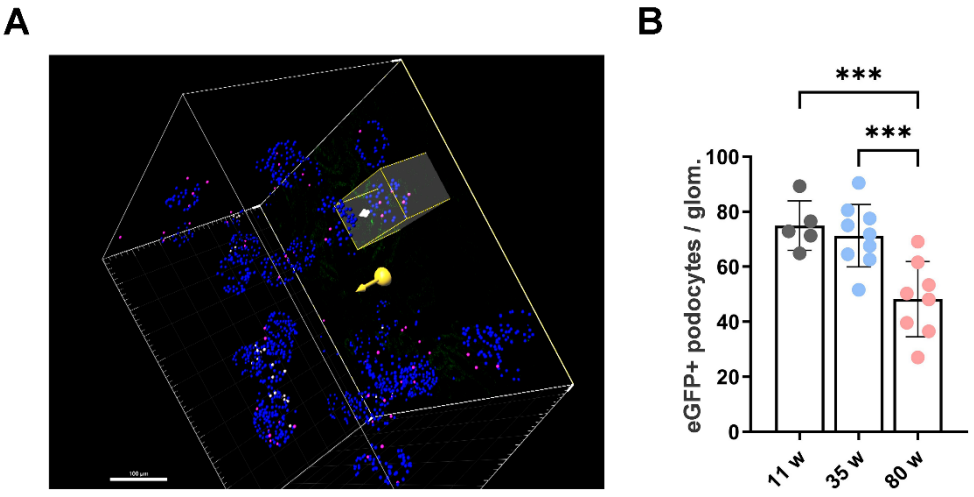


Figure 8. Quantification of the average number of podocytes per glomerulus in 3D reveals a marked podocyte loss at 80 weeks of age. (A) A three-dimensional (3D) reconstruction was generated from a representative kidney tissue volume. Blue dots indicate eGFP$^+$ podocytes automatically detected by Imaris software, whereas pink and white dots denote manually added eGFP$^+$ podocytes. The selected single glomerulus is outlined with a yellow circle. **(B)** The average number of podocytes per glomerulus was quantified in mice aged 11 weeks (n = 5), 35 weeks (n = 9), and 80 weeks (n = 8). Data are shown as mean ± SD. ***P < 0.001. Scale bar: 100 µm.

4.1.1.2 Mice Develop Age-Related Glomerular Synechiae

Glomerular synechiae, defined as an adhesion between the glomerular tuft and Bowman's capsule, represent an early lesion in post-adaptive FSGS [117]. To evaluate glomerular morphological lesions and early signs of FSGS across our age groups, PAS staining was performed to assess potential histological changes. Consistent with the age-dependent decrease in podocyte number (Figs. 8A, B), the frequency of synechiae showed a slight increase between 11 and 35 weeks of age and rose significantly from 35 to 80 weeks (Fig. 9A; P < 0.05 for 35 vs. 80 weeks; **P < 0.001 for 11 vs. 80 weeks). In contrast, the glomerulosclerosis score did not differ significantly among age groups and remained relatively stable even at 80 weeks (Fig. 9B).

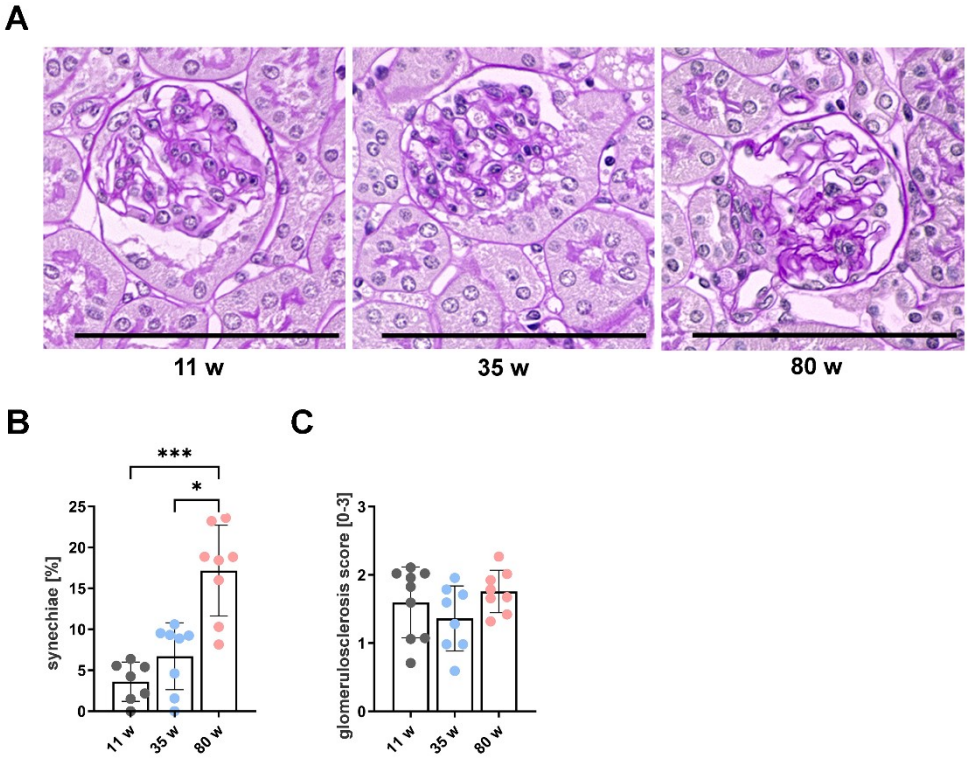


Figure 9. Age-related increase in the formation of glomerular synechiae without a significant change in the severity of glomerulosclerosis. (A) Representative PAS-stained kidney sections showing glomeruli from 11-, 35-, and 80-week-old mice. **(B)** The frequency of glomeruli exhibiting synechiae between the capillary tuft synechiae between the capillary tuft and Bowman's capsule, and **(C)** the severity of glomerulosclerosis were assessed. 11-week group, n=7-9; 35- and 80-week groups, n=8. Data are shown as means ± SD. *P < 0.05, *** P < 0.001. Scale bar: 100 µm.

4.1.1.3 Kidney Function Declines Slightly with Aging

Serum cystatin C levels were measured to evaluate age-associated changes in kidney function between week 11 and week 80 (Fig. 10). Cystatin C concentrations remained largely unchanged among 11-, 35-, and 80-week-old mice (0.60 ± 0.12, 0.59 ± 0.18, and 0.68 ± 0.18 µg/ml, respectively), indicating that overall kidney filtration capacity was maintained with age. Although a slight upward trend was observed in aged animals, the difference did not reach statistical significance. These data suggest that, despite evident structural changes in the aging kidney, functional decline remains modest within this time frame.

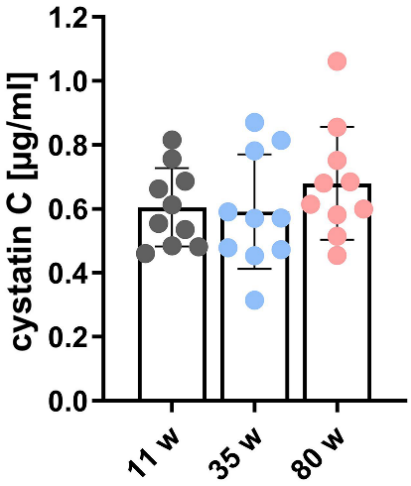


Figure 10. Kidney function remains largely preserved during aging. Serum cystatin C levels in mice at 11, 35, and 80 weeks of age. n=10 per group. Data are shown as means ± SD.

Together, these findings highlight coordinated structural and functional changes that occur in the kidney as part of the natural aging process.

4.1.2 Identification of Known and Novel Mislocalized Podocyte Biomarkers in Aging Mouse Kidneys

To investigate age-dependent protein mislocalization in podocytes, an imaging workflow for quantifying nuclear-to-cytoplasmic (N/C) intensity ratios of interested proteins was established. Several proteins known to undergo age-related redistribution in other post-mitotic cells were analyzed to determine whether similar changes occur in podocytes. The same approach was then applied for the discovery of novel podocyte-specific mislocalized proteins.

4.1.2.1 Establishment of an Imaging Analysis Work Flow for Calculating Nuclear-to-Cytoplasmic Ratios of Proteins

A semi-automated image analysis pipeline was established in *CellProfiler* to quantify the N/C ratio of candicate proteins. To enable separation of the

cytoplasmic and nuclear compartments of podocytes, triple immunofluorescence staining was performed using nestin as a cytoplasmic marker, p57 as a nuclear marker, and the candidate protein co-stained on the same tissue section. β-Tubulin triple staining was used as an example to illustrate the analytical workflow and to validate the reliability of the pipeline (Fig. 11).

First, in the “Input” step, images from each fluorescence channel were imported into *CellProfiler*, and individual glomeruli-or in some cases adjacent glomeruli, depending on the local background intensity-were manually selected. The images were then converted to grayscale, and the primary structures corresponding to nestin and p57 signals were identified in the “Image processing” step. Since podocytes have a three-dimensional architecture, nestin staining from the cytoplasmic extensions above the nucleus sometimes overlapped with p57 signals, producing apparent false co-localization. To more accurately delineate the two compartments, a tertiary nestin mask was generated by subtracting the p57-positive nuclear area from the primary nestin cytoplasmic mask. Next, nestin-positive cytoplasmic regions belonging to the same glomerulus were grouped and paired with the corresponding p57-positive nuclei from that glomerulus. A comparison between the original immunofluorescence images and the final reconstructed glomerular segmentation generated by this pipeline is shown (Fig. 11). Finally, the β-Tubulin signal intensity was quantified separately within the nestin-positive (cytoplasmic) and p57-positive (nuclear) compartments, and the nuclear to cytoplasmic intensity ratio (N/C ratio) was calculated. As expected, the β-Tubulin N/C ratio was below 1, indicating predominant cytoplasmic localization of β-Tubulin. The utility of this pipeline for further N/C ratio analyses was therefore demonstrated. It was subsequently applied to the mouse tissues described in this chapter and was also used to analyze N/C ratios in rat tissues following the intervention study described below (see Chapter 3.2).

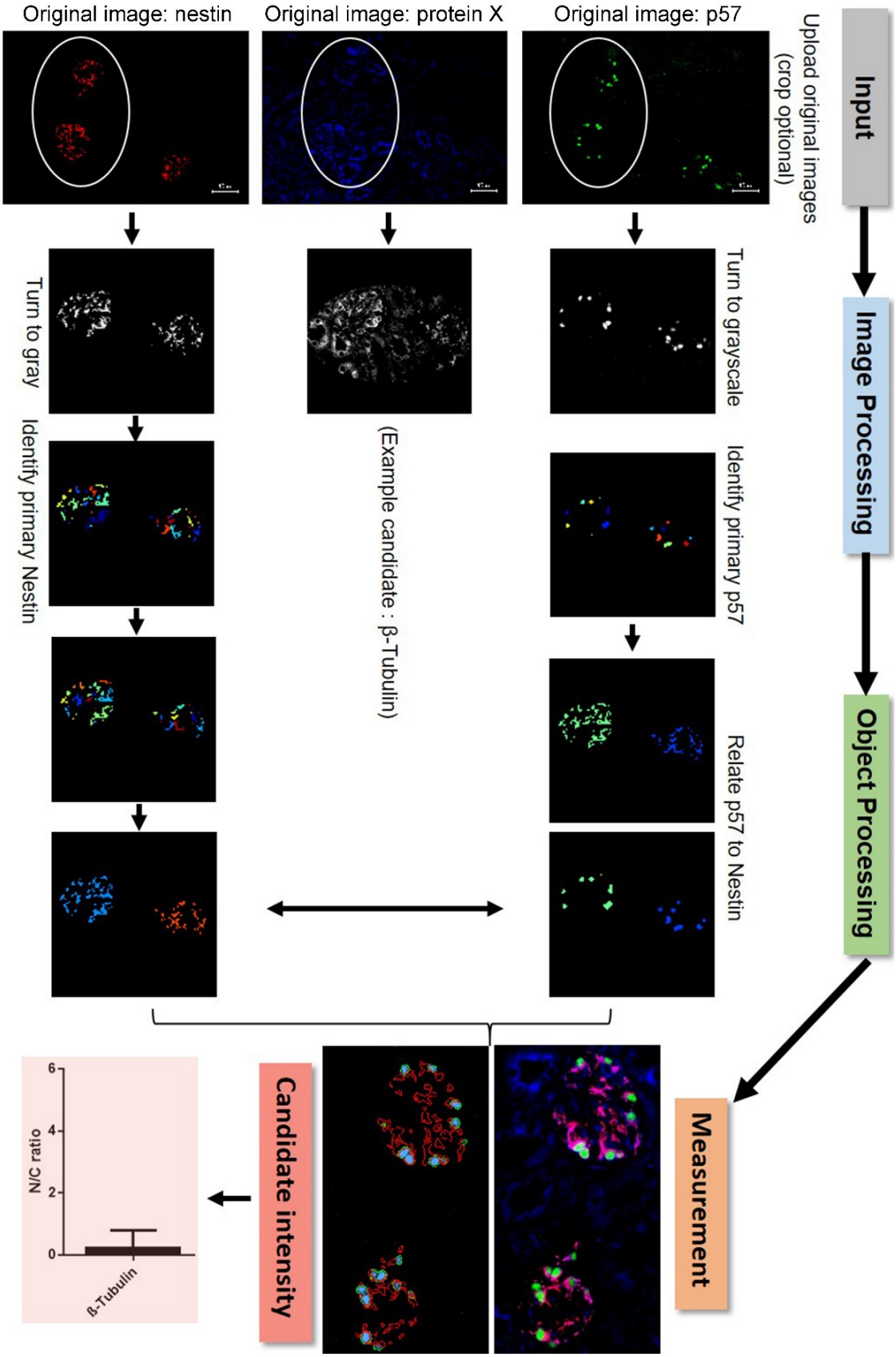


Figure 11. A workflow was established in CellProfiler to enable compartment-specific quantification of protein intensity in podocytes in triple-labeled kidney sections. Input: Original immunofluorescence images of nestin (cytoplasmic marker, red), the protein of interest (example: β-tubulin, blue), and p57 (nuclear marker, green) were uploaded. Image processing: Each channel was converted to grayscale, and primary objects corresponding to nestin and p57 signals were identified. Object

processing: A tertiary nestin mask was generated by subtracting p57-positive areas from the nestin-positive cytoplasmic regions to avoid overlap due to the 3D structure of podocytes. Nestin- and p57-positive objects from the same glomerulus were then paired. Measurement: The signal intensity of the candidate protein was measured separately within the nestin (cytoplasmic) and p57 (nuclear) compartments, and the N/C intensity ratio was calculated. The β-tubulin example demonstrates the analytical workflow and validation of the pipeline, showing predominant cytoplasmic localization (N/C ratio < 1).

4.1.2.2 Analysis of Nuclear to Cytoplasmic Intensity Ratio (N/C) of Known Candidate Proteins

The cellular localization of the protein SMCR8 (Smith-Magenis syndrome chromosome region, candidate 8) has been reported to include the nucleus, the cytosol, and lysosmes [118]. As a component of the C9orf72-SMCR8-WDR41 complex, SMCR8 plays an important role in autophagy regulation, vesicle trafficking, and immune response in transgenic mice [119]. Importantly, the subcellular distribution of this complex has been shown to change in response to amino acid starvation [120]. Representative immunofluorescence images of kidney sections from 11-, 35-, and 80-week-old mice stained for SMCR8, nestin, and p57 now revealed distinct age-dependent changes in SMCR8 localization within podocytes (Fig. 12A). At 11 weeks, SMCR8 fluorescence was predominantly cytoplasmic, showing a diffuse distribution within nestin-positive podocyte processes (see also yellow stained glomerular areas in the right merge column at 11 weeks). By 35 weeks, SMCR8 displayed a roughly equal distribution between cytoplasm and nucleus. In 80-week-old samples, SMCR8 exhibited pronounced nuclear accumulation accompanied by a marked reduction in cytoplasmic staining intensity. Quantitative analysis using the established imaging analysis workflow (see 3.1.2.1 above) revealed that the SMCR8 nuclear-to-cytoplasmic (N/C) fluorescence intensity ratio increased progressively from 0.79 ± 0.31 at 11 weeks to 1.06 ± 0.46 at 35 weeks and further to 1.29 ± 0.55 at 80 weeks (Fig. 12B). These increases were statistically significant between all examined time points (Fig. 12B; 11 w vs. 35 w, $p < 0.01$; 35 w vs. 80 w, $p < 0.05$; and 11 w vs. 80 w, $p < 0.0001$), thereby reflecting a progressive translocation of SMCR8 from the cytoplasm to the nucleus during podocyte aging.

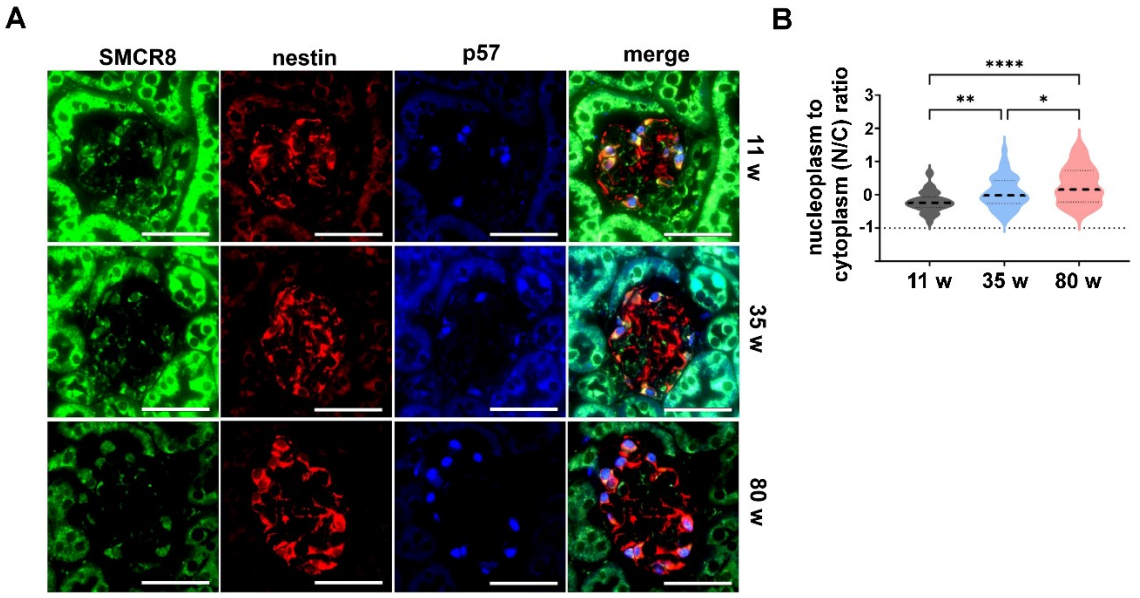


Figure 12. SMCR8 exhibits progressive nuclear translocation in podocytes during aging. (A) Representative images of podocytes showing SMCR8 (green signal) staining, with nestin (red signal) and p57 (blue signal) as cytoplasmic and nuclear markers, respectively. **(B)** Quantification of the nuclear-to-cytoplasmic ratio of SMCR8 staining intensity based on data from (A), measured in 29-46 glomeruli per age group. Data are presented as median (thick line) with interquartile range (thin lines). *P < 0.05, **P < 0.01, ****P < 0.0001. Scale bar: 40 µm.

Ran is a small Ras-related GTPase that regulates nucleocytoplasmic transport by maintaining a nuclear-to-cytoplasmic Ran-GTP/GDP gradient [121, 122]. Disruption of nuclear envelope integrity during aging or cellular stress has been reported to cause cytoplasmic mislocalization of Ran [74, 123]. In podocytes, a predominant cytoplasmic localization of Ran was evident at 11 weeks (Figs. 13A, B). With aging, Ran fluorescence progressively intensified in the nucleus, while remaining stronger in the cytoplasm (Figs. 13A, B). Quantitative analysis of the nuclear-to-cytoplasmic (N/C) intensity ratio confirmed a significant increase from 0.48 ± 0.32 at 11 weeks to 0.64 ± 0.33 at 35 weeks ($p < 0.05$), followed by a slight, non-significant decline to 0.61 ± 0.27 at 80 weeks (Fig. 13B). Notably, the N/C ratio remained below 1 at all ages, indicating that Ran localization retained a cytoplasmic predominance throughout podocyte aging.

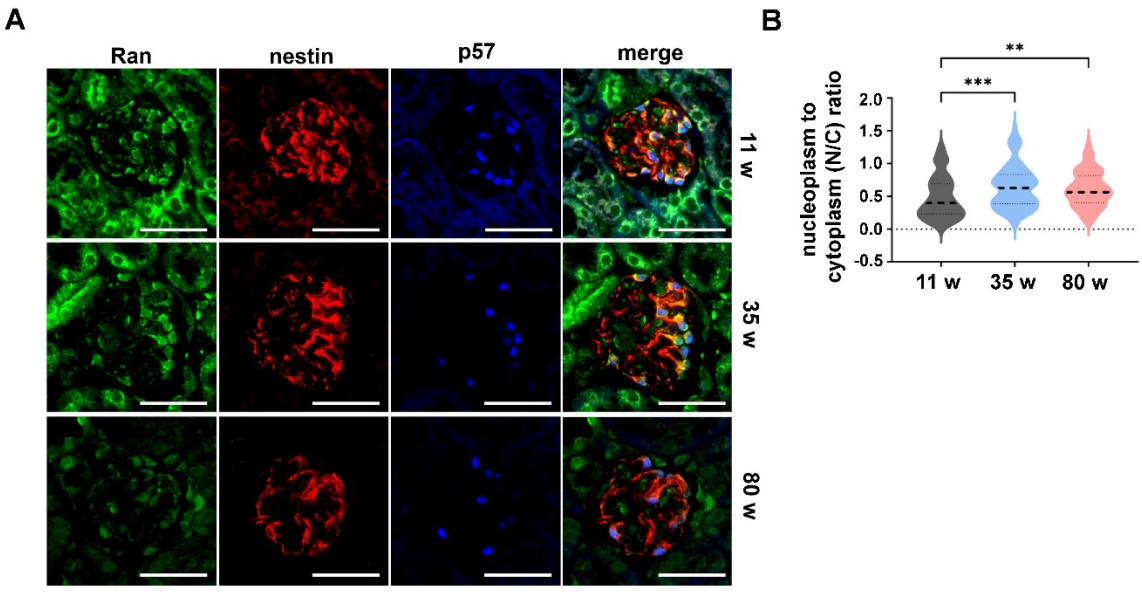


Figure 13. Ran shows age-dependent redistribution toward the nucleus while maintaining a predominant cytoplasmic localization in podocytes. (A) Representative images of podocytes showing Ran (green signal) staining, with nestin (red signal) and p57 (blue signal) as cytoplasmic and nuclear markers, respectively. **(B)** Quantification of the nuclear-to-cytoplasmic ratio of Ran staining intensity based on data from (A), measured in 56-79 glomeruli per age group. Data are presented as median (thick line) with interquartile range (thin lines). **P < 0.01, ***P < 0.001. Scale bar: 40 µm.

Eukaryotic initiation factor 4E (eIF4E) is a key translation initiation factor that resides in both the cytoplasm and the nucleus. It has been reported to translocate from the cytoplasm to the nucleus in response to nutrient deprivation or stress [124]. Consistent with previous findings, eIF4E displayed dual cytoplasmic and nuclear localization in podocytes, with the cytoplasm serving as the predominant compartment (Fig. 14). Quantitative analysis showed that the mean N/C intensity ratio of eIF4E remained below 0.4 (11 weeks: 0.33 ± 0.17; 35 weeks: 0.37 ± 0.22; 80 weeks: 0.38 ± 0.20, Fig. 14B). Across all three time points no significant differences were observed, indicating sustained cytoplasmic enrichment.

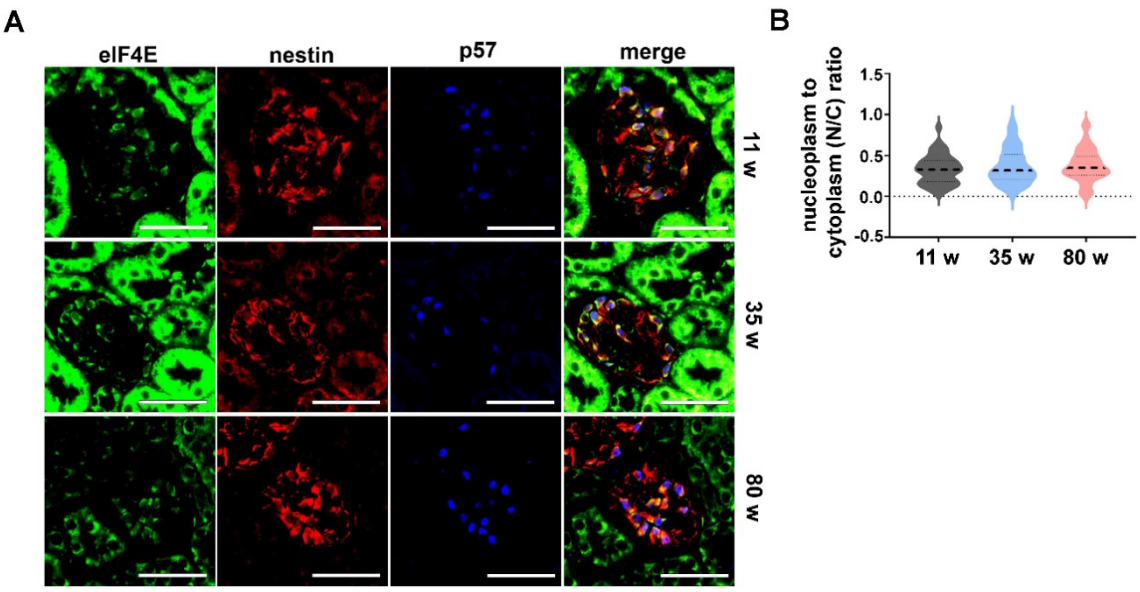


Figure 14. eIF4E maintains a stable cytoplasmic-predominant localization in podocytes during aging. (A) Representative images of podocytes showing eIF4E (green signal) staining, with nestin (red signal) and p57 (blue signal) as cytoplasmic and nuclear markers, respectively. **(B)** Quantification of the nuclear-to-cytoplasmic ratio of eIF4E staining intensity based on data from (A), measured in 44-96 glomeruli per age group. Data are presented as median (thick line) with interquartile range (thin lines). Scale bar: 40 µm.

DRG2 (Developmentally Regulated GTP-binding Protein 2), a protein implicated in the regulation of cell growth and differentiation [125], has been reported to alter its subcellular localization in response to specific stimuli, such as transferrin treatment following serum starvation [126]. In podocytes, DRG2 displayed a slightly cytoplasmic-dominant distribution at 11 weeks (N/C = 0.87 ± 0.42; Fig. 15). At 35 weeks, DRG2 localization shifted significantly toward the cytoplasm (N/C = 0.67 ± 0.28), indicating reduced nuclear relative intensity compared with 11 weeks. By 80 weeks the distribution returned to near equilibrium with a slight nuclear predominance. Quantitative analysis confirmed a significant increase from 35 to 80 weeks (0.67 ± 0.28 to 1.02 ± 0.38; $p < 0.0001$, Fig. 15B). Together, these data indicate a transient decrease in nuclear intensity at mid-age followed by recovery to near- or slight nuclear predominance at advanced age.

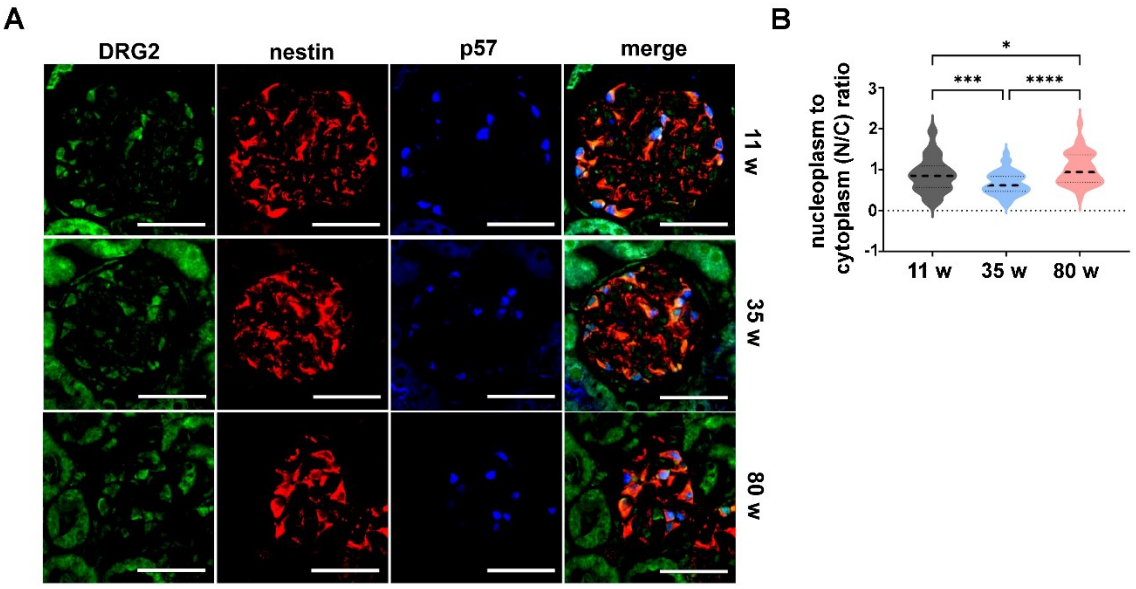


Figure 15. DRG2 exhibits transient nuclear enrichment during mid-age followed by partial cytoplasmic redistribution in aged podocytes. (A) Representative images of podocytes showing DRG2 (green signal) staining, with nestin (red signal) and p57 (blue signal) as cytoplasmic and nuclear markers, respectively. **(B)** Quantification of the nuclear-to-cytoplasmic ratio of DRG2 staining intensity based on data from (A), measured in 41-90 glomeruli per age group. Data are presented as median (thick line) with interquartile range (thin lines). *P < 0.05, ***P < 0.001, ****P < 0.0001. Scale bar: 40 µm.

The observed localization changes of these known proteins in podocytes during aging suggest a potential accumulation of defective nuclear pore complexes (NPCs) in aged cells. These findings highlight the possibility that age-related alterations in nucleocytoplasmic transport may contribute to podocyte dysfunction, warranting further investigation into podocyte-specific regulatory mechanisms.

4.1.2.3 Screening for Podocyte-Specific Mislocalized Proteins During Aging

4.1.2.3.1 Optimization of the Podocyte Isolation Protocol

Labeling of Podocytes

Kidneys were collected from mice that received doxycycline (Dox) either by a single intraperitoneal (i.p.) injection 24 hours before organ collection or via drinking water for 14 days. A small piece of kidney tissue was homogenized in PBS, and the resulting suspension was used to compare transgene induction efficiency. The intensity of the eGFP signal was examined by fluorescence microscopy. As shown in Figures 16A and B, under identical exposure conditions (exposure time: 1/23 second), a substantial number of eGFP-positive cells were observed in glomeruli from the mouse treated with Dox in drinking water, whereas no eGFP signal was detected in glomeruli from the i.p.-injected mouse. However,

upon longer exposure (exposure time: 1/6 second), eGFP-positive podocytes became visible in glomeruli from the i.p.-injected mouse. These results indicate that a single i.p. injection of Dox was sufficient to induce transgene expression, although with markedly lower efficiency. Therefore, for subsequent podocyte isolation experiments, Dox was administered via drinking water for 14 days to ensure more robust and consistent induction.

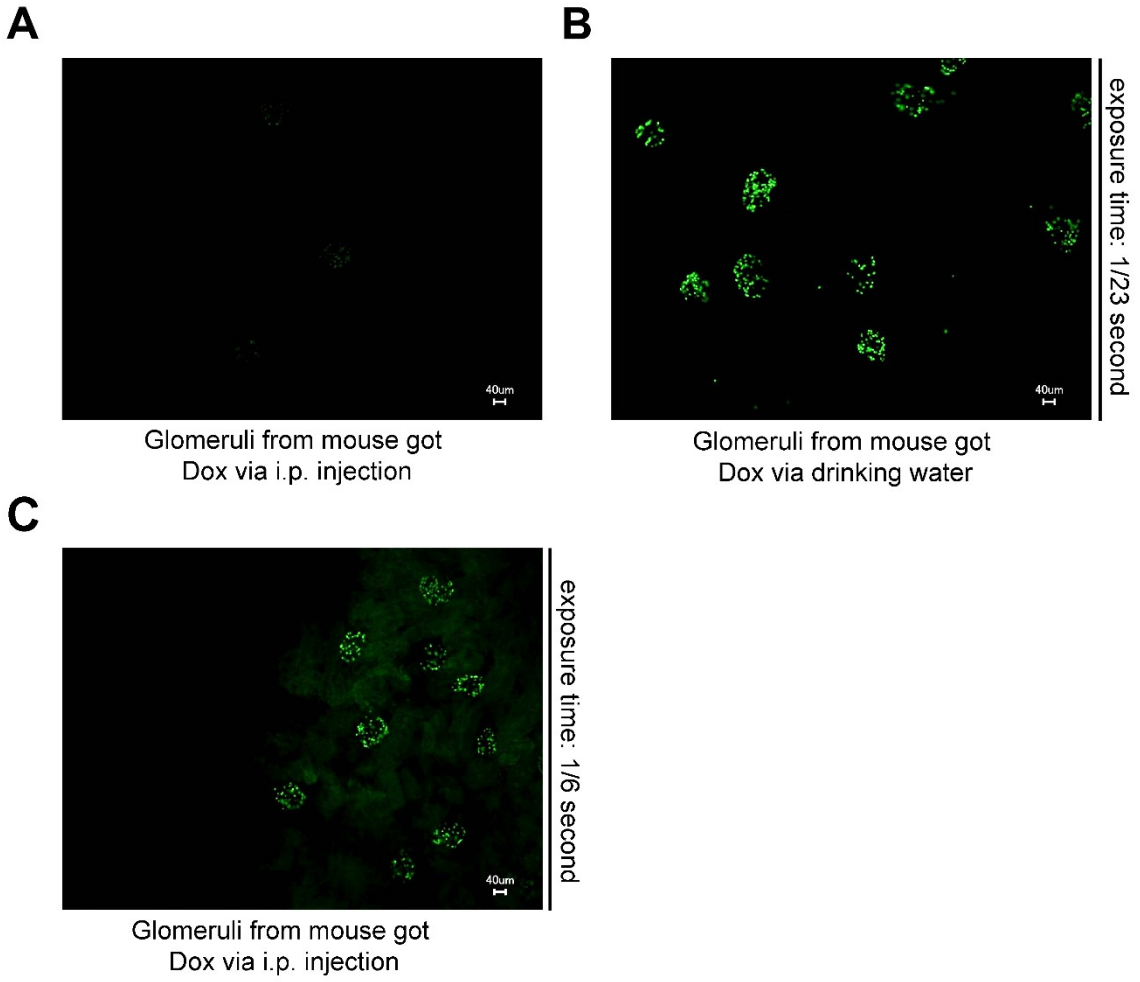


Figure 16. Doxycycline administration *via* drinking water induces stronger transgene expression in podocytes than intraperitoneal injection. Kidney pieces from Pod-rtTA mice were homogenized in PBS. Panels A-C show kidney suspensions under fluorescence microscopy. **(A)** Glomeruli from the mouse that received a single i.p. injection of Dox. **(B)** Glomeruli from the mouse that received Dox via drinking water for 14 days. Panels A and B illustrate the labeling efficiency under identical exposure conditions, with an exposure time of 1/23 second. **(C)** Longer exposure (1/6 second) revealed eGFP-positive podocytes in glomeruli from the i.p.-injected mouse, indicating lower but detectable transgene induction. Scale bar: 40 µm.

Primary Podocyte Isolation

After establishing the optimal Dox induction conditions, further optimization steps were undertaken to improve the yield of isolated podocytes. As summarized in Table 8, these optimizations mainly focused on two aspects: (i) the choice of

perfusion solution and (ii) the washing strategy for the 40 µm filter during glomerular isolation when mice were perfused with NaCl. Because podocyte yield tends to decline with age, the optimization experiments were primarily conducted using 35- and 80-week-old mice.

When mice were perfused with 0.9% iron oxide (Fe_3O_4, 50 nm) suspended in 0.9% NaCl [127], glomeruli were isolated using a magnetic cell separation approach instead of the sieving method. This method efficiently removed most tubular fragments after several washing steps. However, incomplete and inconsistent perfusion of glomeruli with Fe_3O_4 particles was frequently observed, likely due to sedimentation of the suspension during the perfusion process, which consequently reduced isolation efficiency. To overcome this limitation, physiological saline (0.9% NaCl) was evaluated as an alternative perfusion solution. In this approach, glomeruli were isolated from the tubular fraction using a 40 µm filter, taking advantage of the size difference between glomeruli and renal tubules [110]. When comparing the two perfusion methods, a substantially higher number of $eGFP^+$ podocytes was obtained from a 36-week-old mouse perfused with NaCl compared to one perfused with Fe_3O_4 (Exp. No. 2 vs. Exp. No. 3). In contrast, both approaches yielded comparable podocyte numbers in 80-week-old mice (Exp. No. 3 vs. Exp. No. 4). Overall, perfusion with 0.9% NaCl proved to be more consistent, technically robust, and reproducible than perfusion with Fe_3O_4 particles suspended in saline. During glomerular isolation using NaCl perfusion, substantial glomerular attachment to the 40 µm filter was observed when washing was performed with a 1 ml pipette tip system, even after multiple washing steps. To address this issue, a syringe-needle system was introduced to improve washing efficiency and maximize glomerular recovery. This modification markedly increased the yield of isolated glomeruli, resulting in an average of ~360,000 podocytes sorted from 11-week-old mice (Exp. No. 5). The yield decreased to approximately 270,000 in 35-week-old mice (Exp. No. 6) and further declined to 120,000 in 80-week-old mice (Exp. No. 7). Taken together, the refined isolation protocol-based on NaCl perfusion combined with syringe-assisted filter washing-proved to be technically straightforward, cost-effective, and reliable, while maintaining satisfactory podocyte yields across different age groups.

Table 8: Optimization of podocyte isolation and eGFP$^+$ cell yield under different experimental conditions

Exp. no.	Perfusion solution	Washing method	Age (weeks)	eGFP$^+$ cells (n)
1	0.9% Fe_3O_4 in 0.9% NaCl	—	36	~89,000
2	0.9% NaCl	With pipette	36	~262,000
3	0.9% Fe_3O_4 in 0.9% NaCl	—	80	~90,000
4	0.9% NaCl	With pipette	80	~90,000
5	0.9% NaCl	With syringe	11	~360,000
6	0.9% NaCl	With syringe	35	~270,000
7	0.9% NaCl	With syringe	80	~120,000

4.1.2.3.2 Validation of Nuclear and Cytoplasmic Fractionation from Podocytes of Different Ages

Following the isolation of mouse podocytes, nuclear and cytoplasmic protein fractions were extracted from mice of different age groups, and their concentrations were subsequently quantified. For each experimental condition, equal amounts of cytoplasmic or nuclear protein in the same volume were used for Western blot analysis to assess the purity of the protein samples. Membranes were incubated with the nuclear marker Histone-H3 and the cytoplasmic markers β-actin or Vinculin. In all samples, Histone-H3 bands were detected exclusively in the nuclear fractions, whereas cytoplasmic markers such as β-actin or Vinculin were detected only in the cytoplasmic fractions. These results indicate that cross-contamination between nuclear and cytoplasmic fractions was negligible, and the purity was sufficient for mass spectrometry analysis. Following the same fractionation protocol, three replicates of each fraction were prepared from 11-week-old and 35-week-old mice. However, due to the reduced podocyte yield in 80-week-old mice, only two replicates per fraction could be obtained.

Following the isolation of mouse podocytes, nuclear and cytoplasmic protein fractions were extracted from mice of different age groups, and their concentrations were subsequently quantified. For each experimental condition, equal amounts of nuclear or cytoplasmic proteins with identical sample volumes were subjected to Western blot analysis to evaluate the purity of the fractions. Membranes were probed with the nuclear marker Histone H3 and the cytoplasmic markers β-actin or Vinculin. As expected, Histone H3 signals were exclusively detected in the nuclear fractions, whereas β-actin and Vinculin were detected only in the cytoplasmic fractions. These results confirm that cross-contamination between nuclear and cytoplasmic fractions was negligible and that the fraction purity was sufficient for subsequent mass spectrometry analysis. Using the same fractionation protocol, three biological replicates of each fraction were prepared from 11-week-old and 35-week-old mice. However, due to the reduced podocyte yield in 80-week-old mice, only two replicates per fraction could be obtained.

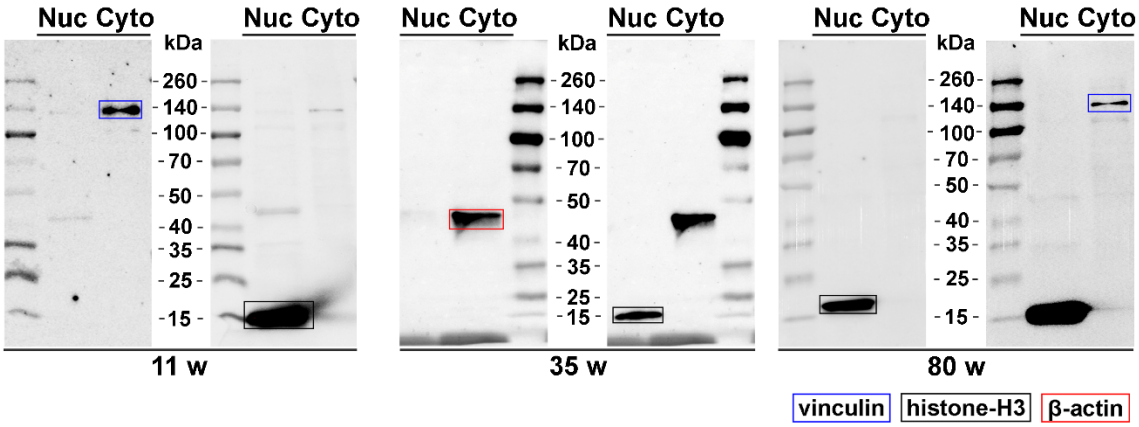


Figure 17. Nuclear and cytoplasmic protein fractions from isolated podocytes show high purity. The purity of nuclear and cytoplasmic protein fractions was assessed by Western Blot using typical markers: Histone-H3 for nuclear proteins and β-actin or Vinculin for cytoplasmic proteins. Nuc, nuclear protein fration; Cyto, cytoplasmic protein fraction.

4.1.2.3.3 Mass Spectrometry Data

Mass spectrometry analysis was performed with the cytoplasmic and nuclear protein franctions prepared above, to screen for podocyte specific marker proteins which show age-related subcellular change. For each identified protein, the N/C intensity ratio was calculated to assess its relative subcellular localization.

Statistical comparisons between age groups were performed using the limma linear model framework, and the results were visualized as volcano plots. As shown in figure 18A, volcano plot analysis revealed extensive relocalization between 80 and 11 weeks, whereas comparisons involving the intermediate 35-

week group showed no significant changes (threshold (False discovery rate (fdr) <= 0.2 & |log2(fold−change)| >= 0.58 (fold−change >= 1.5)), indicating that major spatial proteome remodeling occurs primarily in late aging. Examination of the complete sets of significantly shifting proteins (Supplementary Table 1) revealed clear functional patterns underlying the age-dependent spatial proteome remodeling. Proteins that became more nuclear with age were dominated by components of the mitochondrial respiratory chain and oxidative phosphorylation machinery, including multiple subunits of complexes I, III, IV, and V (e.g., Atp5if1, Cox5b, Rmnd1, Ndufb8, Chchd3), as well as cytoplasm-to-nucleus shifters such as Ndufa2 and Cox7c [128, 129, 130, 131]. Additional nuclear-shifting proteins included regulators of mitochondrial dynamics, import, and redox homeostasis (Mff, Tomm40, Tomm70, Vdac1-3, Micu1), indicating a coordinated nuclear enrichment of mitochondrial and redox-associated pathways [132, 133, 134, 135, 136, 137]. In contrast, proteins that became more cytoplasmic with age consisted largely of metabolic turnover enzymes involved in glycolysis, amino-acid metabolism, and small-molecule catabolism (Dbi, Ldha, Pkm, Aldoa, Aldoc, Aldh7a1) [138, 139, 140, 141, 142] , as well as stress-response and cytoskeletal regulators (Serpinb6, Cap1, Cfl1, Anxa3/5/6) [143, 144, 145, 146, 147, 148]. Prominent nucleus-to-cytoplasm transitions such as Lgals1 and Alad further highlighted an age-related cytoplasmic redistribution of metabolic and structural factors [149, 150, 151].

To explore the biological implications of these spatial proteome changes, Gene Ontology (GO) enrichment analyses were performed on proteins showing significant increases or decreases in N/C ratio (Figs. 18B-D).

GO Biological Process analysis revealed that proteins shifting toward the cytoplasm were enriched for small-molecule catabolism, amino-acid metabolism, and cofactor/vitamin-related processes, indicating that metabolic turnover enzymes and cytoplasmic metabolic pathways become increasingly dominant in aged podocytes. In contrast, proteins shifting toward the nucleus were broadly enriched for mitochondrial and oxidative phosphorylation (OXPHOS) pathways, including electron transport chain activity, cellular respiration, and ATP synthesis-coupled electron transport. These enrichments were driven by multiple OXPHOS complex components distributed across the full significance set, indicating a

coordinated age-related redistribution of mitochondrial and redox-related machinery toward the nuclear fraction.

GO Cellular Component terms further highlighted this compartmental reorganization. Proteins exhibiting cytoplasmic shifts were enriched for perinuclear endoplasmic reticulum, cytoskeletal and membrane-associated regions, and extracellular matrix components, reflecting an age-dependent redistribution toward cytoplasmic structural compartments. Conversely, nuclear-enriched proteins mapped predominantly to mitochondrial protein-containing complexes, inner mitochondrial membrane assemblies, and the respirasome, indicating an age-associated nuclear enrichment of mitochondrial and respiratory chain components.

Molecular Function analysis showed that proteins becoming more cytoplasmic were enriched for transaminase activity, lyase/carbon–carbon lyase activity, and ion/cofactor-binding functions (e.g., NAD binding, magnesium/alkali-metal ion binding, calcium-dependent phospholipid binding), as well as GDP-dissociation inhibitor activity and wide-pore channel activity. In contrast, proteins gaining nuclear localization were enriched for oxidoreductase and electron-transfer functions, including NADH dehydrogenase (ubiquinone/quinone) activity, oxidoreductase activity acting on NAD(P)H, quinone or similar compounds as acceptor, electron transfer activity, and (oxidoreduction-driven) transmembrane transporter activity, together with voltage-gated anion channel activity.

A

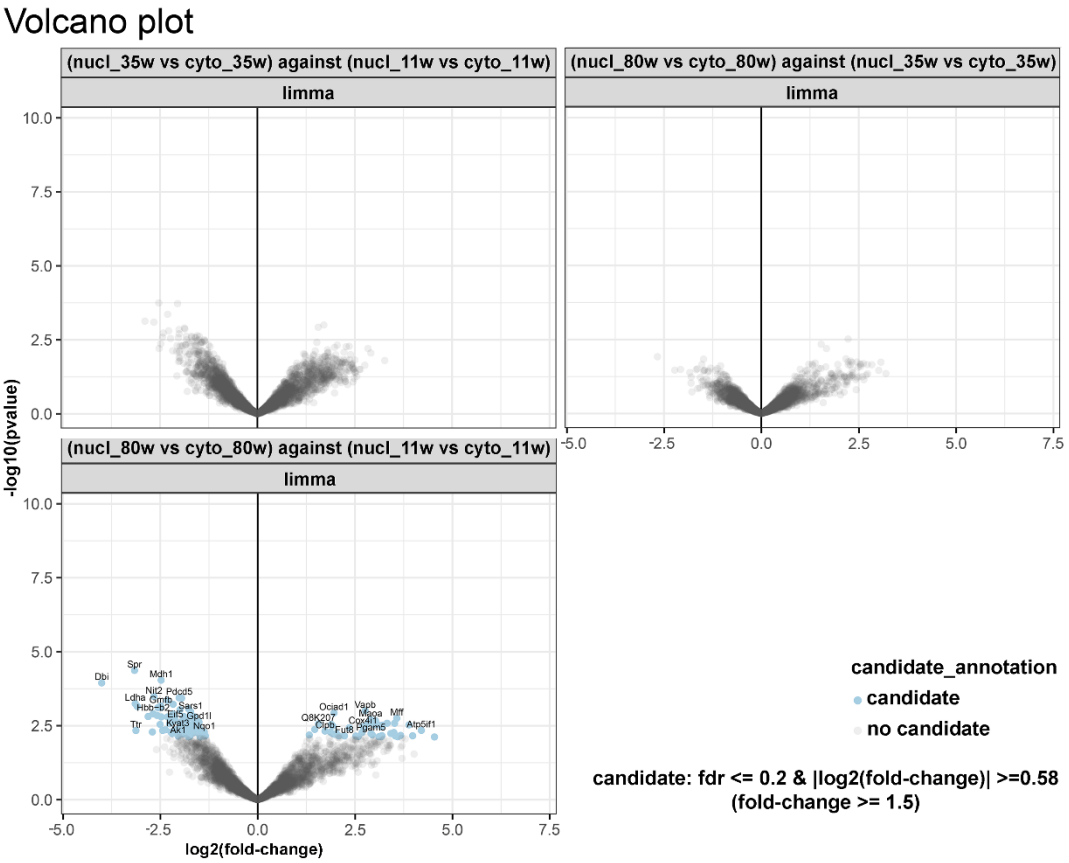
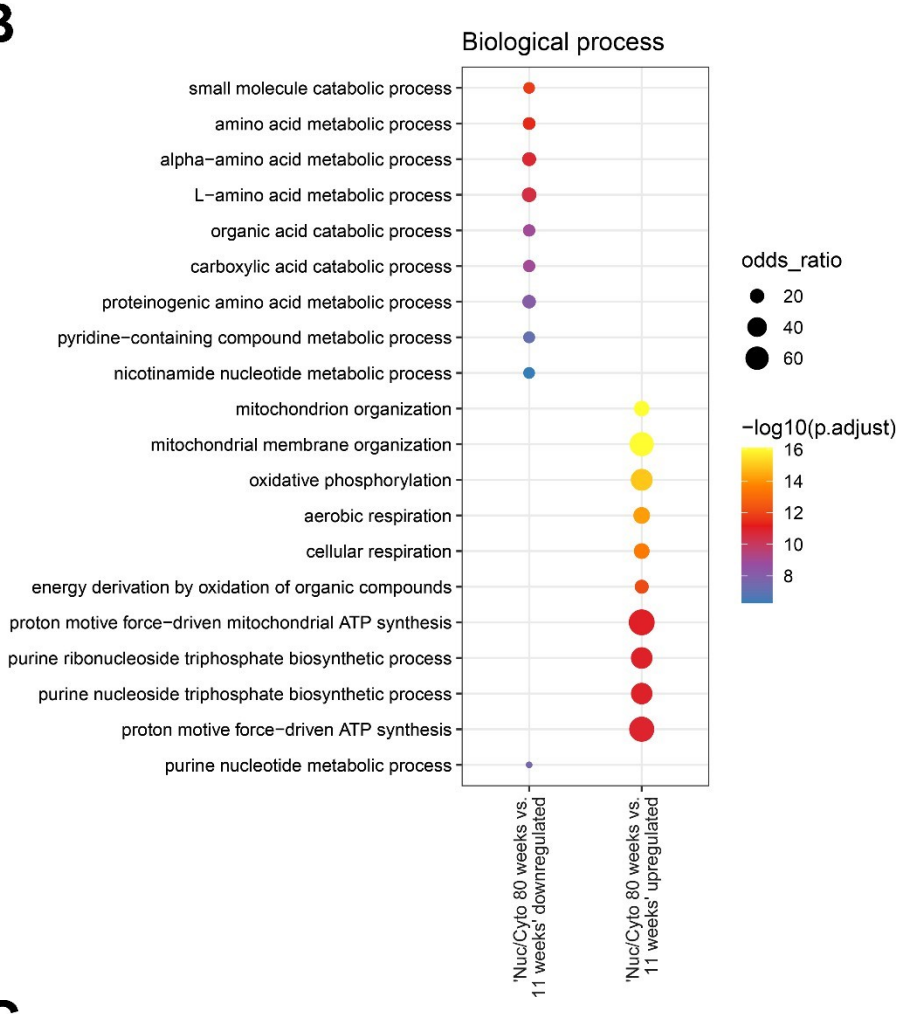
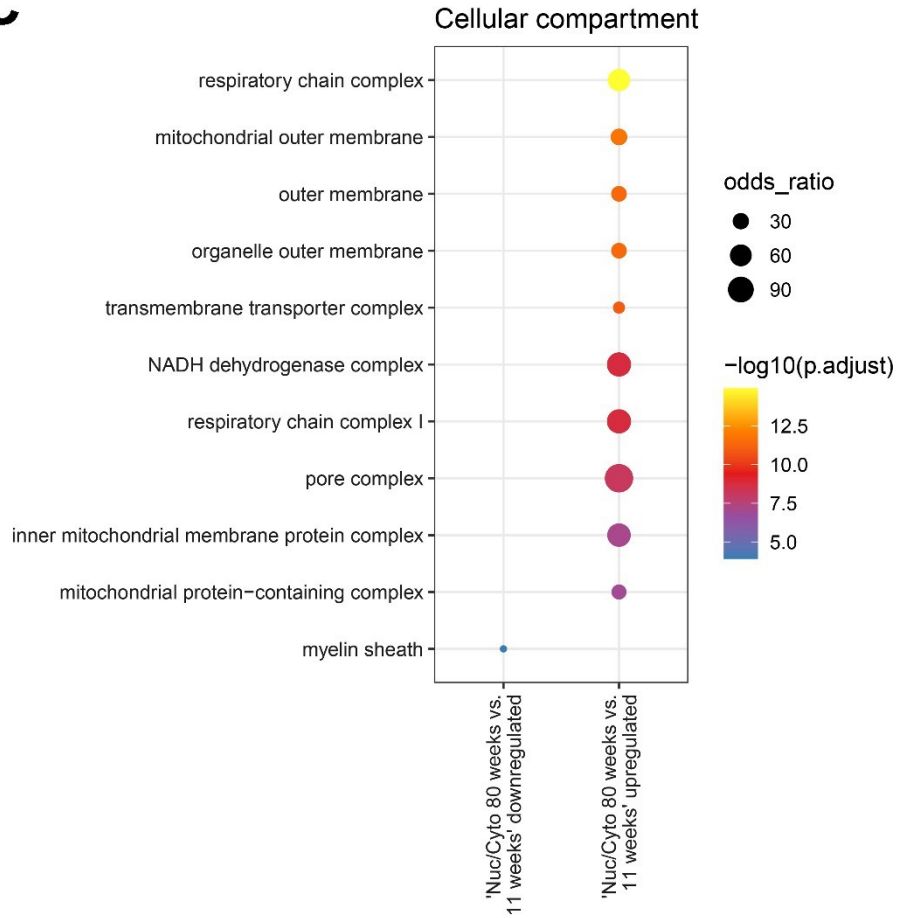


Figure 18A. Volcano plot of differential nuclear-to-cytoplasmic (N/C) ratios between 80- and 11-week-old podocytes. Volcano plot showing age-dependent changes in protein nuclear-to-cytoplasmic (N/C) ratios, analyzed using the limma linear model. Each point represents a quantified protein. Proteins with significantly increased N/C ratios (more nuclear with age) are shown on the right, and proteins with significantly decreased N/C ratios (more cytoplasmic with age) on the left. Significance thresholds were set at FDR ≤ 0.2 and $|\log_2(\text{fold change})| \geq 0.58$ (corresponding to ≥1.5-fold change). No significant changes were detected in comparisons involving 35-week-old mice (top panels). Representative proteins exhibiting the strongest shifts between 80- and 11-week-group are highlighted as candidates (lower panel).

B


Biological process
small molecule catabolic process
amino acid metabolic process
alpha−amino acid metabolic process
L−amino acid metabolic process
organic acid catabolic process
carboxylic acid catabolic process
proteinogenic amino acid metabolic process
pyridine−containing compound metabolic process
nicotinamide nucleotide metabolic process
mitochondrion organization
mitochondrial membrane organization
oxidative phosphorylation
aerobic respiration
cellular respiration
energy derivation by oxidation of organic compounds
proton motive force−driven mitochondrial ATP synthesis
purine ribonucleoside triphosphate biosynthetic process
purine nucleoside triphosphate biosynthetic process
proton motive force−driven ATP synthesis
purine nucleotide metabolic process
'Nuc/Cyto 80 weeks vs. 11 weeks' downregulated
'Nuc/Cyto 80 weeks vs. 11 weeks' upregulated
odds_ratio
20
40
60
−log10(p.adjust)
16
14
12
10
8

C


Cellular compartment
respiratory chain complex
mitochondrial outer membrane
outer membrane
organelle outer membrane
transmembrane transporter complex
NADH dehydrogenase complex
respiratory chain complex I
pore complex
inner mitochondrial membrane protein complex
mitochondrial protein−containing complex
myelin sheath
'Nuc/Cyto 80 weeks vs. 11 weeks' downregulated
'Nuc/Cyto 80 weeks vs. 11 weeks' upregulated
odds_ratio
30
60
90
−log10(p.adjust)
12.5
10.0
7.5
5.0

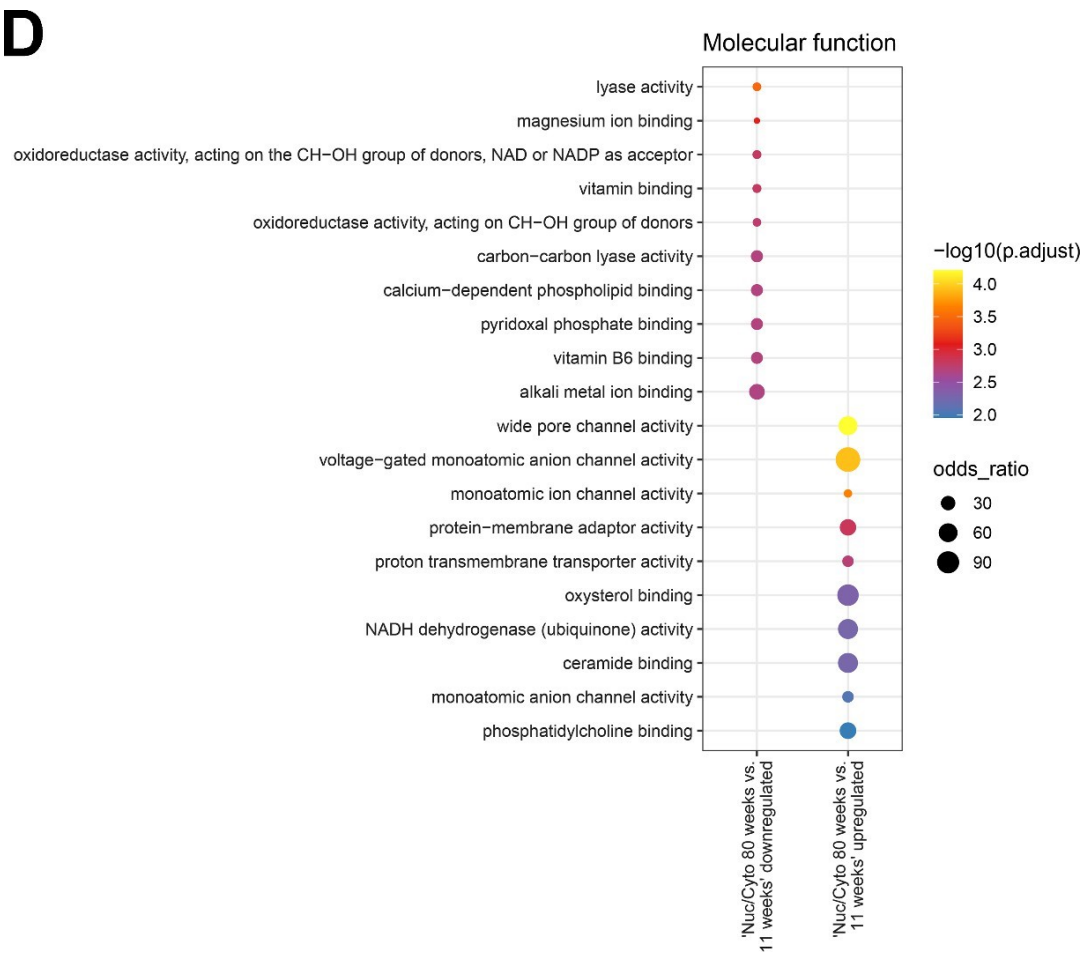


Figure 18 B-D. Gene Ontology enrichment analyses of proteins showing age-dependent shifts in nuclear-to-cytoplasmic (N/C) ratios. GO enrichment was performed separately for proteins with significantly increased (more nuclear) or decreased (more cytoplasmic) N/C ratios between 80- and 11-week-old podocytes. **(B)** Biological Process terms show that nuclear-shifting proteins were enriched for mitochondrial and oxidative phosphorylation pathways, whereas cytoplasmic-shifting proteins were enriched for metabolic and catabolic processes. **(C)** Cellular Component terms indicate that nuclear-enriched proteins were associated with mitochondrial complexes, while cytoplasmic-enriched proteins localized to perinuclear ER, cytoskeletal, and membrane-related structures. **(D)** Molecular Function analysis revealed enrichment of oxidoreductase and electron-transfer activities among nuclear-shifting proteins, and transaminase, cofactor-binding, and structural-regulatory functions among cytoplasmic-shifting proteins. Together, these results demonstrate coordinated age-related reorganization of mitochondrial, metabolic, and structural pathways across subcellular compartments.

In summary, aging is accompanied by a progressive loss of podocytes, initiating focal segmental glomerulosclerosis (FSGS) and contributing to a gradual decline in kidney function. The findings presented in this chapter suggest that dysfunctional nucleocytoplasmic compartmentalization (NPC) plays a key role in these processes. Several proteins known to undergo age-related shifts in subcellular localization in other postmitotic cells, such as neurons, exhibited comparable alterations in aged mouse podocytes. Among these, SMCR8 showed a marked increase in its nuclear-to-cytoplasmic (N/C) ratio, while Ran and DRG2

displayed distinct yet dynamic redistribution patterns. Collectively, these changes reflect a progressive imbalance in nucleocytoplasmic distribution, consistent with impaired NPC function during aging. Complementary proteomic analyses further revealed a coordinated remodeling of the podocyte spatial proteome, characterized by nuclear accumulation of mitochondrial and redox-associated proteins and cytoplasmic displacement of metabolic and structural enzymes. This remodeling suggests that altered mitochondrial-nuclear communication and disrupted metabolic compartmentalization are hallmark features of podocyte aging. Although these molecular alterations may serve as potential indicators of NPC dysfunction and early FSGS development, their diagnostic and mechanistic significance requires further validation.

Together, these results support a model in which impaired NPC function acts as an early molecular driver of podocyte dysfunction and the onset of FSGS. Building upon this hypothesis, Chapter 3.2 investigates whether pharmacological modulation of nuclear transport can therapeutically counteract these defects. Specifically, the efficacy of the nuclear export inhibitor Selinexor (KPT-330) was evaluated in a spontaneous rat model of FSGS to assess its potential to restore podocyte homeostasis and slow disease progression.

4.2 Nuclear Export Inhibitor Selinexor (KPT-330) Improves Kidney Function in a Rat Model of Focal Segmental Glomerulosclerosis

4.2.1 Restoration of Impaired NPC Function by KPT-330 *In Vitro*

To explore the potential rescue of nuclear pore complex (NPC) dysfunction *in vitro*, a stable HeLa cell line expressing a fusion protein composed of tandem green fluorescent protein (GFP) linked to a nuclear localization signal (2xGFP-NLS) was established, serving as a marker for nuclear import. Under physiological conditions, the NLS directs the GFP protein into the nucleus, resulting in a high nuclear-to-cytoplasmic fluorescence ratio. NPC impairment was induced by siRNA-mediated downregulation of Nup93, an essential NPC component that is disrupted in certain FSGS-associated mutations [96]. Given the indispensable role of Nup93 in maintaining NPC integrity [152, 153, 154, 155], its expression was only partially reduced rather than completely abolished. Nup93 knockdown was confirmed by Western blot analysis (Figs. 19A, B), and this partial depletion compromised NPC activity, as evidenced by partial mislocalization of the 2xGFP-NLS reporter to the cytoplasm, reflecting a reduced capacity of the NPC to maintain nuclear-cytoplasmic compartmentalization (Figs. 19C, D).

As a positive control, cells were treated with 5% hexanediol, which perturbs the central diffusion barrier of the NPC formed by nucleoporins [156]. Following Nup93 depletion or hexanediol treatment, the nuclear-to-cytoplasmic ratio of 2xGFP-NLS decreased to 1.159 and 0.625, respectively, compared with 1.679 in control cells Fig. 19D). Subsequently, Nup93-deficient HeLa cells were exposed to 1 µM KPT-330 for two hours prior to imaging. KPT-330 treatment restored nuclear enrichment of 2xGFP-NLS to levels comparable with those observed in untreated wild-type cells (Figs. 19C, D). A similar effect was observed with 10 nM leptomycin B (LMB), another inhibitor of the nuclear export receptor XPO1, which also reinstated nuclear localization of the reporter to near wild-type levels. However, due to the known cytotoxicity of LMB [157, 158], subsequent experiments focused on KPT-330, which has been extensively evaluated in both preclinical and clinical studies [159, 160, 161, 162].

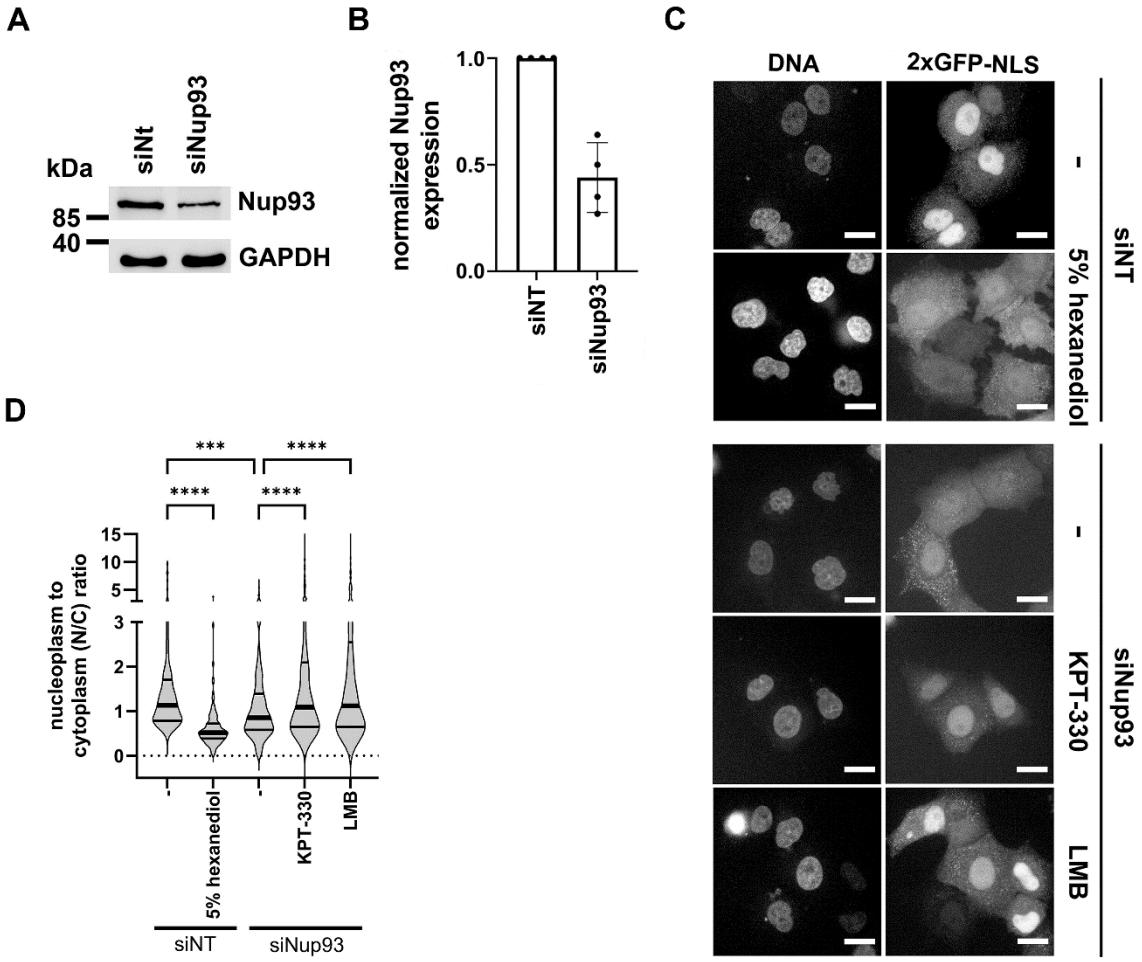


Figure 19. XPO1 inhibition alleviates nucleocytoplasmic transport defects following Nup93 depletion in HeLa cells expressing 2xGFP-NLS [163]. (A) Immunoblot analysis of HeLa cells transfected for 48 h with either 20 nM non-targeting siRNA (siNT) or Nup93-specific siRNA, with GAPDH serving as a loading control. **(B)** Densitometric quantification of Nup93 protein levels, normalized to GAPDH and further adjusted to the untreated control, based on four independent experiments. Each dot represents an individual measurement. **(C)** HeLa cells stably expressing 2xGFP-NLS were transfected as in panel (A) and, 48 h post-transfection, exposed to 1 µM KPT-330 or 10 nM Leptomycin B (LMB) for 2 h. As a positive control for NPC perturbation, siNT-transfected cells were treated with 5% hexanediol for 5 min. Nuclear DNA was visualized using sirDNA. **(D)** Quantification of the nuclear-to-cytoplasmic (N/C) fluorescence intensity ratio of 2xGFP-NLS under the conditions described in panel (C). Analysis was performed with a custom-built image processing pipeline. Data are presented as median (thick line) with interquartile range (thin lines). Between 70 and 150 cells were analyzed per treatment across three independent experiments. Statistical significance: ***P < 0.001, ****P < 0.0001. Scale bar, 20 µm.

4.2.2 Histological and Functional Characterization of MWF Rats During Aging

The successful evaluation of the XPO1 inhibitor KPT-330 in stabilizing NPC function *in vitro* (Fig. 19) prompted us to investigate its potential therapeutic benefit *in vivo* using the MWF rat model of FSGS, by targeting nuclear-to-cytoplasmic transport. To this end, we first characterized histological and

functional parameters of male MWF rats, which begin to develop hypertension and a slight decline in kidney function as early as 10 weeks of age. Histological evaluation of MWF rats was performed at 10 and 40 weeks of age. PAS staining revealed that by 40 weeks, the proportion of glomeruli exhibiting synechiae was nearly threefold higher than those of 10-week-old rats (10 w: 13.12 ± 9.89 % vs. 40 w: 34.54 ± 5.29 %; P < 0.001; Fig. 20), indicating that the housing conditions were appropriate for MWF rats to spontaneously develop FSGS.

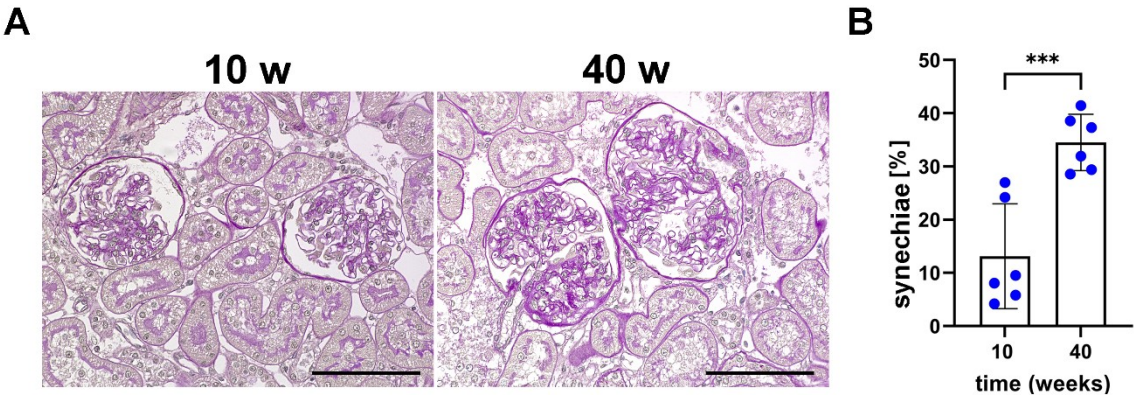


Figure 20. Increased glomerular synechiae in 40-week-old MWF rats [163]. (A) Representative PAS-stained kidney sections from 20- and 40-week-old untreated MWF rats. **(B)** Quantification of glomeruli exhibiting synechiae between the capillary tuft and Bowman's capsule, across entire tissue sections. n=6 per group. Data are shown as means ± SD. ***P < 0.001. Scale bar: 100 µm.

IHC staining for WT-1, CD44, and collagen IV revealed that the development of FSGS/Synechiae was accompanied by podocyte loss (Fig. 21A), activation of parietal epithelial cell (Fig. 21B), and extracellular matrix deposition (Fig. 21C). Collectively, these changes demonstrate the progression of FSGS in MWF rats during aging.

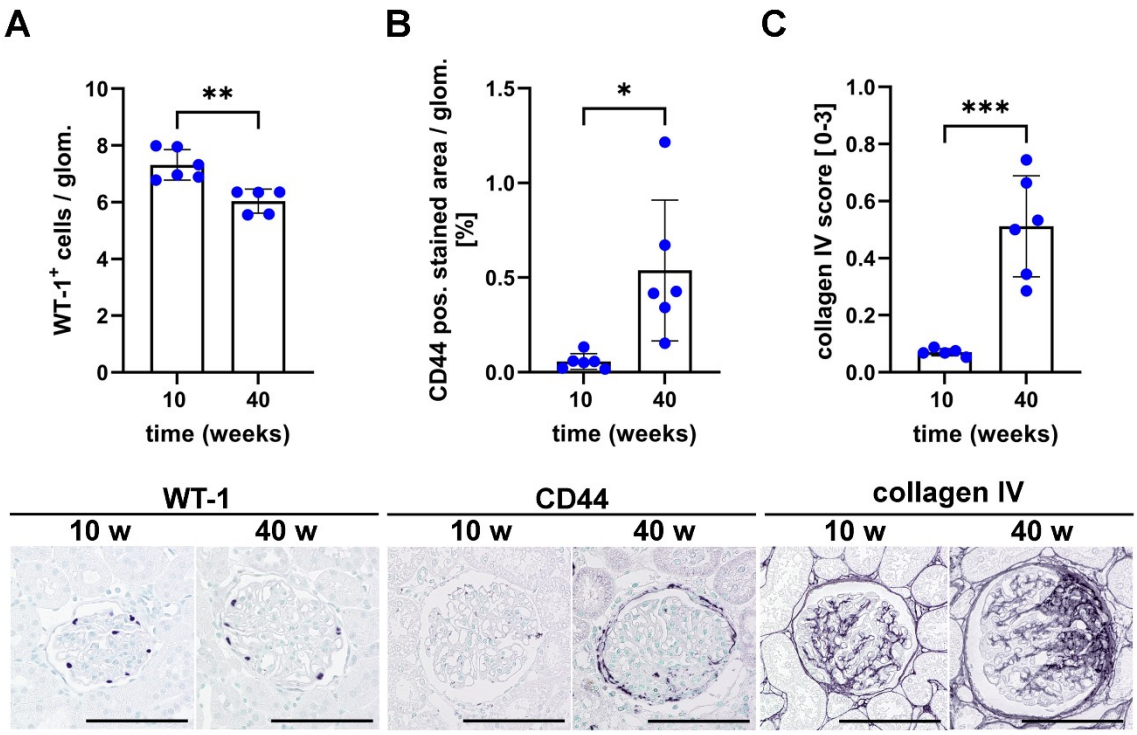


Figure 21. Development of FSGS in aged MWF is associated with podocyte loss, PEC activation, and glomerular matrix deposition [163]. (A) Quantification of WT-1-positive podocytes per glomerulus, with representative stainings shown on the right. **(B)** Percentage of CD44-positive area per glomerulus, with representative stainings on the right. **(C)** Percentage of collagen IV-positive area within the glomerular tuft, with representative stainings on the right. n=5-6 per group. Data are shown as means ± SD. *P < 0.05, **P < 0.01, ***P < 0.001. Scale bars: 100 µm.

The functional changes in MWF rats during aging were assessed. Serum creatinine (Fig. 22A) and blood urea nitrogen (BUN, Fig. 22B) levels were monitored every 5 weeks starting at week 5, whereas cystatin C (Fig. 22C) and albuminuria (Fig. 22D) were measured only at weeks 10, 20, and 40. Together, these parameters indicated an age-dependent decline in renal function in MWF rats, which had already begun by at least week 10, the second earliest time point examined in this study.

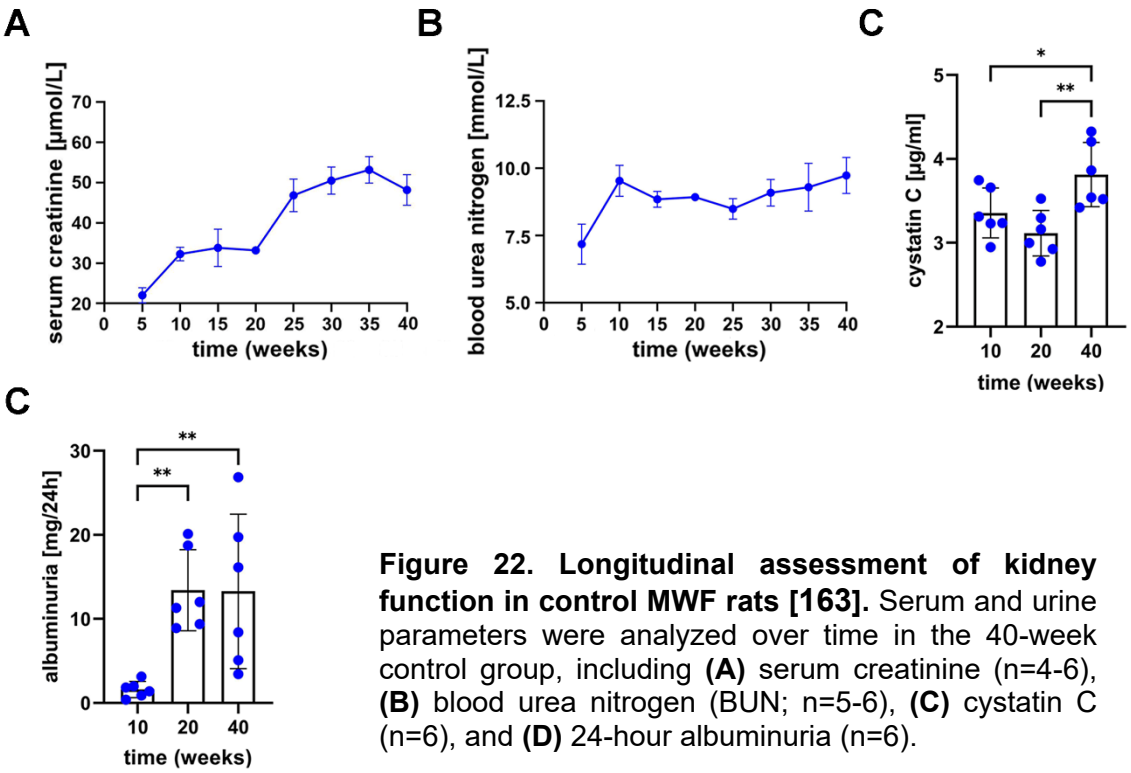


Figure 22. Longitudinal assessment of kidney function in control MWF rats [163]. Serum and urine parameters were analyzed over time in the 40-week control group, including **(A)** serum creatinine (n=4-6), **(B)** blood urea nitrogen (BUN; n=5-6), **(C)** cystatin C (n=6), and **(D)** 24-hour albuminuria (n=6).

4.2.3 KPT-330 Alters General Physiological Parameters in MWF Rats

Based on the results above, week 10 was selected as the starting point for subsequent intervention experiments, representing a stage at which kidney function had begun to decline while histological changes remained subtle. The effects of KPT-330 were investigated on MWF rats using two experimental approaches: (A) treatment from week 10 to 20, with animals euthanized at week 20 (20-week group) to assess the immediate impact of KPT-330, and (B) treatment from week 10 to 20 followed by a non-interventional observation period until euthanasia at week 40 (40-week group), a stage at which MWF rats typically display marked histological and functional kidneys changes.

At 10 weeks of age, rats were allocated to treatment groups based on comparable body weights, ensuring similar baseline characteristics (Fig. 23A). In the 40-week cohort, rats treated with KPT-330 exhibited reduced body weight gain compared with vehicle-treated controls; however, this growth-inhibitory effect subsided once treatment ended at week 20 (Fig. 23B), consistent with findings from previous mouse studies [164]. To evaluate whether fluid retention contributed to the reduced body weight, edema was monitored. Throughout the study, no visible signs of edema, such as limb swelling, were detected during daily inspections. In addition, histological analysis of the kidneys after the 10-week treatment period

revealed no evidence of tubulointerstitial edema (Fig. 23C). Together, these findings indicate that MWF rats did not develop edema up to week 20 and that fluid accumulation is unlikely to account for the body weight differences observed immediately after treatment.

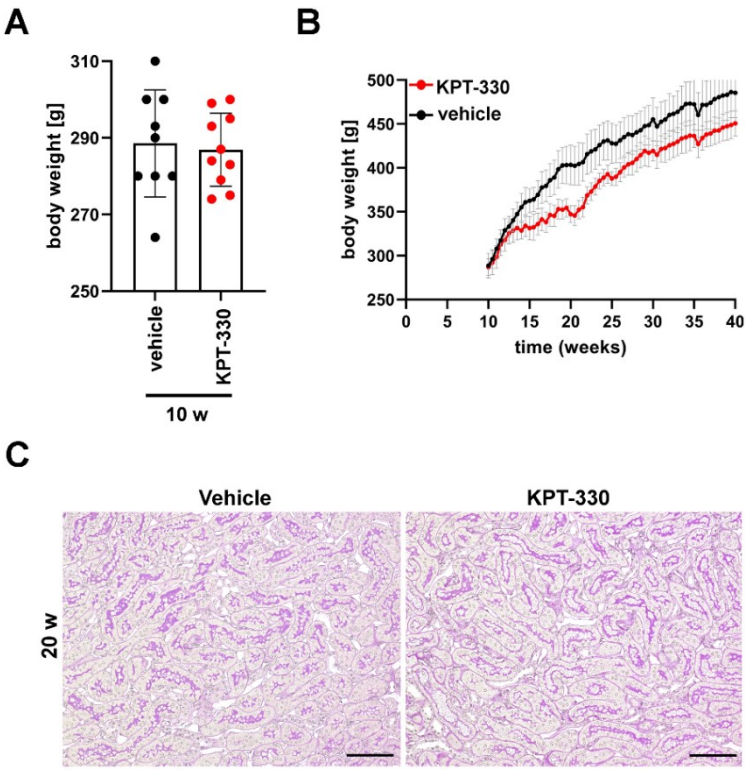


Figure 23. KPT-330 reduces body weight gain in MWF rats [163]. **(A)** Body weight of animals in the 40-week group (approach B) at group allocation (week 10). **(B)** Body weight was monitored twice weekly in vehicle-treated (n=7-9) and KPT-330-treated (n=10) rats. **(C)** PAS-stained renal tissue from vehicle- and KPT-330-treated rats at week 20 showing normal tubulointerstitium without evidence of edema. Scale bar: 100 µm.

Systolic blood pressure in the 40-week-old animals (Fig. 24A) followed a similar trajectory in both groups: rising steeply between weeks 5 and 10 and subsequently stabilizing, with no significant differences between KPT-330 and vehicle groups. In vehicle-treated rats, mean corpuscular hemoglobin (MCH; Fig. 24B) and mean corpuscular volume (MCV; Fig. 24C) gradually declined over the 40-week period. Interestingly, MCH and MCV were transiently preserved in KPT-330-treated rats during the treatment phase.

Taken together, these findings indicate that, under the dosing and regimen applied in this study, KPT-330 exerts detectable physiological effects in the MWF rat model.

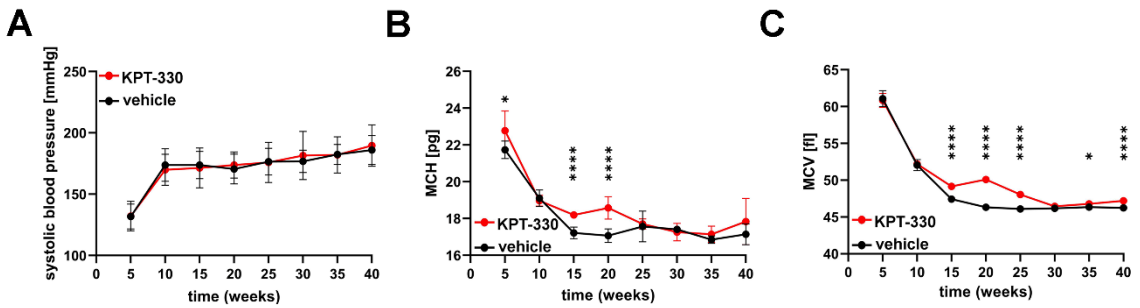


Figure 24. KPT-330 alters general physiological parameters in MWF rats [163]. (A) Systolic blood pressure was measured every five weeks (vehicle: n=7-9; KPT-330: n=10). **(B)** Mean corpuscular hemoglobin (MCH) and **(C)** mean corpuscular volume (MCV) were assessed at the same intervals (vehicle: n=6-9; KPT-330: n=8-10). Please note that some error bars were too small to be visible. All data were collected from 40-week group animals. Data are shown as means ± SD. *P < 0.05, ****P < 0.0001.

4.2.4 KPT-330 Treatment Increases Podocytic NPC Numbers

Changes in nuclear pore complex (NPC) numbers in podocytes during aging and FSGS progression in MWF rats were investigated. Kidney sections were co-stained with mab414, an antibody recognizing multiple nucleoporins within the NPC and widely regarded as a reliable NPC marker [165], and WT-1 to identify podocytes. High-resolution stimulated emission depletion (STED) microscopy revealed that KPT-330 treatment significantly increased podocyte NPC numbers at the end of the treatment period (week 20) compared with vehicle-treated controls (KPT-330: 12.7 ± 1.59 vs. vehicle: 11.07 ± 1.90; P < 0.05) (Figs. 25A, B). This increase was not maintained 20 weeks after treatment cessation (week 40). Concurrently, the mean distance from each NPC to its three nearest neighbors was reduced in KPT-330-treated rats (KPT-330: 0.25 ± 0.012 µm vs. vehicle: 0.27 ± 0.022 µm; P < 0.01), indicating a higher NPC density relative to vehicle-treated animals (Fig. 25C). In summary, NPC numbers in podocytes of MWF rats remain stable with aging but are elevated during KPT-330 treatment, accompanied by a denser spatial arrangement of NPCs.

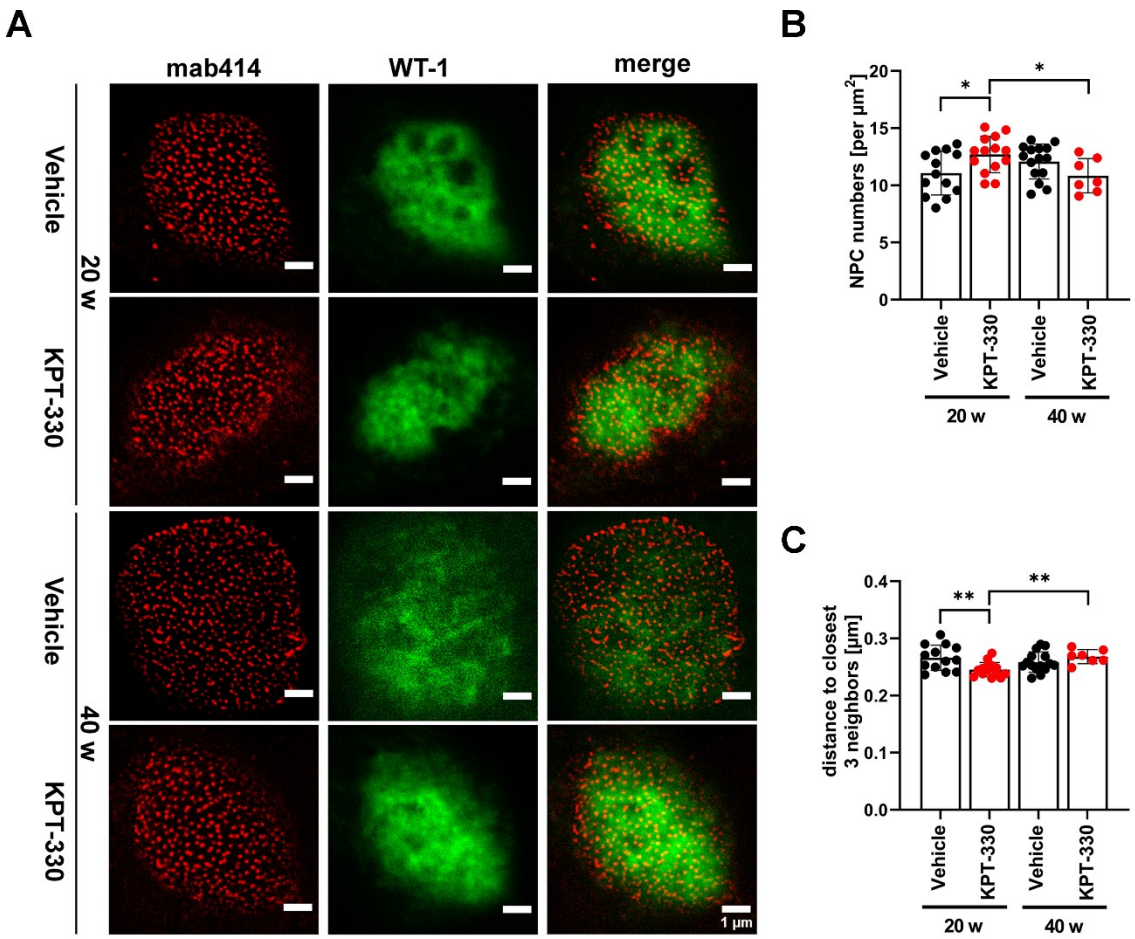


Figure 25. KPT-330 increases podocyte nuclear pore complex (NPC) density at week 20 [163]. (A) Representative high-resolution STED microscopy images of podocytes, identified by the podocyte-specific nuclear marker WT-1 (green signal), with individual NPCs labeled using mab414 (red signal). **(B)** Quantitation of NPCs number per µm² and **(C)** the distance to the three closest neighboring NPCs. Data collected from 7-16 podocytes per condition across three randomly selected animals. The mean clinical parameters (e.g., albuminuria and serum creatinine) of these three selected animals did not differ from the overall group mean values. 20-week group: vehicle (n=13), KPT-330 (n=14); 40-week group: vehicle (n=15), KPT-330 (n=7). Data are shown as means ± SD. *P < 0.05, **P < 0.01. Scale bar: 1 µm

In addition, the staining intensity of Nup93, a core structural component of NPCs, was significantly elevated in podocytes of KPT-330-treated rats compared with vehicle-treated controls at both week 20 (KPT-330: 0.35 ± 1.43 vs. vehicle: 0.20 ± 0.07; P < 0.0001) and week 40 (KPT-330: 0.32 ± 1.59 vs. vehicle: 0.22 ± 0.08; P < 0.001; Fig. 26). Given the high stability of Nup93 within NPCs, this sustained increase likely reflects a longer-lasting effect of KPT-330 relative to the more dynamic nucleoporins detected using the mab414 antibody in STED microscopy [74, 154, 166].

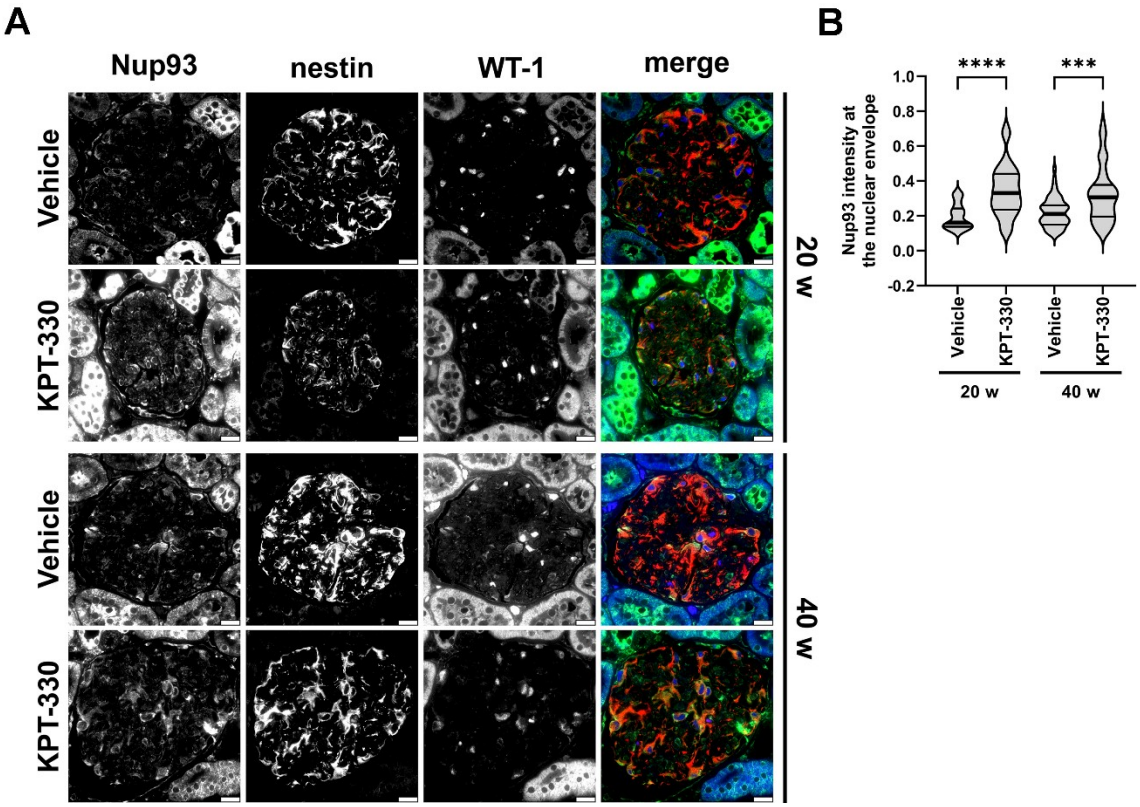


Figure 26. KPT-330 enhances Nup93 staining intensity in podocytes [163]. (A) Representative fluorescence images of podocytes, identified by WT-1 and nestin staining, showing co-staining with Nup93. In the merged image, red indicates nestin staining, blue indicates WT1 staining, and green indicates XPO1 staining. **(B)** Quantification of Nup93 fluorescence intensity at the nuclear envelope. Analysis was performed on 50-85 podocytes per condition. 20-week group: vehicle (n=50), KPT-330 (n=85); 40-week group: vehicle (n=51), KPT-330 (n=56). Data are presented as mean ± SD. *** $P < 0.001$, **** $P < 0.0001$. Scale bar: 20 µm.

4.2.5 KPT-330 Treatment Promotes Nuclear Retention of XPO1 and P53

KPT-330 act as an inhibitor of the nuclear export factor XPO1, which normally cycles between the nucleus and cytoplasm. Following treatment, a marked increase in nuclear enrichment of XPO1 was detected at week 20, reflected by an elevated nuclear-to-cytoplasmic ratio compared with vehicle-treated animals (KPT-330: 1.45 ± 0.24 vs. vehicle: 1.02 ± 0.14; $P < 0.0001$; Fig. 27). However, by week 40, this difference had disappeared, with ratios being comparable between groups (KPT-330: 1.25 ± 0.23 vs. vehicle: 1.23 ±0.24; $P > 0.05$).

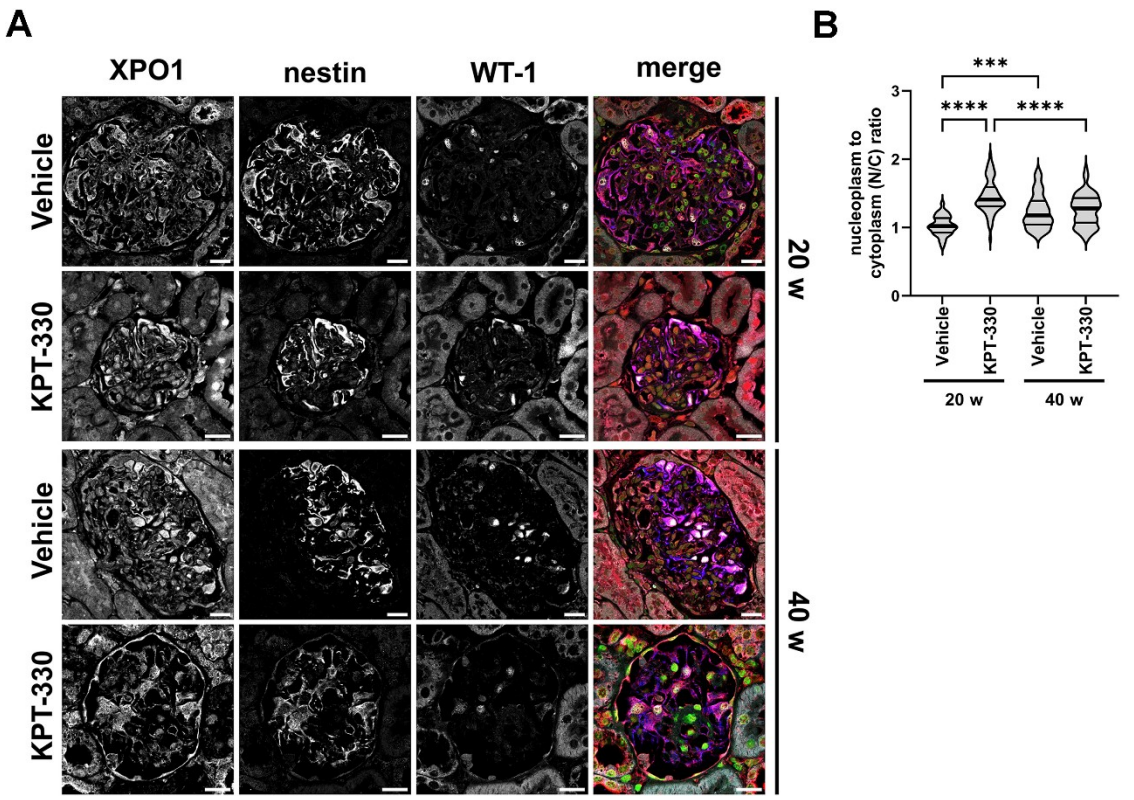


Figure 27. KPT-330 increases nuclear localization of XPO1 [163]. (**A**) Representative confocal images of podocytes stained for XPO1. Nestin served as a cytoplasmic marker specific for podocytes, while WT1 was used to identify podocyte nuclei. In the merged image, red indicates nestin staining, blue indicates WT1 staining, and green indicates XPO1 staining. (**B**) Quantitative analysis of the nuclear-to-cytoplasmic fluorescence intensity ratio of XPO1. A total of 33-82 podocytes per condition were evaluated. 20-week group: vehicle (n=33), KPT-330 (n=71); 40-week group: vehicle (n=41), KPT-330 (n=82). Data are presented as mean ± SD. *** $P < 0.001$, **** $P < 0.0001$. Scale bars: 20 µm.

In line with its mechanism of action, i.e. blocking of XPO1-mediated nuclear export [167], KPT-330 treatment also promoted nuclear accumulation of p53 at week 20, as indicated by a higher nuclear-to-cytoplasmic ratio compared with vehicle-treated controls (KPT-330: 1.70 ± 0.43 vs. vehicle: 1.61 ± 0.43; $P < 0.05$; Fig. 28). By week 40, this effect was no longer detectable (KPT-330: 1.55 ± 0.39 vs. vehicle: 1.61 ± 0.45; $P > 0.05$).

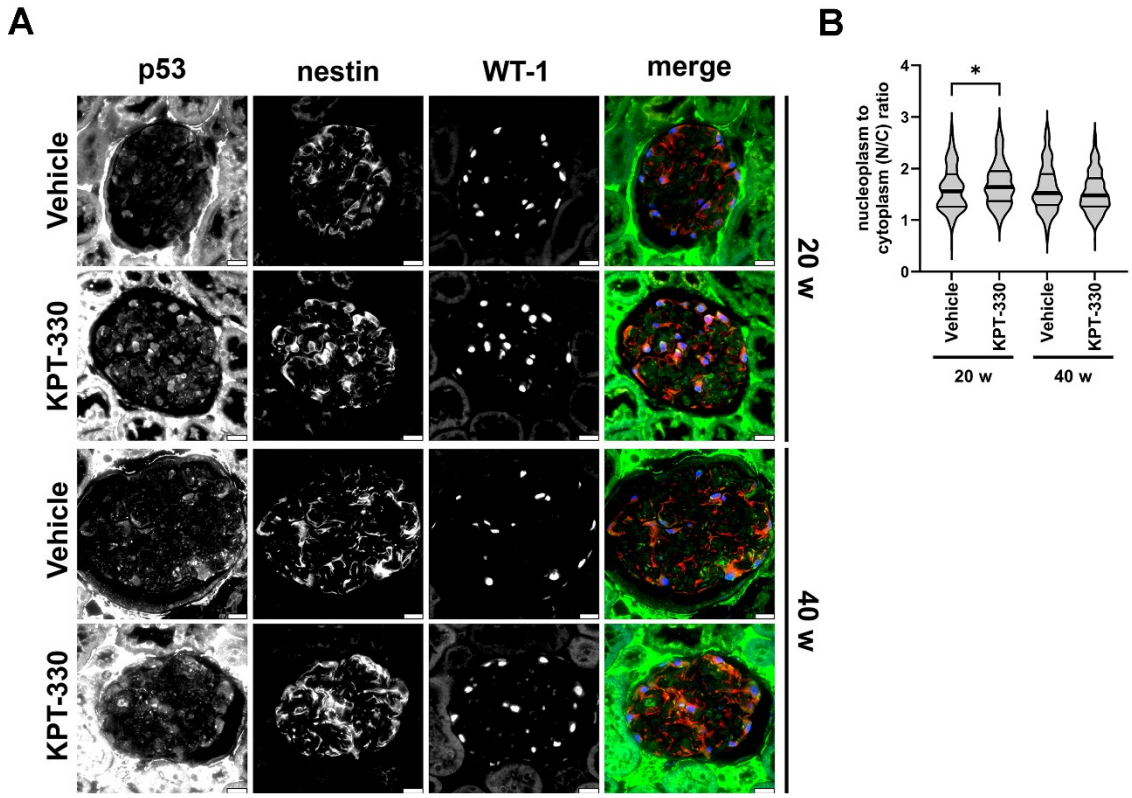


Figure 28. KPT-330 promotes nuclear accumulation of P53 in podocytes [163]. (**A**) Representative fluorescence microscopy images of podocytes stained for p53, with nestin and WT1 serving as cytoplasmic and nuclear markers, respectively. In the merged image, red indicates nestin staining, blue indicates WT1 staining, and green indicates p53 staining. (**B**) Quantification of the nuclear-to-cytoplasmic ratio of p53 staining intensity, measured in 207-475 podocytes per condition. 20-week group: vehicle (n=207), KPT-330 (n=227); 40-week group: vehicle (n=335), KPT-330 (n=475). Data are presented as mean ± SD. * $P < 0.05$. Scale bars: 20 µm.

4.2.6 KPT-330 Treatment Improves Renal Function and Reduces Serum Lipids

The potential association between increased NPC numbers and renal function in FSGS was investigated. During the treatment period from week 10 to week 40, serum creatinine levels consistently decreased in the KPT-330-treated rats, whereas levels in the vehicle group exhibited a gradual increase (week 20: KPT-330 34.11 ± 1.77 µmol/L vs. vehicle 39.25 ± 3.54 µmol/L; $P < 0.01$) (Fig. 29A). After cessation of treatment, creatinine levels rose in both groups; however, values in the KPT-330 cohort remained lower and only reached the levels observed in vehicle-treated animals by the end of the study at week 40 (Fig. 29A). A comparable trend was observed for BUN, which decreased during the administration period from week 10 to week 20 (Fig. 29B). Serum cystatin C was also reduced in KPT-330-treated rats at week 20, and this reduction persisted through week 40 (KPT-330 3.62 ± 0.39 µg/ml vs. vehicle 4.19 ± 0.44 µg/ml; P <

0.05), 20 weeks after the final dose (Fig. 29C). No significant differences in albuminuria were detected between groups at any time point (Fig. 29D). In addition to primary parameters of kidney function, serum lipids and electrolytes were evaluated. Serum triglycerides and total cholesterol levels were significantly lower in the KPT-330 group at week 20 (Figs. 29E and F), consistent with improved renal function; however, these effects were not sustained at week 40. Overall, these results demonstrate that KPT-330 enhances renal performance and alleviates hyperlipidemia during FSGS progression.

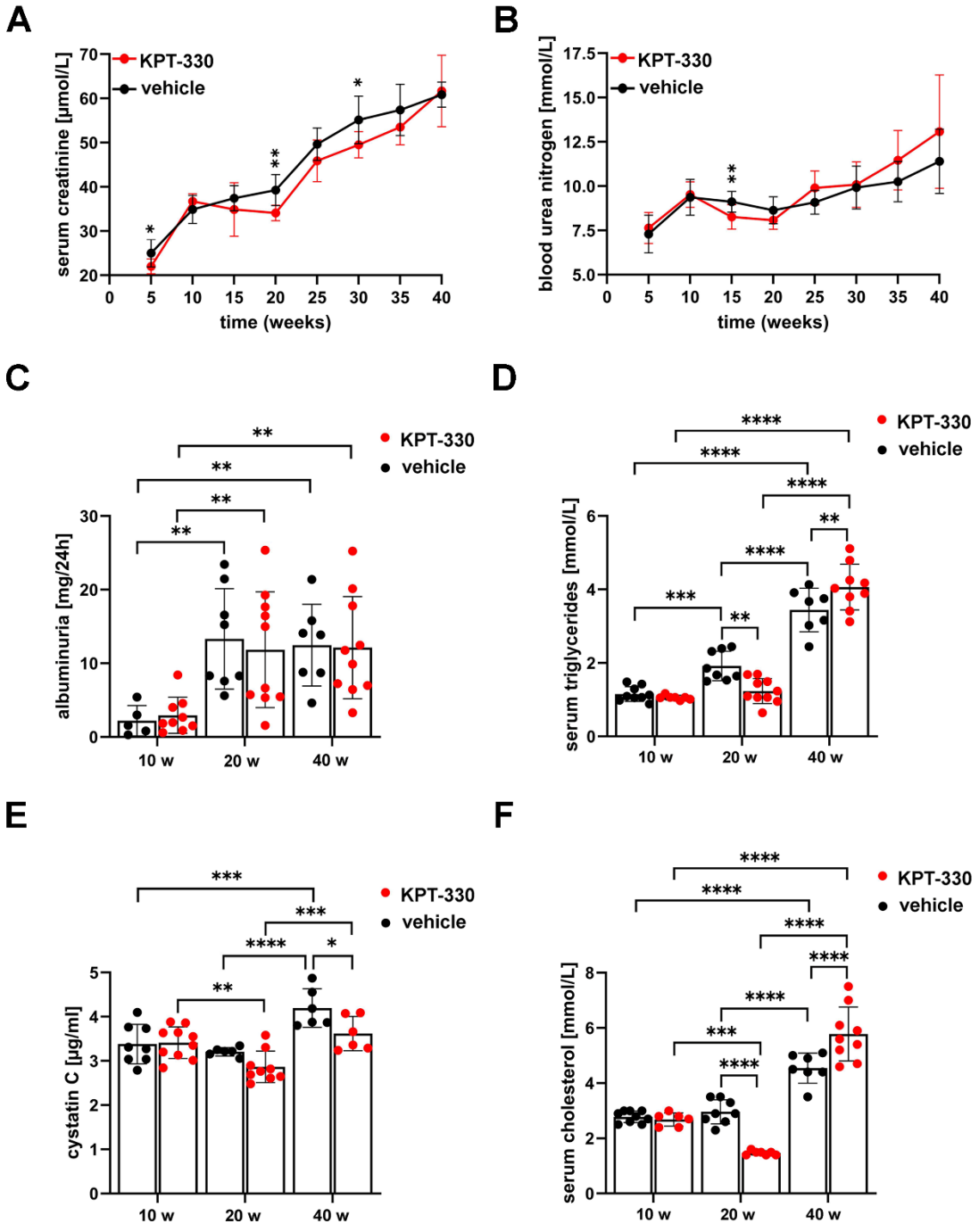


Figure 29. KPT-330 treatment modestly improves renal function and reduces hyperlipidemia [163]. Longitudinal measurements of **(A)** serum creatinine (vehicle: n =

7-9; KPT-330: n = 7-10) and **(B)** blood urea nitrogen (BUN; vehicle: n = 7–9; KPT-330: n = 9–10) are shown, along with **(C)** serum cystatin C concentrations at weeks 10, 20, and 40 (vehicle: n = 6-8; KPT-330: n = 6-10). **(D)** Twenty-four-hour albuminuria, calculated from urine albumin concentration and urine volume collected during a 15-hour metabolic cage session (vehicle: n = 5-8; KPT-330: n = 9-10). **(E)** Serum triglyceride (vehicle: n = 7-9; KPT-330: n = 7-10) and **(F)** total cholesterol levels (vehicle: n = 7-9; KPT-330: n = 6-9; two week-20 KPT-330 samples were below the detection limit, <1.3 mmol/L, therefore, were not included) are shown. All measurements were obtained from animals in the 40-week cohort (approach B), and data are expressed as mean ± SD. *P < 0.05, **P < 0.01, ***P < 0.001, ****P < 0.0001.

Serum phosphate levels varied over time regardless of KPT-330 treatment (Fig. 30A), likely reflecting altered phosphate handling as CKD progressed. Similar to the phosphate levels, KPT-330 treatment also had no effect on serum potassium or sodium levels at any time point (Figs. 30B, C).

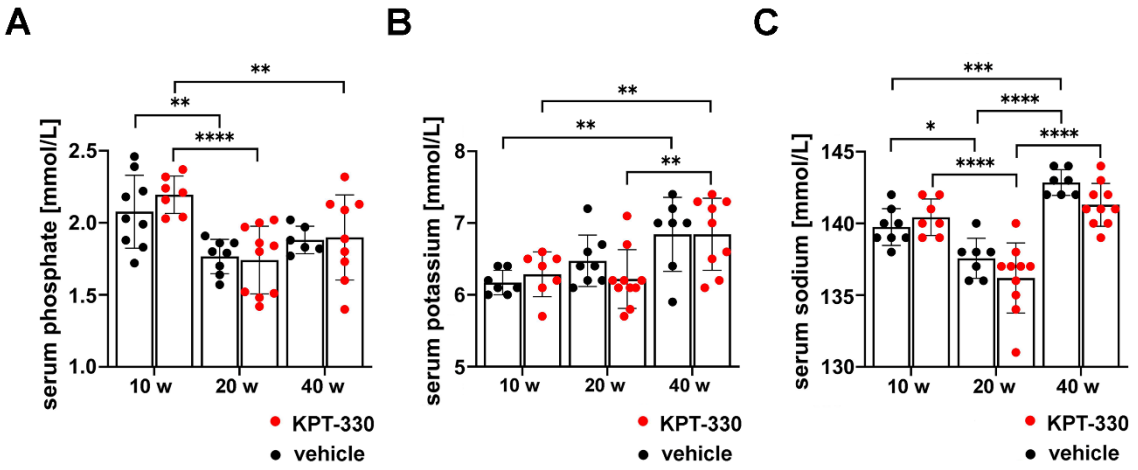


Figure 30. Serum phosphate, potassium, and sodium levels during disease progression are not significantly affected by KPT-330 treatment [163]. (A) Serum phosphate levels (vehicle: n=7-8; KPT-330: n=7-10), **(B)** serum potassium levels (vehicle: n=6-9; KPT-330: n=7-10), and **(C)** serum sodium levels (vehicle: n=7-8; KPT-330: n=7-10), all measured at 10, 20, and 40 weeks. All samples were from the 40-week group (approach B) animals. Data are shown as means ± SD. *P < 0.05, **P < 0.01, ***P < 0.001, ****P < 0.0001.

4.2.7 KPT-330 Does Not Halt FSGS Progression

KPT-330 administration transiently lowered the incidence of synechiae at week 20; however, by week 40 the frequency had risen again, with no significant difference compared with vehicle controls (Figs. 31A, B). In contrast, glomerulosclerosis scores were consistently higher in the KPT-330-treated group relative to vehicle-treated animals, and this difference became statistically significant at week 40 (Figs. 31A, C).

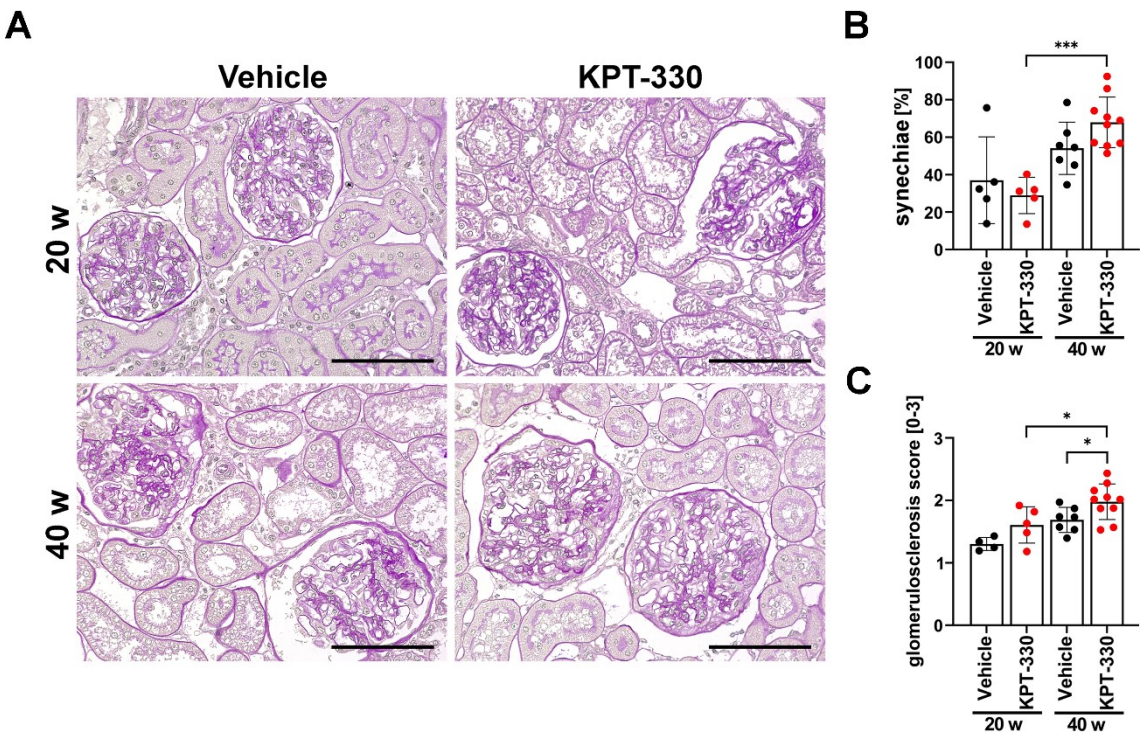


Figure 31. KPT-330 fails to prevent FSGS progression [163]. (A) Representative PAS-stained kidney sections from vehicle- and KPT-330-treated rats at 20 and 40 weeks. **(B)** Percentage of glomeruli displaying synechiae between the capillary tuft and Bowman's capsule. **(C)** Glomerulosclerosis severity scores assessed across entire kidney sections. 20-week group: vehicle (n=4-5), KPT-330 (n=5); 40-week group: vehicle (n=7), KPT-330 (n=10). Data are shown as means ± SD. *P < 0.05, ***P < 0.001. Scale bar: 100 µm.

As FSGS advanced, a pronounced decline in WT-1-positive podocytes was observed in both treatment groups from week 20 to week 40, without any significant differences between KPT-330- and vehicle-treated animals at either time point (Fig. 32A). Glomerular CD44 expression, a marker of activated PECs, showed no group-specific variation at week 20 (Fig. 32B), but was markedly higher in KPT-330-treated rats by week 40 (Fig. 32B). Collagen IV accumulation displayed a similar pattern, rising in both treatment groups and mirroring the CD44 pattern, reaching statistical significance at week 40 (Fig. 32C). When glomerular area was normalized to body weight, no significant differences emerged between groups, either directly after treatment at week 20 or later at week 40, indicating that KPT-330 does not influence glomerular hypertrophy (Fig. 32D).

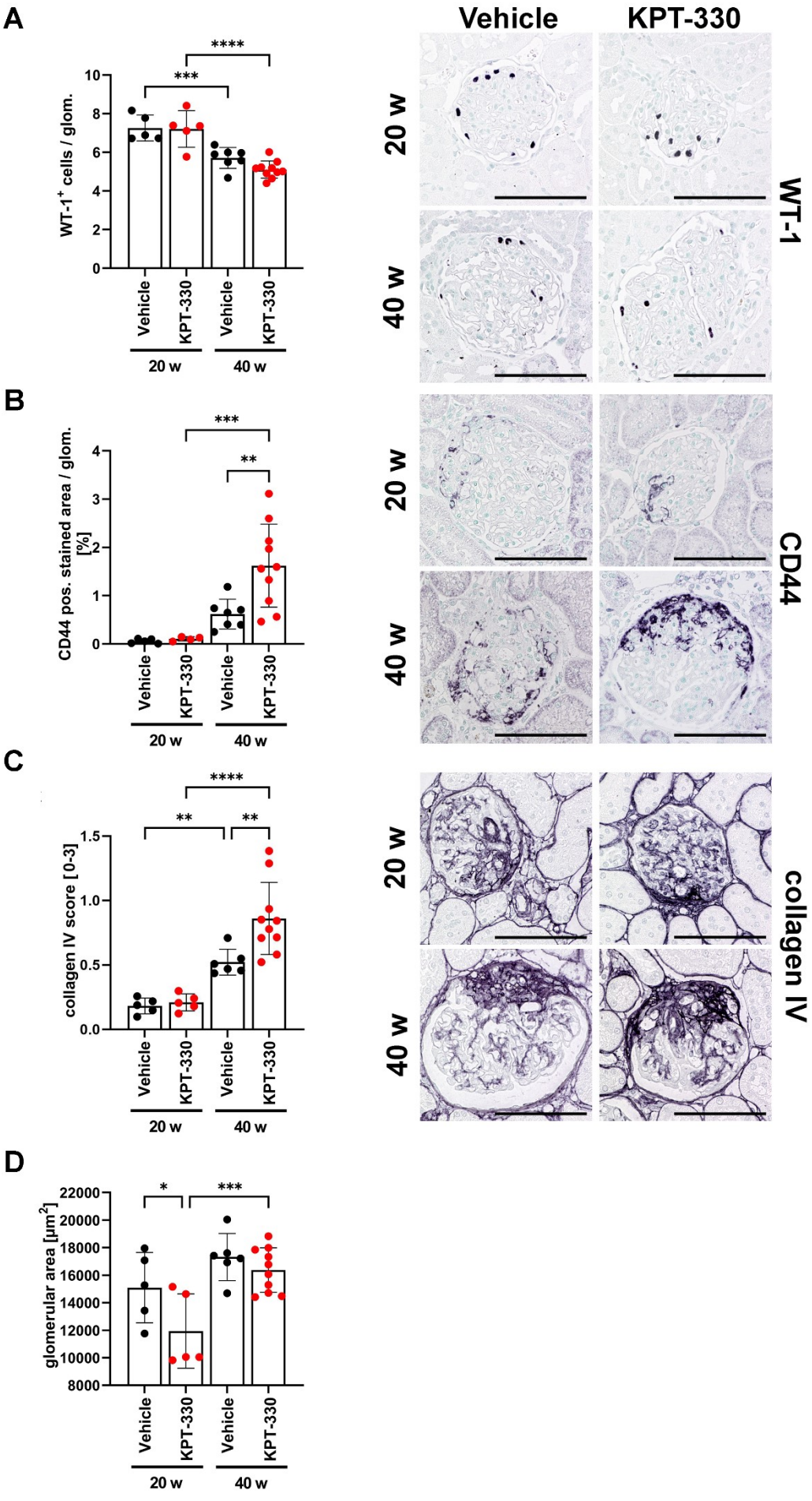

A
B
C
D
Vehicle
KPT-330
20 w
40 w
WT-1
CD44
collagen IV
WT-1+ cells / glom.
CD44 pos. stained area / glom. [%]
collagen IV score [0-3]
glomerular area [µm2]
Vehicle
KPT-330
Vehicle
KPT-330
20 w
40 w

Figure 32. Podocyte depletion, PEC activation, and glomerular matrix deposition continue after KPT-330 treatment [163]. (A) Quantification of WT-1-positive podocytes per glomerulus in vehicle and KPT-330 treated rats at weeks 20 and 40, with representative stainings shown to the right. (**B**) Fraction of CD44-positive area within the glomeruli with representative stainings on the right. **(C)** Proportion of collagen IV-positive area in the glomerular tuft, with representative stainings on the right. **(D)** Mean glomerular area per animal, adjusted for body weight. 20-week group: vehicle (n=5), KPT-330 (n=5); 40-week group: vehicle (n=6-7), KPT-330 (n=10). Data are shown as means ± SD. **P < 0.01, ***P < 0.001, ****P < 0.0001. Scale bars: 100 µm.

In summary, although KPT-330 improves renal function and reduces hyperlipidemia, it fails to halt the long-term progression of FSGS in MWF rats after treatment withdrawal.

5 Discussion

The present thesis systematically characterized how nuclear-cytoplasmic protein localization changes across different ages in primary mouse podocytes. This analysis identified both previously recognized mislocalized proteins known from other postmitotic cell types, as well as novel podocyte-specific candidates whose spatial proteome remodeling emerges as a hallmark of aging. Complementing these mechanistic findings, the short- and long-term evaluation of nuclear export inhibition with KPT-330 in a spontaneous FSGS rat model showed that pharmacological modulation of nuclear transport can partially restore aspects of podocyte homeostasis and improve kidney function. Together, these findings highlight nucleocytoplasmic transport dysregulation as a convergent mechanism linking aging-associated podocyte decline with glomerular disease progression.

5.1 Aging Predisposes Mice to FSGS-like Pathology and Is Accompanied by Loss of Podocytes

Age-associated structural changes in the kidney and glomerulus have been consistently recognized for more than a century [168]. Human biopsy studies further support this concept. In a cohort of 1203 healthy living kidney donors, the prevalence of glomerulosclerosis increased steadily across age groups, rising from young adulthood to advanced age [169, 170]. These data support the concept that aging is an independent risk factor for glomerular scarring, even among otherwise healthy individuals. Consistent with these human observations, the mouse model used in this study demonstrated a clear age-related progression of FSGS-like pathology. Even at 11 weeks, roughly corresponding to early adulthood in humans [171], mice already exhibited a small proportion of glomeruli with abnormal synechiae. This proportion increased further by 35 weeks, a stage equivalent to mid-life [171], and reached its highest levels at 80 weeks, representing an elderly phase [171]. Thus, aging mice recapitulate the gradual, spontaneous development of segmental scarring observed in aging humans. As early as 1997, Floege et al. described age-related glomerulosclerosis as a podocyte disorder [172]. In the present study, pathological progression was likewise accompanied by a parallel decline in podocyte number. Podocyte depletion became particularly pronounced between 35 and 80 weeks, supporting the well-established concept that podocytes in aged organisms are structurally

fragile, less able to compensate for injury, and prone to detachment [173]. Correspondingly, age-related deterioration in renal function was mainly evident between mid-life and advanced age, consistent with podocyte loss reaching a critical threshold beyond which glomerular filtration becomes compromised [174]. Together, these findings indicate that aging not only increases susceptibility to FSGS-like glomerular injury but also establishes a biological context in which podocyte maintenance mechanisms progressively fail.

5.2 Methodological Considerations for Primary Podocyte Isolation in Aging Research

Low cell yield during isolation has long been a major obstacle for studies on primary podocytes. Many researchers have attempted to improve podocyte yield. In 2013, Boerries et al. [109] optimized the magnetic bead method originally described by Takemoto et al. [175] using a reporter mouse line. They introduced three main modifications to the standard protocol, which substantially increased the yield to an average of 500,000 podocytes per mouse. However, in order to maximize magnetic bead delivery into glomeruli, perfusion was performed via the renal artery instead of the heart, which is technically challenging. In addition, perfusion with Dynabeads is costly when a large number of animals are required. Another widely used approach to isolate glomeruli is based on their size [175]. In mice, use of a 40-µm strainer allows retention of glomeruli on the mesh while most renal tubules pass through [110].

In this study, mice were perfused with 0.9% NaCl, and glomeruli were isolated using two different sizes of strainers: a 70-µm strainer for mechanical tissue dissociation, and a 40-µm strainer to separate glomeruli from tubules. Taking advantage of this mouse line, contamination by tubular fragments was mitigated by podocyte-specific eGFP expression, and no additional purification steps were applied. Nevertheless, simple washing of the strainer by pipette flushing resulted in low glomerular yield. To overcome glomerular adhesion to the filter membrane, a syringe-needle flushing system was introduced, which led to a marked improvement in glomerular recovery. To obtain a single-cell suspension from the glomerular fraction, an additional enzymatic digestion step was performed as described by Boerries et al. [109]. This isolation strategy combines mechanical enrichment with enzymatic dissociation and reporter-based cell specificity, allowing the reproducible collection of intact podocyte populations across

different age groups. Moreover, according to Wang et al., compared with the Dynabeads method, the mechanical enrichment of glomeruli also induces less inflammatory stress [110]. This methodological consistency is particularly critical for aging-related proteomic analyses, as it minimizes technical bias and ensures that observed changes in protein localization and abundance predominantly reflect true biological aging processes rather than isolation-induced artifacts. Thus, the protocol provides a robust and cost-effective foundation for high-confidence spatial proteomic profiling of aging podocytes.

5.3 Age-dependent Remodeling of the Podocyte Spatial Proteome

Aging refers to the gradual progression toward advanced biological age, whereas senescence describes the decline in cellular function that emerges during this process [177]. Several candidate pathways underlying physiological age-associated changes in podocytes have been proposed, including oxidative stress, epigenetic alterations, cellular senescence, sirtuin signaling, impaired autophagy, and increased apoptosis [178]. More recently, accumulating evidence has identified an additional age-associated mechanism involving the progressive accumulation of misassembled NPCs and dysfunctional nucleocytoplasmic signaling in aged and senescent cells [71, 179, 180]. As terminally differentiated, postmitotic cells, podocytes are therefore particularly susceptible to the long-term accumulation of NPC damage and progressive protein mislocalization during aging.

An age-dependent nuclear accumulation of SMCR8 in podocytes was observed here, although the molecular function of nuclear SMCR8 remains largely undefined. Previous work has suggested that SMCR8 can associate with chromatin in proximity to autophagy-related gene loci, including ULK1 and WIPI2, and suppress their transcriptional activity [181]. This regulatory mechanism is consistent with the well-documented decline in autophagic capacity observed in aged podocytes [182]. Importantly, SMCR8 lacks a clearly defined nuclear localization or export sequence; its nuclear presence in the present study therefore suggests the involvement of non-classical or indirect transport mechanisms in aged podocytes [181].

In this study, Ran exhibited a progressive, age-associated redistribution toward

the nuclear compartment. Although the mechanistic basis for this shift remains unclear, previous studies have demonstrated that age-related disruption of nuclear envelope integrity and cellular stress can perturb the Ran-GTP/GDP gradient and alter the subcellular distribution of Ran [74, 123]. Given the central role of Ran in coordinating nucleocytoplasmic transport, this age-dependent change in Ran localization suggests that the overall nuclear transport machinery is progressively compromised in aged podocytes, potentially contributing to impaired protein trafficking and cellular homeostasis.

In contrast to these alterations, cytoplasmic localization of eIF4E was consistently observed at all three analyzed time points, and no significant translocation was detected. Previous studies have reported nuclear accumulation of eIF4E in response to cellular stress or nutrient deprivation [124]. Based on this, a similar redistribution might have been anticipated during podocyte aging, as increased oxidative and metabolic stress are widely recognized contributors to age-associated podocyte dysfunction. However, podocyte hypertrophy represents a prominent and well-established feature of aging and chronic glomerular stress, which is strongly dependent on increased protein synthesis [183]. Sustained cytoplasmic localization of eIF4E is therefore likely to play its typical function, i.e. serving as a central component of the translation initiation machinery and being required to support elevated translational activity in aging podocytes. Thus, the stable cytoplasmic distribution of eIF4E observed in this study may reflect a balance between stress-induced nuclear signaling and the persistent demand for cytoplasmic protein synthesis.

Although DRG2 has mainly been described as a cytoplasmic protein involved in regulation of cell growth and differentiation [124], very little is known about its function in terminally differentiated podocytes. In the present study, an age-associated alteration in the N/C ratio of DRG2 was observed, characterized by a transient decrease at mid-age followed by a significant increase in aged animals. While the functional relevance of this redistribution remains unclear, this finding suggests that aging may subtly affect the subcellular organization of proteins not previously linked to nuclear transport in podocytes.

Taken together, these findings provide experimental support for the central hypothesis that aging in podocytes is accompanied by progressive impairment of NPC-dependent compartmentalization, leading to selective and protein-specific

redistribution between nuclear and cytoplasmic compartments. Rather than reflecting a uniform failure of nuclear transport, the observed patterns suggest a gradual erosion of transport fidelity, which may represent an early molecular driver of age-associated podocyte dysfunction.

5.4 Proteomic Identification of Podocyte-specific Spatial Remodeling Markers

Proteomic analysis revealed a global, age-associated remodeling of the podocyte spatial proteome. Volcano plot-based differential analysis identified a subset of proteins displaying significant changes in their N/C ratios, indicating that protein relocalization during aging follows coordinated and biologically structured patterns rather than random, uncoordinated redistribution.

Proteins exhibiting increased nuclear localization with aging were strongly enriched for mitochondrial organization, oxidative phosphorylation, and electron transport chain pathways. Notably, many of the proteins showing the strongest age-dependent nuclear enrichment are nuclear-encoded mitochondrial proteins. These proteins must traverse one of the longest and most complex intracellular trafficking routes, requiring sequential passage through the nuclear pore complex, the cytosol, and the TOM/TIM mitochondrial translocase system. This extended transport chain renders mitochondrial precursor proteins intrinsically sensitive to defects in both nucleocytoplasmic transport and mitochondrial import, such that their mislocalization is more likely to reflect a trafficking bottleneck rather than simple passive equilibration. In this context, the pronounced age-dependent amplification of Tomm40 nuclear accumulation may indicate progressively altered regulation or reduced efficiency of the mitochondrial translocase (TOM/TIM) machinery [184]. Impaired import could result in cytosolic retention or mislocalization of nuclear-encoded mitochondrial precursor proteins. Consistent with this model, defective mitochondrial import has been shown to redirect precursor proteins to the nucleus for quality control and degradation [185], a process now recognized as part of mitochondrial protein translocation-associated degradation and nuclear surveillance of non-imported mitochondrial proteins [186, 187]. Beyond being a passive consequence of failed import, nuclear accumulation of mitochondrial proteins may also constitute an active mitochondrial-to-nuclear stress signaling pathway. Numerous mitochondrial proteins have been shown to shuttle to the nucleus, where they directly regulate

transcription, chromatin state, and stress-responsive gene programs [188, 189]. Analogous to the mitochondrial unfolded protein response, mislocalized mitochondrial precursors in the nucleus could modulate transcriptional programs that regulate metabolism, stress resistance, and cell survival [190, 191]. In aging podocytes, such mitochondrial precursor-mediated nuclear stress signalingmay therefore contribute to the observed metabolic rewiring and represent an adaptive response to declining mitochondrial performance rather than a purely degenerative process.

Beyond ATP production, mitochondria participate in sugars, lipids, amino acid, and heme metabolism [192, 193]. The observed redistribution of TOM/TIM components and respiratory chain proteins therefore suggests that aging podocytes undergo compensatory metabolic remodeling. Accordingly, proteins shifting toward the cytoplasm were enriched for metabolic processes, glycolytic pathways, and cofactor-dependent enzymatic activities. This pattern is consistent with a metabolic shift from mitochondrial oxidative metabolism toward increased reliance on cytoplasmic glycolysis, a phenomenon broadly described in aging and stress adaptation [194, 195]. Such metabolic reprogramming is a hallmark of mitochondrial stress and mitonuclear imbalance, in which declining respiratory capacity, increased reactive oxygen species, and disturbed NAD^+/NADH homeostasis force cells to compensate by upregulating glycolytic and cytosolic energy-generating pathways [196, 197]. In podocytes, which are highly energy-demanding, postmitotic cells that rely on continuous ATP supply to maintain their actin cytoskeleton and resist biomechanical stress at the glomerular filtration barrier, mitochondrial dysfunction is particularly deleterious [198, 199, 200, 201, 202]. A shift toward glycolysis may initially serve as an adaptive response to sustain cellular viability when mitochondrial oxidative phosphorylation becomes inefficient. However, chronic reliance on cytoplasmic metabolism is likely maladaptive in podocytes, as mitochondrial stress-associated redox imbalance and altered metabolite homeostasis are known to destabilize cytoskeletal organization and promote foot process effacement [203]. Thus, the observed age-dependent redistribution of metabolic enzymes toward the cytoplasm likely reflects a metabolic trade-off that transiently preserves energy production at the cost of long-term structural integrity, thereby linking mitochondrial dysfunction to progressive podocyte loss and FSGS development.

Several limitations should be acknowledged. First, sex-dependent differences in subcellular podocyte proteome profile could not be addressed due to technical constraints, although transcriptomic studies indicate that age accounts for a much larger fraction of expression variance than sex in podocytes [178]. Second, direct measurements of NPC number or functional permeability were not performed, and therefore a causal link between NPC dysfunction and protein relocalization cannot yet be conclusively established.

5.5 KPT-330 Enhanced Renal Function in MWF rats but Could Not Halt the Histological Damage Progression in the Current Setting

In this study, selinexor (KPT-330) is shown to compensate for defects in nuclear pore complex (NPC) transport or permeability in a cell culture model. In the Munich Wistar Frömter (MWF) rat, a spontaneous model of focal segmental glomerulosclerosis (FSGS), administration of KPT-330 for ten weeks results in an increased number of podocyte NPCs and higher Nup93 immunoreactivity. Functional parameters of renal performance improved following KPT-330 therapy, as indicated by reduced serum creatinine at the end of the treatment phase and lower serum cystatin C levels twenty weeks thereafter. However, histopathological examination does not reveal a lasting mitigation of FSGS progression under the current dosing regimen.

Selinexor (KPT-330) acts as a selective inhibitor of nuclear export by binding to and blocking exportin 1 (XPO1), a major mediator of nuclear-cytoplasmic transport [204]. During the treatment period, the continuous loss of body weight together with changes in MCV and MCH indicated that the chosen administration frequency and dosage of KPT-330 were sufficient to elicit systemic pharmacodynamic effects in MWF rats. The improvements in MCV and MCH may be related to alterations in iron metabolism, as selinexor has been reported to modulate transcription factors involved in iron homeostasis [88].

By preventing XPO1-dependent protein export, KPT-330 induces nuclear retention of several key regulators, including tumor suppressors and cell cycle-controlling proteins. Consistent with this mechanism, increased nuclear p53 localization was detected in podocytes following KPT-330 treatment. While nuclear accumulation of p53 is well known to induce cell-cycle arrest and apoptosis in cancer cells, forming the basis of KPT-330's oncological application

[161, 205], p53 appears to exert a distinct function in podocytes. In differentiated mouse podocyte clone-5 cells, nuclear p53 has been reported to promote the expression of key podocyte-specific genes, including *Nephrin*, *Podocin*, and *WT-1*, supporting a protective and differentiation-maintaining role in this cell type. Furthermore, podocyte-specific deletion of p53 accelerates renal dysfunction in experimental alport syndrome, while having no detectable effect on normal renal function, highlighting that p53 signaling is selectively required under mechanical or pathological stress conditions [206]. Both alport syndrome and MWF-associated FSGS represent podocyte depletion-driven glomerulosclerosis that are characterized by increased biomechanical stress at the glomerular filtration barrier, despite different primary etiologies [207, 208]. In this context, it is therefore plausible that, in MWF rats, inhibition of XPO1 and consequent nuclear accumulation of essential nuclear proteins in podocytes contribute to the functional protective effects observed. It should be noted, however, that selinexor exerts systemic effects and is not podocyte-specific. Consequently, the observed renal benefits are likely to involve additional mechanisms in other glomerular and extraglomerular cell types, which were not directly addressed in the present study and warrant further investigation.

Prior work also suggests that enrichment of transport receptors such as XPO1 at the NPC may strengthen its selective permeability barrier [209]. This barrier is primarily maintained by intrinsically disordered FG (phenylalanine-glycine) nucleoporins that line the NPC channel; their interaction with transport receptors can compact the central channel, thereby tightening the permeability filter [210]. Consequently, KPT-330 might indirectly influence NPC permeability through effects on XPO1. Supporting this notion, in vitro data show that both XPO1 inhibitors, KPT-330 and leptomycin B (LMB), are able to restore the integrity of a compromised NPC barrier. Thus, XPO1 inhibition by KPT-330 may reinforce NPC selectivity and permeability, as confirmed by the cell culture findings. Notably, KPT-330 has also demonstrated beneficial effects in a mouse model of progeria [211] and has been explored for antiviral applications [212]. In these contexts, KPT-330 reduces SARS-CoV-2 infection and protects respiratory tissues in ferret models of COVID-19 [213] as well as improving outcomes in sepsis [214]. Collectively, these data, together with the present findings, suggest that the therapeutic potential of KPT-330 extends beyond oncology into broader disease contexts.

Guided by the in vitro observations that XPO1 inhibition enhances the NPC permeability barrier, the in vivo effects of KPT-330 were assessed in MWF rats developing spontaneous FSGS. Treatment results in decreased serum creatinine and blood urea nitrogen (BUN) during the initial 20 weeks. However, because KPT-330-treated rats exhibit reduced body weight, serum creatinine alone may not be a reliable indicator of renal function. Importantly, serum cystatin C, which is less affected by muscle mass and other extrarenal factors [215] remains significantly lower at week 40 in the treated group, suggesting a sustained renal benefit. A temporary decline in serum lipid levels at week 20 is also observed, further indicating metabolic improvement. As MWF rats are not known to harbor mutations in nucleoporin genes [216], these data suggest that general enhancement of NPC barrier function may benefit FSGS independently of specific genetic alterations.

Although cystatin C levels improve, the inconsistent effects of KPT-330 on albuminuria highlight the complexity of glomerular recovery, in which temporary functional gains may not prevent podocyte loss or fibrosis. Restoration of kidney function does not necessarily imply structural repair, as persistent fibrosis can continue despite improved filtration. A similar dissociation between renal function and fibrosis has been reported in adenine-induced nephropathy [217]. At week 20, histological evaluation reveals no significant differences in podocyte density or glomerulosclerosis between KPT-330- and vehicle-treated groups, indicating that XPO1 inhibition provides only transient functional improvement without preventing structural progression of FSGS. The dissociation between improved renal function and persistent structural damage suggests that XPO1 inhibition does not primarily reverse fibrosis or glomerular scarring, but rather enhances the stress tolerance and functional reserve of surviving podocytes. In this regard, KPT-330 may act as a cellular resilience modifier, increasing the ability of podocytes to withstand mechanical and metabolic stress even in a structurally compromised glomerular environment. Such a mechanism would explain why filtration parameters improve while sclerosis continues to progress. Given KPT-330's anti-proliferative activity, it is reasonable to suspect that XPO1 inhibition could modulate proliferative/activated PEC responses in FSGS. However, CD44, a receptor for hyaluronic acid and a marker of activated parietal epithelial cells (PECs) in sclerotic glomeruli [218, 219, 220], was increased in the KPT-330 group, suggesting elevated PEC activation and possible promotion of

glomerulosclerosis. These observations underscore that XPO1 blockade alone may not suffice to halt chronic kidney injury.

A limitation of the study is that KPT-330 administration was terminated after ten weeks. Prolonging treatment throughout the full 30-week observation period may have yielded stronger or more sustained improvements. Nevertheless, this investigation provides preliminary in vivo evidence that modulation of nuclear transport can influence disease-relevant functional parameters in FSGS.

In summary, this thesis demonstrates that aging induces progressive erosion of nucleocytoplasmic transport fidelity in podocytes, accompanied by coordinated remodeling of their spatial proteome and metabolic landscape. These findings identify NPC dysfunction and mitochondrial import stress as interconnected drivers of podocyte vulnerability, positioning spatial proteomics as a powerful approach for detecting early molecular signatures of age-associated glomerular injury. Moreover, the partial therapeutic efficacy of KPT-330 underscores that modulation of nuclear transport pathways represents a promising, yet still incomplete, strategy to restore podocyte homeostasis.

6 Outlook

Based on the findings presented here, several directions for future research emerge.

First, although age-associated redistribution of nuclear and cytoplasmic proteins strongly suggests impaired nucleocytoplasmic transport fidelity in podocytes, direct quantitative assessment of nuclear pore complex (NPC) number, composition, and permeability in aging podocytes is still lacking. Future studies combining ultrastructural approaches, such as super-resolution microscopy or electron tomography, with functional transport assays will be required to establish a causal link between NPC deterioration and spatial proteome remodeling.

Second, the present study identifies mitochondrial protein mislocalization and mitochondrial import stress as prominent features of podocyte aging. However, it remains unclear whether nuclear accumulation of mitochondrial proteins represents a protective quality control mechanism, a maladaptive stress response, or a signaling pathway actively contributing to podocyte dysfunction. Addressing this question will require time-resolved analyses and genetic or pharmacological perturbation of mitochondrial import pathways to dissect cause-effect relationships.

Third, while pharmacological inhibition of nuclear export using selinexor (KPT-330) improved renal functional parameters, it failed to prevent structural disease progression. This highlights the need for a deeper understanding of the temporal window, dosage, and cell-type specificity required for effective modulation of nucleocytoplasmic transport in chronic glomerular disease. Combination strategies targeting both nuclear transport integrity and mitochondrial or metabolic stress pathways may represent a more effective therapeutic approach than nuclear export inhibition alone. Further research is also warranted to elucidate the molecular links between NPC dysfunction and FSGS pathogenesis.

Finally, the spatial proteomic framework established in this thesis provides a foundation for future biomarker discovery. Validation of candidate proteins identified here in human podocyte samples or patient-derived material will be essential to determine their translational relevance. Extending spatial proteomics to earlier disease stages or additional podocyte injury models may further clarify whether nucleocytoplasmic transport defects represent an initiating event or a

downstream consequence of podocyte damage.

Addressing these questions will be critical for translating the mechanistic insights from this thesis into effective interventions for age-associated glomerular disease and focal segmental glomerulosclerosis.

References

1. Finco DR. Kidney function. In: *Clinical biochemistry of domestic animals*. Elsevier; 1997. p. 441-84. doi:10.1016/B978-012396305-5/50018-X.

2. Beena V. Excretory Physiology. In: *Textbook of Veterinary Physiology*. Springer; 2023. p. 213-31. doi:10.1007/978-981-19-9410-4_9.

3. Smith HW. *The kidney: structure and function in health and disease.* Oxford University Press; 1951.

4. Greka A, Mundel P. Cell biology and pathology of podocytes. *Annu Rev Physiol.* 2012;74:299-323. doi:10.1146/annurev-physiol-020911-153238.

5. Dalal R, Bruss ZS, Sehdev JS. Physiology, renal blood flow and filtration [Internet]. Treasure Island (FL): StatPearls Publishing; 2018.

6. Lennon R, Randles MJ, Humphries MJ. The importance of podocyte adhesion for a healthy glomerulus. *Front Endocrinol (Lausanne).* 2014;5:160. doi:10.3389/fendo.2014.00160.

7. Bruno V, Muhlig AK, Oh J, Licht C. New insights into the immune functions of podocytes: the role of complement. *Mol Cell Pediatr.* 2023;10(1):3. doi:10.1186/s40348-023-00157-3.

8. Burghardt T, Hochapfel F, Salecker B, Meese C, Gröne H-J, Rachel R, et al. Advanced electron microscopic techniques provide a deeper insight into the peculiar features of podocytes. *Am J Physiol Renal Physiol.* 2015;309(12):F1082-9. doi:10.1152/ajprenal.00338.2015.

9. Ebefors K, Lassen E, Anandakrishnan N, Azeloglu EU, Daehn IS. Modeling the Glomerular Filtration Barrier and Intercellular Crosstalk. *Front Physiol.* 2021;12:689083. doi:10.3389/fphys.2021.689083.

10. Garg P. A Review of Podocyte Biology. *Am J Nephrol.* 2018;47 (Suppl 1):3-13. doi:10.1159/000481633.

11. Friedrich C, Endlich N, Kriz W, Endlich K. Podocytes are sensitive to fluid shear stress *in vitro*. *Am J Physiol Renal Physiol.* 2006;291(4):F856-65. doi:10.1152/ajprenal.00196.2005.

12. Lu CC, Wang GH, Lu J, Chen PP, Zhang Y, Hu ZB, et al. Role of Podocyte Injury in Glomerulosclerosis. *Adv Exp Med Biol.* 2019;1165:195-232. doi:10.1007/978-981-13-8871-2_10.

13. Bierzynska A, Soderquest K, Koziell A. Genes and podocytes - new insights into mechanisms of podocytopathy. *Front Endocrinol (Lausanne).* 2015;5:226. doi:10.3389/fendo.2014.00226.

14. Lasagni L, Lazzeri E, Shankland SJ, Anders HJ, Romagnani P. Podocyte mitosis - a catastrophe. *Curr Mol Med.* 2013;13(1):13-23. doi:10.2174/1566524011307010013.

15. Kopp JB, Anders H-J, Susztak K, Podestà MA, Remuzzi G, Hildebrandt F, et al. Podocytopathies. *Nat Rev Dis Primers.* 2020;6(1):68. doi:10.1038/s41572-020-0196-7.

16. Rabelink TJ, Heerspink HJL, de Zeeuw D. The pathophysiology of proteinuria. In: *Chronic renal disease*. Elsevier; 2015. p. 92-105. doi:10.1016/B978-0-12-411602-3.00009-3.

17. Miao J, Krisanapan P, Tangpanithandee S, Thongprayoon C, Mao MA, Cheungpasitporn W. Efficacy of extracorporeal plasma therapy for adult native kidney patients with Primary FSGS: a Systematic review. *Ren Fail.* 2023;45(1):2176694. doi:10.1080/0886022X.2023.2176694.

18. de Cos M, Meliambro K, Campbell KN. Novel Treatment Paradigms: Focal Segmental Glomerulosclerosis. *Kidney Int Rep.* 2023;8(1):30-5. doi:10.1016/j.ekir.2022.10.004.

19. Focal Segmental Glomerulosclerosis. *StatPearls* [Internet]. Treasure Island (FL): StatPearls Publishing; 2023.

20. Suresh V, Stillman IE, Campbell KN, Meliambro K. Focal Segmental Glomerulosclerosis. *Adv Kidney Dis Health.* 2024;31(4):275-89. doi:10.1053/j.akdh.2024.03.009.

21. Salfi G, Casiraghi F, Remuzzi G. Current understanding of the molecular mechanisms of circulating permeability factor in focal segmental glomerulosclerosis. *Front Immunol.* 2023;14:1247606. doi:10.3389/fimmu.2023.1247606.

22. Beckwith H, Lightstone L, McAdoo S. Sex and gender in glomerular disease. *Semin Nephrol.* 2022; 42(2): 185-96. doi:10.1016/j.semnephrol.2022.04.008.

23. Kitiyakara C, Eggers P, Kopp JB. Twenty-one-year trend in ESRD due to focal segmental glomerulosclerosis in the United States. *Am J Kidney Dis.* 2004;44(5):815-25. doi:10.1053/j.ajkd.2004.07.008.

24. Moeller M, Kramann R, Lammers T, Hoppe B, Latz E, Ludwig-Portugall I, et al. New aspects of kidney fibrosis-from mechanisms of injury to modulation of disease. *Front Med.* 2021;8:814497. doi:10.3389/fmed.2021.814497.

25. Miesen L, Steenbergen E, Smeets B. Parietal cells-new perspectives in glomerular disease. *Cell Tissue Res.* 2017;369(1):237-44. doi:10.1007/s00441-017-2600-5.

26. Jiang S, Luo M, Bai X, Nie P, Zhu Y, Cai H, et al. Cellular crosstalk of glomerular endothelial cells and podocytes in diabetic kidney disease. *J Cell Commun Signal.* 2022;16(3):313-31. doi:10.1007/s12079-021-00664-w.

27. Ravaglia F, Melica ME, Angelotti ML, De Chiara L, Romagnani P, Lasagni L. The Pathology Lesion Patterns of Podocytopathies: How and why? *Front Cell Dev Biol.* 2022;10:838272. doi:10.3389/fcell.2022.838272.

28. Gipson DS, Wang CS, Salmon E, Gbadegesin R, Naik A, Sanna-Cherchi S, et al. FSGS Recurrence Collaboration: Report of a Symposium. *Glomerular Dis.* 2024;4(1):1-10. doi:10.1159/000535138.

29. Fisher M, Ross M, DiFranza L, Reidy K. An Update on Viral Infection-Associated Collapsing Glomerulopathy. *Adv Kidney Dis Health.* 2024;31(4):317-25. doi:10.1053/j.akdh.2023.12.007.

30. De Vriese AS, Sethi S, Nath KA, Glassock RJ, Fervenza FC. Differentiating Primary, Genetic, and Secondary FSGS in Adults: A Clinicopathologic Approach. *J Am Soc Nephrol.* 2018;29(3):759-74. doi:10.1681/ASN.2017090958.

31. Catanese L, Siwy J, Wendt R, Amann K, Beige J, Hendry B, et al. Differentiating primary and secondary FSGS using non-invasive urine biomarkers. *Clin Kidney J.* 2024;17(2):sfad296. doi:10.1093/ckj/sfad296.

32. Bonilla M, Efe O, Selvaskandan H, Lerma EV, Wiegley N. A Review of Focal Segmental Glomerulosclerosis Classification With a Focus on Genetic Associations. *Kidney Med.* 2024;6(6):100826. doi:10.1016/j.xkme.2024.100826.

33. Sambharia M, Rastogi P, Thomas CP. Monogenic focal segmental glomerulosclerosis: a conceptual framework for identification and management of a heterogeneous disease. *Am J Med Genet C Semin Med Genet.* 2022;190(3):377-98. doi:10.1002/ajmg.c.31990.

34. D'Agati V. Pathologic classification of focal segmental glomerulosclerosis. Semin Nephrol. 2003;23(2):117-34. doi:10.1053/snep.2003.50012.

35. Hodson EM, Sinha A, Cooper TE. Interventions for focal segmental glomerulosclerosis in adults. *Cochrane Database Syst Rev.* 2022;2(2):CD003233. doi:10.1002/14651858.CD003233.pub3.

36. Trachtman H. Emerging drugs for treatment of focal segmental glomerulosclerosis. *Expert Opin Emerg Drugs.* 2020;25(3):367-75. doi:10.1080/14728214.2020.1803276.

37. Ahn W, Bomback AS. Approach to Diagnosis and Management of Primary Glomerular Diseases Due to Podocytopathies in Adults: Core Curriculum 2020. *Am J Kidney Dis.* 2020;75(6):955-64. doi:10.1053/j.ajkd.2019.12.019.

38. Rovin BH, Adler SG, Barratt J, Bridoux F, Burdge KA, Chan TM, et al. Kdigo 2021 Clinical Practice Guideline for the Management of Glomerular Diseases. *Kidney Int.* 2021;100(4):S1-S276. doi:10.1016/j.kint.2021.05.021.

39. De Vriese AS, Wetzels JF, Glassock RJ, Sethi S, Fervenza FC. Therapeutic trials in adult FSGS: lessons learned and the road forward. *Nat Rev Nephrol.* 2021;17(9):619-30. doi:10.1038/s41581-021-00427-1.

40. Beaudreuil S, Lorenzo HK, Elias M, Nnang Obada E, Charpentier B, Durrbach A. Optimal management of primary focal segmental glomerulosclerosis in adults. *Int J Nephrol Renovasc Dis.* 2017;10:97-107. doi:10.2147/IJNRD.S126844.

41. Bakris GL. Slowing nephropathy progression: focus on proteinuria reduction. *Clin J Am Soc Nephrol.* 2008;3 Suppl 1(Suppl 1):S3-10. doi:10.2215/CJN.03250807.

42. Shabaka A, Tato Ribera A, Fernandez-Juarez G. Focal Segmental Glomerulosclerosis: State-of-the-Art and Clinical Perspective. *Nephron.* 2020;144(9):413-27. doi:10.1159/000508099.

43. Fogo AB. Animal models of FSGS: lessons for pathogenesis and treatment. *Semin Nephrol*. 2003;23(2):161-71. doi:10.1053/snep.2003.50015.

44. Yang JW, Dettmar AK, Kronbichler A, Gee HY, Saleem M, Kim SH, et al. Recent advances of animal model of focal segmental glomerulosclerosis. *Clin Exp Nephrol.* 2018;22(4):752-63. doi:10.1007/s10157-018-1552-8.

45. de Mik SM, Hoogduijn MJ, de Bruin RW, Dor FJ. Pathophysiology and treatment of focal segmental glomerulosclerosis: the role of animal models. *BMC Nephrol.* 2013;14(1):74. doi:10.1186/1471-2369-14-74.

46. Lee VW, Harris DC. Adriamycin nephropathy: a model of focal segmental glomerulosclerosis. *Nephrology (Carlton).* 2011;16(1):30-8. doi:10.1111/j.1440-1797.2010.01383.x.

47. Kollias G, Evans DJ, Ritter M, Beech J, Morris R, Grosveld F. Ectopic expression of Thy-1 in the kidneys of transgenic mice induces functional and proliferative abnormalities. *Cell.* 1987;51(1):21-31. doi:10.1016/0092-8674(87)90006-7.

48. Assmann KJ, van Son JP, Dijkman HB, Mentzel S, Wetzels JF. Antibody-induced *albuminuria and accelerated focal glomerulosclerosis in the Thy-1.1 transgenic mouse. Kidney Int.* 2002;62(1):116-26. doi:10.1046/j.1523-1755.2002.00428.x.

49. Yang X, Ren X, Li B, Zhai W. Comparative analysis of adriamycin-induced models of focal segmental glomerulosclerosis nephropathy in rats. *Research Square* [preprint]. 2024. doi:10.21203/rs.3.rs-4015976/v1.

50. Le Berre L, Herve C, Buzelin F, Usal C, Soulillou JP, Dantal J. Renal macrophage activation and Th2 polarization precedes the development of nephrotic syndrome in Buffalo/Mna rats. *Kidney Int.* 2005;68(5):2079-90. doi:10.1111/j.1523-1755.2005.00664.x.

51. Fassi A, Sangalli F, Maffi R, Colombi F, Mohamed EI, Brenner BM, et al. Progressive glomerular injury in the MWF rat is predicted by inborn nephron deficit. *J Am Soc Nephrol.* 1998;9(8):1399-406. doi:10.1681/ASN.V981399.

52. Mans BJ, Anantharaman V, Aravind L, Koonin EV. Comparative genomics, evolution and origins of the nuclear envelope and nuclear pore complex. *Cell Cycle.* 2004;3(12):1612-37. doi:10.4161/cc.3.12.1316.

53. Wilson KL, Dawson SC. Evolution: functional evolution of nuclear structure. *J Cell Biol.* 2011;195(2):171-81. doi:10.1083/jcb.201103171.

54. Park N, Katikaneni P, Skern T, Gustin KE. Differential targeting of nuclear pore complex proteins in poliovirus-infected cells. *J Virol*. 2008;82(4):1647-55. doi:10.1128/jvi.01670-07.

55. Schuller AP, Wojtynek M, Mankus D, Tatli M, Kronenberg-Tenga R, Regmi SG, et al. The cellular environment shapes the nuclear pore complex architecture. *Nature.* 2021;598(7882):667-71. doi:10.1038/s41586-021-03985-3.

56. Petrovic S, Samanta D, Perriches T, Bley CJ, Thierbach K, Brown B, et al. Architecture of the linker-scaffold in the nuclear pore. *Science.* 2022;376(6598):eabm9798. doi:10.1126/science.abm9798.

57. Kabachinski G, Schwartz TU. The nuclear pore complex--structure and function at a glance. *J Cell Sci.* 2015;128(3):423-9. doi:10.1242/jcs.083246.

58. Hamed M, Antonin W. Dunking into the Lipid Bilayer: How Direct Membrane Binding of Nucleoporins Can Contribute to Nuclear Pore Complex Structure and Assembly. *Cells.* 2021;10(12):3601. doi:10.3390/cells10123601.

59. Raices M, D'Angelo MA. Nuclear pore complexes and regulation of gene expression. *Curr Opin Cell Biol.* 2017;46:26-32. doi:10.1016/j.ceb.2016.12.006.

60. Beck M, Hurt E. The nuclear pore complex: understanding its function through structural insight. *Nat Rev Mol Cell Biol.* 2017;18(2):73-89. doi:10.1038/nrm.2016.147.

61. Gomar-Alba M, Pozharskaia V, Cichocki B, Schaal C, Kumar A, Jacquel B, et al. Nuclear pore complex acetylation regulates mRNA export and cell cycle commitment in budding yeast. *EMBO J.* 2022;41(15):e110271. doi:10.15252/embj.2021110271.

62. Patel VP, Chu CT. Nuclear transport, oxidative stress, and neurodegeneration. *Int J Clin Exp Pathol.* 2011;4(3):215-29.

63. Folz H, Nino CA, Taranum S, Caesar S, Latta L, Waharte F, et al. SUMOylation of the nuclear pore complex basket is involved in sensing cellular stresses. *J Cell Sci.* 2019;132(7):jcs224279. doi:10.1242/jcs.224279.

64. Liu S, Pellman D. The coordination of nuclear envelope assembly and chromosome segregation in metazoans. *Nucleus.* 2020;11(1):35-52. doi:10.1080/19491034.2020.1742064.

65. Guttinger S, Laurell E, Kutay U. Orchestrating nuclear envelope disassembly and reassembly during mitosis. *Nat Rev Mol Cell Biol.* 2009;10(3):178-91. doi:10.1038/nrm2641.

66. Kutay U, Juhlen R, Antonin W. Mitotic disassembly and reassembly of nuclear pore complexes. *Trends Cell Biol.* 2021;31(12):1019-33. doi:10.1016/j.tcb.2021.06.011.

67. Otsuka S, Steyer AM, Schorb M, Heriche JK, Hossain MJ, Sethi S, et al. Postmitotic nuclear pore assembly proceeds by radial dilation of small membrane openings. *Nat Struct Mol Biol.* 2018;25(1):21-8. doi:10.1038/s41594-017-0001-9.

68. Chou YY, Upadhyayula S, Houser J, He K, Skillern W, Scanavachi G, et al. Inherited nuclear pore substructures template post-mitotic pore assembly. *Dev Cell.* 2021;56(12):1786-803. e9. doi:10.1016/j.devcel.2021.05.015.

69. Rabut G, Doye V, Ellenberg J. Mapping the dynamic organization of the nuclear pore complex inside single living cells. *Nat Cell Biol.* 2004;6(11):1114-21. doi:10.1038/ncb1184.

70. Knockenhauer KE, Schwartz TU. The Nuclear Pore Complex as a Flexible and Dynamic Gate. *Cell.* 2016;164(6):1162-71. doi:10.1016/j.cell.2016.01.034.

71. Rempel IL, Crane MM, Thaller DJ, Mishra A, Jansen DP, Janssens G, et al. Age-dependent deterioration of nuclear pore assembly in mitotic cells decreases transport dynamics. *Elife.* 2019;8:e48186. doi:10.7554/eLife.48186.

72. Janssens GE, Meinema AC, Gonzalez J, Wolters JC, Schmidt A, Guryev V, et al. Protein biogenesis machinery is a driver of replicative aging in yeast. *Elife.* 2015;4:e08527. doi:10.7554/eLife.08527.

73. Rempel IL, Steen A, Veenhoff LM. Poor old pores-The challenge of making and maintaining nuclear pore complexes in aging. *FEBS J.* 2020;287(6):1058-75. doi:10.1111/febs.15205.

74. D'Angelo MA, Raices M, Panowski SH, Hetzer MW. Age-dependent deterioration of nuclear pore complexes causes a loss of nuclear integrity in postmitotic cells. *Cell.* 2009;136(2):284-95. doi:10.1016/j.cell.2008.11.037.

75. Sakuma S, D'Angelo MA. The roles of the nuclear pore complex in cellular dysfunction, aging and disease. *Semin Cell Dev Biol*. 2017;68:72-84. doi:10.1016/j.semcdb.2017.05.006.

76. Coyne AN, Rothstein JD. Nuclear pore complexes - a doorway to neural injury in neurodegeneration. *Nat Rev Neurol.* 2022;18(6):348-62. doi:10.1038/s41582-022-00653-6.

77. Lupu F, Alves A, Anderson K, Doye V, Lacy E. Nuclear pore composition regulates neural stem/progenitor cell differentiation in the mouse embryo. *Dev Cell.* 2008;14(6):831-42. doi:10.1016/j.devcel.2008.03.011.

78. Li C, Goryaynov A, Yang W. The selective permeability barrier in the nuclear pore complex. *Nucleus.* 2016;7(5):430-46. doi:10.1080/19491034.2016.1238997.

79. Xu S, Powers MA. Nuclear pore proteins and cancer. *Semin Cell Dev Biol*. 2009;20(5):620-630. doi:10.1016/j.semcdb.2009.03.003.

80. Gould VE, Orucevic A, Zentgraf H, Gattuso P, Martinez N, Alonso A. Nup88 (karyoporin) in human malignant neoplasms and dysplasias: correlations of immunostaining of tissue sections, cytologic smears, and immunoblot analysis. *Hum Pathol.* 2002;33(5):536-44. doi:10.1053/hupa.2002.124785.

81. Agudo D, Gomez-Esquer F, Martinez-Arribas F, Nunez-Villar MJ, Pollan M, Schneider J. Nup88 mRNA overexpression is associated with high aggressiveness of breast cancer. *Int J Cancer.* 2004;109(5):717-20. doi:10.1002/ijc.20034.

82. Varambally S, Yu J, Laxman B, Rhodes DR, Mehra R, Tomlins SA, et al. Integrative genomic and proteomic analysis of prostate cancer reveals signatures of metastatic progression. *Cancer Cell.* 2005;8(5):393-406. doi:10.1016/j.ccr.2005.10.001.

83. Nofrini V, Di Giacomo D, Mecucci C. Nucleoporin genes in human diseases. *Eur J Hum Genet.* 2016;24(10):1388-95. doi:10.1038/ejhg.2016.25.

84. Tsuji S, Midorikawa Y, Seki M, Takayama T, Sugiyama Y, Aburatani H. Network-based analysis for identification of candidate genes for colorectal cancer progression. *Biochem Biophys Res Commun.* 2016;476(4):534-40. doi:10.1016/j.bbrc.2016.05.158.

85. Syed YY. Selinexor: First Global Approval. *Drugs.* 2019;79(13):1485-94. doi:10.1007/s40265-019-01188-9.

86. Azmi AS, Uddin MH, Mohammad RM. The nuclear export protein XPO1 - from biology to targeted therapy. *Nat Rev Clin Oncol.* 2021;18(3):152-69. doi:10.1038/s41571-020-00442-4.

87. Galinski B, Alexander TB, Mitchell DA, Chatwin HV, Awah C, Green AL, et al. Therapeutic Targeting of Exportin-1 in Childhood Cancer. *Cancers (Basel).* 2021;13(24):6161. doi:10.3390/cancers13246161.

88. Kashyap T, Argueta C, Aboukameel A, Unger TJ, Klebanov B, Mohammad RM, et al. Selinexor, a Selective Inhibitor of Nuclear Export (SINE) compound, acts through NF-kappaB deactivation and combines with proteasome inhibitors to synergistically

induce tumor cell death. *Oncotarget.* 2016;7(48):78883-95. doi:10.18632/oncotarget.12428.

89. Coleman RL, Kalyanapu P, Walker CJ, Vergote I. An evaluation of selinexor as a maintenance therapy for patients with p53 wild-type, advanced, or recurrent endometrial carcinoma. *Expert Rev Anticancer Ther.* 2025;25(9):1007-19. doi:10.1080/14737140.2025.2522948.

90. Mascarenhas J, Maher K, Rampal R, Bose P, Podoltsev N, Hong J, et al. Selinexor plus ruxolitinib in JAK inhibitor treatment-naive myelofibrosis: SENTRY Phase 3 study design. *Future Oncol.* 2025;21(7):807-13. doi:10.1080/14796694.2025.2461393.

91. Lussignol M, Kopp M, Molloy K, Vizcay-Barrena G, Fleck RA, Dorner M, et al. Proteomics of HCV virions reveals an essential role for the nucleoporin Nup98 in virus morphogenesis. *Proc Natl Acad Sci USA.* 2016;113(9):2484-9. doi:10.1073/pnas.1518934113.

92. Le Rouzic E, Mousnier A, Rustum C, Stutz F, Hallberg E, Dargemont C, et al. Docking of HIV-1 Vpr to the nuclear envelope is mediated by the interaction with the nucleoporin hCG1. *J Biol Chem.* 2002;277(47):45091-8. doi:10.1074/jbc.M207439200.

93. Bejarano DA, Peng K, Laketa V, Borner K, Jost KL, Lucic B, et al. HIV-1 nuclear import in macrophages is regulated by CPSF6-capsid interactions at the nuclear pore complex. *Elife.* 2019;8:e41800. doi:10.7554/eLife.41800.

94. Buffone C, Martinez-Lopez A, Fricke T, Opp S, Severgnini M, Cifola I, et al. Nup153 Unlocks the Nuclear Pore Complex for HIV-1 Nuclear Translocation in Nondividing Cells. *J Virol.* 2018;92(19): 10-128. doi:10.1128/JVI.00648-18.

95. Yao L, Li Y, Wang P, Xu C, Yu Z. Nucleoporin-associated steroid-resistant nephrotic syndrome. *Pediatr Nephrol.* 2025;40(3):629-49. doi:10.1007/s00467-024-06494-3.

96. Miyake N, Tsukaguchi H, Koshimizu E, Shono A, Matsunaga S, Shiina M, et al. Biallelic Mutations in Nuclear Pore Complex Subunit NUP107 Cause Early-Childhood-Onset Steroid-Resistant Nephrotic Syndrome. *Am J Hum Genet.* 2015;97(4):555-66. doi:10.1016/j.ajhg.2015.08.013.

97. Braun DA, Sadowski CE, Kohl S, Lovric S, Astrinidis SA, Pabst WL, et al. Mutations in nuclear pore genes NUP93, NUP205 and XPO5 cause steroid-resistant nephrotic syndrome. *Nat Genet.* 2016;48(4):457-65. doi:10.1038/ng.3512.

98. Hussain HMJ, Cai Y, Weng Q, Tong J, Aftab A, Jin Y, et al. Mutation in XPO5 causes adult-onset autosomal dominant familial focal segmental glomerulosclerosis. *Hum Genomics.* 2022;16(1):57. doi:10.1186/s40246-022-00430-y.

99. Braun DA, Lovric S, Schapiro D, Schneider R, Marquez J, Asif M, et al. Mutations in multiple components of the nuclear pore complex cause nephrotic syndrome. *J Clin Invest.* 2018;128(10):4313-28. doi:10.1172/JCI98688.

100. Hashimoto T, Harita Y, Takizawa K, Urae S, Ishizuka K, Miura K, et al. *In Vivo* Expression of NUP93 and Its Alteration by NUP93 Mutations Causing Focal Segmental Glomerulosclerosis. *Kidney Int Rep.* 2019;4(9):1312-22. doi:10.1016/j.ekir.2019.05.1157.

101. Zhao F, Zhu J-y, Richman A, Fu Y, Huang W, Chen N, et al. Mutations in NUP160 are implicated in steroid-resistant nephrotic syndrome. *J Am Soc Nephrol.* 2019;30(5):840-53. doi:10.1681/ASN.2018080786.

102. Han Y, Sha H, Yang Y, Yu Z, Zhou L, Wang Y, et al. Mutations in the NUP93, NUP107 and NUP160 genes cause steroid-resistant nephrotic syndrome in Chinese children. *Ital J Pediatr.* 2024;50(1):81. doi:10.1186/s13052-024-01656-3.

103. Zhao B, Chen JY, Liao YB, Li YF, Jiang XM, Bi X, et al. Steroid-resistant nephrotic syndrome in infants caused by a novel compound heterozygous mutation of the NUP93: A CARE case report. *Medicine (Baltimore).* 2021;100(6):e24627. doi:10.1097/MD.0000000000024627.

104. Acharya R, Upadhyay K. End-stage renal disease in a child with focal segmental glomerulosclerosis associated with a homozygous NUP93 variant. *Clin Case Rep.* 2021;9(11):e05111. doi:10.1002/ccr3.5111.

105. Ester L, Cabrita I, Ventzke M, Christodoulou M, Fabretti F, Benzing T, et al. The FSGS disease gene product and nuclear pore protein NUP205 regulates nuclear localization and activity of the transcriptional regulators YAP and TAZ in podocytes. *bioRxiv*. 2023. doi:10.1101/2023.03.07.531564.

106. Lipska-Zietkiewicz BS, Schaefer F. NUP Nephropathy: When Defective Pores Cause Leaky Glomeruli. *Am J Kidney Dis.* 2019;73(6):890-2. doi:10.1053/j.ajkd.2019.01.015.

107. Englmeier L, Olivo JC, Mattaj IW. Receptor-mediated substrate translocation through the nuclear pore complex without nucleotide triphosphate hydrolysis. *Curr Biol.* 1999;9(1):30-41. doi:10.1016/s0960-9822(99)80044-x.

108. Frahsek M, Schulte K, Chia-Gil A, Djudjaj S, Schueler H, Leuchtle K, et al. Cre recombinase toxicity in podocytes: a novel genetic model for FSGS in adolescent mice. *Am J Physiol Renal Physiol.* 2019 Nov 1;317(5):F1375-82. doi:10.1152/ajprenal.00573.2018.

109. Boerries M, Grahammer F, Eiselein S, Buck M, Meyer C, Goedel M, et al. Molecular fingerprinting of the podocyte reveals novel gene and protein regulatory networks. *Kidney Int.* 2013;83(6):1052-64. doi:10.1038/ki.2012.487.

110. Wang H, Sheng J, He H, Chen X, Li J, Tan R, et al. A simple and highly purified method for isolation of glomeruli from the mouse kidney. *Am J Physiol Renal Physiol.* 2019;317(5):F1217-F23. doi:10.1152/ajprenal.00293.2019.

111. Herlan L, Unland J, Langer S, Schulte L, Schutten S, Garcia-Prieto CF, et al. Development of progressive albuminuria in male Munich Wistar Fromter rats is androgen dependent. *Physiol Genomics.* 2015;47(7):281-9. doi:10.1152/physiolgenomics.00008.2015.

112. Floege J, Johnson RJ, Gordon K, Iida H, Pritzl P, Yoshimura A, et al. Increased synthesis of extracellular matrix in mesangial proliferative nephritis. *Kidney Int.* 1991;40(3):477-88. doi:10.1038/ki.1991.235.

113. Kliem V, Johnson RJ, Alpers CE, Yoshimura A, Couser WG, Koch KM, et al. Mechanisms involved in the pathogenesis of tubulointerstitial fibrosis in 5/6-nephrectomized rats. *Kidney Int.* 1996;49(3):666-78. doi:10.1038/ki.1996.95.

114. Kamentsky L, Jones TR, Fraser A, Bray MA, Logan DJ, Madden KL, et al. Improved structure, function and compatibility for CellProfiler: modular high-throughput image analysis software. *Bioinformatics.* 2011;27(8):1179-80. doi:10.1093/bioinformatics/btr095.

115. Schneider RR, Eng DG, Kutz JN, Sweetwyne MT, Pippin JW, Shankland SJ. Compound effects of aging and experimental FSGS on glomerular epithelial cells. *Aging (Albany NY).* 2017;9(2):524. doi:10.18632/aging.101176.

116. Verzola D, Saio M, Picciotto D, Viazzi F, Russo E, Cipriani L, et al. Cellular senescence is associated with faster progression of focal segmental glomerulosclerosis. *Am J Nephrol.* 2021;51(12):950-8. doi:10.1159/000511560.

117. Ozeki T, Nagata M, Katsuno T, Inagaki K, Goto K, Kato S, et al. Nephrotic syndrome with focal segmental glomerular lesions unclassified by Columbia classification; Pathology and clinical implication. *PLoS One.* 2021;16(1):e0244677. doi:10.1371/journal.pone.0244677.

118. Jung J, Behrends C. Multifaceted role of SMCR8 as autophagy regulator. *Small GTPases.* 2020;11(1):53-61. doi:10.1080/21541248.2017.1346553.

119. Goodier JL, Soares AO, Pereira GC, DeVine LR, Sanchez L, Cole RN, et al. C9orf72-associated SMCR8 protein binds in the ubiquitin pathway and with proteins linked with neurological disease. *Acta Neuropathol Commun.* 2020;8(1):110. doi:10.1074/jbc.M110.122929.

120. Amick J, Tharkeshwar AK, Talaia G, Ferguson SM. PQLC2 recruits the C9orf72 complex to lysosomes in response to cationic amino acid starvation. *J Cell Biol.* 2020;219(1):e201906076. doi:10.1083/jcb.201906076.

121. Gorlich D, Kutay U. Transport between the cell nucleus and the cytoplasm. Annu *Rev Cell Dev Biol.* 1999;15(1):607-60. doi:10.1146/annurev.cellbio.15.1.607.

122. Kalab P, Heald R. The RanGTP gradient - a GPS for the mitotic spindle. *J Cell Sci.* 2008;121(Pt 10):1577-86. doi:10.1242/jcs.005959.

123. Kelley JB, Datta S, Snow CJ, Chatterjee M, Ni L, Spencer A, et al. The defective nuclear lamina in Hutchinson-gilford progeria syndrome disrupts the nucleocytoplasmic Ran gradient and inhibits nuclear localization of Ubc9. *Mol Cell Biol.* 2011;31(16):3378-95. doi:10.1128/MCB.05087-11.

124. Rong L, Livingstone M, Sukarieh R, Petroulakis E, Gingras AC, Crosby K, et al. Control of eIF4E cellular localization by eIF4E-binding proteins, 4E-BPs. *RNA.* 2008;14(7):1318-27. doi:10.1261/rna.950608.

125. Dang T, Jang SH, Back SH, Park JW, Han IS. DRG2 Deficiency Causes Impaired Microtubule Dynamics in HeLa Cells. *Mol Cells.* 2018;41(12):1045-51. doi:10.14348/molcells.2018.0129.

126. Mani M, Lee UH, Yoon NA, Yoon EH, Lee BJ, Cho WJ, et al. Developmentally regulated GTP-binding protein 2 is required for stabilization of Rac1-positive membrane tubules. *Biochem Biophys Res Commun.* 2017;493(1):758-64. doi:10.1016/j.bbrc.2017.08.110.

127. Smeets B, Kabgani N, Moeller MJ. Isolation and primary culture of murine podocytes with proven origin. In: *Kidney Research: Experimental Protocols.* New York: Springer; 2015. p. 3-10. doi:10.1007/978-1-4939-3353-2_1.

128. Signes A, Fernandez-Vizarra E. Assembly of mammalian oxidative phosphorylation complexes I–V and supercomplexes. *Essays Biochem.* 2018;62(3):255-70. doi:10.1042/EBC20170098.

129. Piekutowska-Abramczuk D, Assouline Z, Mataković L, Feichtinger RG, Koňařiková E, Jurkiewicz E, et al. NDUFB8 mutations cause mitochondrial complex I deficiency in individuals with Leigh-like encephalomyopathy. *Am J Hum Genet.* 2018;102(3):460-7. doi:10.1016/j.ajhg.2018.01.008.

130. Romero-Carramiñana I, Dominguez-Zorita S, Esparza-Moltó PB, Cuezva JM. Ablation of Atp5if1 impairs metabolic reprogramming and proliferation of T lymphocytes and compromises mouse survival. *iScience.* 2024;27(6). doi:10.1016/j.isci.2024.109863.

131. Janer A, Van Karnebeek CD, Sasarman F, Antonicka H, Al Ghamdi M, Shyr C, et al. RMND1 deficiency associated with neonatal lactic acidosis, infantile onset renal failure, deafness, and multiorgan involvement. *Eur J Hum Genet.* 2015;23(10):1301-7. doi:10.1038/ejhg.2014.293.

132. Akram S, Zittlau KI, Maček B, Jansen R-P. Proximity labeling reveals differential interaction partners of the human mitochondrial import receptor proteins TOMM20 and TOMM70. *bioRxiv.* 2024. doi:10.1101/2024.10.25.620316.

133. Otera H, Wang C, Cleland MM, Setoguchi K, Yokota S, Youle RJ, et al. Mff is an essential factor for mitochondrial recruitment of Drp1 during mitochondrial fission in mammalian cells. *J Cell Biol.* 2010;191(6):1141-58. doi:10.1083/jcb.201007152.

134. Seager R, Ramesh NS, Cross S, Guo C, Wilkinson KA, Henley JM. SUMOylation of MFF coordinates fission complexes to promote stress-induced mitochondrial fragmentation. *Sci Adv*. 2024;10(40):eadq6223. doi:10.1126/sciadv.adq6223.

135. Shoshan-Barmatz V, Shteinfer-Kuzmine A, Verma A. VDAC1 at the intersection of cell metabolism, apoptosis, and diseases. *Biomolecules.* 2020;10(11):1485. doi:10.3390/biom10111485.

136. Dubey AK, Godbole A, Mathew M. Regulation of VDAC trafficking modulates cell death. *Cell Death Discov.* 2016;2(1):1-10. doi:10.1038/cddiscovery.2016.85.

137. Liu JC, Liu J, Holmström KM, Menazza S, Parks RJ, Fergusson MM, et al. MICU1 serves as a molecular gatekeeper to prevent *in vivo* mitochondrial calcium overload. *Cell Rep.* 2016;16(6):1561-73. doi:10.1016/j.celrep.2016.07.011.

138. Joseph A, Chen H, Anagnostopoulos G, Montégut L, Lafarge A, Motiño O, et al. Effects of acyl-coenzyme A binding protein (ACBP)/diazepam-binding inhibitor (DBI) on body mass index. *Cell Death Dis.* 2021;12(6):599. doi:10.1038/s41419-021-03864-9.

139. Jin L, Chun J, Pan C, Alesi G, Li D, Magliocca K, et al. Phosphorylation-mediated activation of LDHA promotes cancer cell invasion and tumour metastasis. *Oncogene.* 2017;36(27):3797-806. doi:10.1038/onc.2017.6.

140. Xiong Y, Lei Q, Zhao S, Guan K. Regulation of glycolysis and gluconeogenesis by acetylation of PKM and PEPCK. *Cold Spring Harb Symp Quant Biol.* 2011;76:285-9. doi:10.1101/sqb.2011.76.010942.

141. Tang F, Cui Q. Diverse roles of aldolase enzymes in cancer development, drug resistance and therapeutic approaches as moonlighting enzymes. *Med Oncol.* 2024;41(9):224. doi:10.1007/s12032-024-02470-x.

142. Brocker C, Lassen N, Estey T, Pappa A, Cantore M, Orlova VV, et al. Aldehyde dehydrogenase 7A1 (ALDH7A1) is a novel enzyme involved in cellular defense against hyperosmotic stress. *J Biol Chem.* 2010;285(24):18452-63. doi:10.1074/jbc.M109.077925.

143. Strik MC, Wolbink A, Wouters D, Bladergroen BA, Verlaan AR, van Houdt IS, et al. Intracellular serpin SERPINB6 (PI6) is abundantly expressed by human mast cells

and forms complexes with β-tryptase monomers. *Blood.* 2004;103(7):2710-7. doi:10.1182/blood-2003-08-2981.

144. Jang M, Hara S, Kim G-H, Kim SM, Son S, Kwon M, et al. Dutomycin induces autophagy and apoptosis by targeting the serine protease inhibitor SERPINB6. *ACS Chem. Biol.* 2021;16(2):360-70. doi:10.1021/acschembio.0c00889.

145. Liu Y, Xiao W, Shinde M, Field J, Templeton DM. Cadmium favors F-actin depolymerization in rat renal mesangial cells by site-specific, disulfide-based dimerization of the CAP1 protein. *Arch Toxicol.* 2018;92(3):1049-64. doi:10.1007/s00204-017-2142-3.

146. Garg P, Verma R, Cook L, Soofi A, Venkatareddy M, George B, et al. Actin-depolymerizing factor cofilin-1 is necessary in maintaining mature podocyte architecture. *J Biol Chem.* 2010;285(29):22676-88. doi:10.1074/jbc.M110.122929.

147. Su J, Wang L, Guan X, Li N, Sun L. Knocking-down annexin A3 suppresses inflammation, oxidative stress, apoptosis, and endoplasmic reticulum stress to attenuate sepsis-induced acute kidney injury in HK2 cells. *Cytojournal.* 2024;21:75. doi:10.25259/Cytojournal_64_2024.

148. Xiao F, Guan Y, Liu T, Zeng Y, Zhu H, Yang K. Oxalate-upregulated annexin A6 promotes the formation of calcium oxalate kidney stones by exacerbating calcium release-mediated oxidative stress injury in renal tubular epithelial cells and crystal-cell adhesion. *Arch Biochem Biophys.* 2024;761:110187. doi:10.1016/j.abb.2024.110187.

149. Li X, Wang H, Jia A, Cao Y, Yang L, Jia Z. LGALS1 regulates cell adhesion to promote the progression of ovarian cancer. *Oncol Lett.* 2023;26(2):1-11. doi:10.3892/ol.2023.13912.

150. Baek J-H, Kim D-H, Lee J, Kim S-J, Chun K-H. Galectin-1 accelerates high-fat diet-induced obesity by activation of peroxisome proliferator-activated receptor gamma (PPARγ) in mice. *Cell Death Dis.* 2021;12(1):66. doi:10.1038/s41419-020-03367-z.

151. Ajioka RS, Phillips JD, Kushner JP. Biosynthesis of heme in mammals. *Biochim Biophys Acta.* 2006;1763(7):723-36. doi:10.1016/j.bbamcr.2006.05.005.

152. Grandi P, Doye V, Hurt EC. Purification of NSP1 reveals complex formation with 'GLFG' nucleoporins and a novel nuclear pore protein NIC96. *EMBO J.* 1993;12(8):3061-71. doi:10.1002/j.1460-2075.1993.tb05975.x.

153. Sachdev R, Sieverding C, Flotenmeyer M, Antonin W. The C-terminal domain of Nup93 is essential for assembly of the structural backbone of nuclear pore complexes. *Mol Biol Cell.* 2012;23(4):740-9. doi:10.1091/mbc.E11-09-0761.

154. Vollmer B, Antonin W. The diverse roles of the Nup93/Nic96 complex proteins - structural scaffolds of the nuclear pore complex with additional cellular functions. *Biol Chem.* 2014;395(5):515-28. doi:10.1515/hsz-2013-0285.

155. Zanni G, De Magistris P, Nardella M, Bellacchio E, Barresi S, Sferra A, et al. Biallelic variants in the nuclear pore complex protein NUP93 are associated with non-progressive congenital ataxia. *Cerebellum.* 2019;18(3):422-32. doi:10.1007/s12311-019-1010-5.

156. Ribbeck K, Gorlich D. The permeability barrier of nuclear pore complexes appears to operate via hydrophobic exclusion. EMBO J. 2002;21(11):2664-71. doi:10.1093/emboj/21.11.2664.

157. Lain S, Lane D. Improving cancer therapy by non-genotoxic activation of p53. *Eur J Cancer.* 2003;39(8):1053-60. doi:10.1016/s0959-8049(03)00063-7.

158. Newlands ES, Rustin GJ, Brampton MH. Phase I trial of elactocin. *Br J Cancer.* 1996;74(4):648-9. doi:10.1038/bjc.1996.415.

159. Yang Y, Guo L, Chen L, Gong B, Jia D, Sun Q. Nuclear transport proteins: structure, function, and disease relevance. *Signal Transduct Target Ther.* 2023;8(1):425. doi:10.1038/s41392-023-01649-4.

160. Gandhi UH, Senapedis W, Baloglu E, Unger TJ, Chari A, Vogl D, et al. Clinical Implications of Targeting XPO1-mediated Nuclear Export in Multiple Myeloma. *Clin Lymphoma Myeloma Leuk.* 2018;18(5):335-45. doi:10.1016/j.clml.2018.03.003.

161. Gravina GL, Mancini A, Sanita P, Vitale F, Marampon F, Ventura L, et al. KPT-330, a potent and selective exportin-1 (XPO-1) inhibitor, shows antitumor effects modulating the expression of cyclin D1 and survivin [corrected] in prostate cancer models. *BMC Cancer.* 2015;15(1):941. doi:10.1186/s12885-015-1936-z.

162. Turner JG, Dawson J, Cubitt CL, Baz R, Sullivan DM. Inhibition of CRM1-dependent nuclear export sensitizes malignant cells to cytotoxic and targeted agents. *Semin Cancer Biol*. 2014;27:62-73. doi:10.1016/j.semcancer.2014.03.001.

163. Gao Y, Hamed M, Martin IV, Raffetseder U, Liu X, Leitz A, et al. The nuclear export inhibitor selinexor improves kidney function in a rat model of focal segmental glomerulosclerosis. *Am J Physiol Renal Physiol.* 2025;329(4):F496-509. doi:10.1152/ajprenal.00143.2025.

164. Etchin J, Sanda T, Mansour MR, Kentsis A, Montero J, Le BT, et al. KPT-330 inhibitor of CRM1 (XPO1)-mediated nuclear export has selective anti-leukaemic activity in preclinical models of T-cell acute lymphoblastic leukaemia and acute myeloid leukaemia. *Br J Haematol.* 2013;161(1):117-27. doi:10.1111/bjh.12231.

165. Davis LI, Blobel G. Identification and characterization of a nuclear pore complex protein. *Cell.* 1986;45(5):699-709. doi:10.1016/0092-8674(86)90784-1.

166. Toyama BH, Savas JN, Park SK, Harris MS, Ingolia NT, Yates JR, 3rd, et al. Identification of long-lived proteins reveals exceptional stability of essential cellular structures. *Cell.* 2013;154(5):971-82. doi:10.1016/j.cell.2013.07.037.

167. Gravina GL, Senapedis W, McCauley D, Baloglu E, Shacham S, Festuccia C. Nucleo-cytoplasmic transport as a therapeutic target of cancer. *J Hematol Oncol.* 2014;7(1):85. doi:10.1186/s13045-014-0085-1.

168. Hodgin JB, Bitzer M, Wickman L, Afshinnia F, Wang SQ, O'Connor C, et al. Glomerular Aging and Focal Global Glomerulosclerosis: A Podometric Perspective. *J Am Soc Nephrol*. 2015;26(12):3162-78. doi:10.1681/ASN.2014080752.

169. Rule AD, Amer H, Cornell LD, Taler SJ, Cosio FG, Kremers WK, et al. The association between age and nephrosclerosis on renal biopsy among healthy adults. *Ann Intern Med.* 2010;152(9):561-7. doi:10.7326/0003-4819-152-9-201005040-00006.

170. Glassock RJ, Rule AD. The implications of anatomical and functional changes of the aging kidney: with an emphasis on the glomeruli. *Kidney Int.* 2012;82(3):270-7. doi:10.1038/ki.2012.65.

171. Dutta S, Sengupta P. Men and mice: Relating their ages. *Life Sci.* 2016;152:244-8. doi:10.1016/j.lfs.2015.10.025.

172. Floege J, Hackmann B, Kliem V, Kriz W, Alpers CE, Johnson RJ, Kühn KW, Koch KM, Brunkhorst R. Age-related glomerulosclerosis and interstitial fibrosis in Milan normotensive rats: a podocyte disease. *Kidney Int.* 1997 Jan;51(1):230-43. doi:10.1038/ki.1997.28.

173. Kikuchi M, Wickman L, Rabah R, Wiggins RC. Podocyte number and density changes during early human life. *Pediatr Nephrol.* 2017;32(5):823-34. doi:10.1007/s00467-016-3564-5.

174. Venkatareddy M, Wang S, Yang Y, Patel S, Wickman L, Nishizono R, et al. Estimating podocyte number and density using a single histologic section. *J Am Soc Nephrol.* 2014;25(5):1118-29. doi:10.1681/ASN.2013080859.

175. Takemoto M, Asker N, Gerhardt H, Lundkvist A, Johansson BR, Saito Y, et al. A new method for large scale isolation of kidney glomeruli from mice. *Am J Pathol.* 2002;161(3):799-805. doi:10.1016/S0002-9440(10)64239-3.

176. Krtil J, Platenik J, Kazderova M, Tesar V, Zima T. Culture methods of glomerular podocytes. *Kidney Blood Press Res.* 2007;30(3):162-74. doi:10.1159/000102520.

177. Shankland SJ, Wang Y, Shaw AS, Vaughan JC, Pippin JW, Wessely O. Podocyte Aging: Why and How Getting Old Matters. *J Am Soc Nephrol.* 2021;32(11):2697-713. doi:10.1681/ASN.2021050614.

178. Wang Y, Eng DG, Kaverina NV, Loretz CJ, Koirala A, Akilesh S, et al. Global transcriptomic changes occur in aged mouse podocytes. *Kidney Int.* 2020;98(5):1160-73. doi:10.1016/j.kint.2020.05.052.

179. Park SC. Nuclear barrier hypothesis of aging as mechanism for trade-off growth to survival. *Adv Exp Med Biol.* 2011;720:3-13. doi:10.1007/978-1-4614-0254-1_1.

180. Kim SY, Ryu SJ, Ahn HJ, Choi HR, Kang HT, Park SC. Senescence-related functional nuclear barrier by down-regulation of nucleo-cytoplasmic trafficking gene expression. *Biochem Biophys Res Commun.* 2010;391(1):28-32. doi:10.1016/j.bbrc.2009.10.154.

181. Jung J, Nayak A, Schaeffer V, Starzetz T, Kirsch AK, Muller S, et al. Multiplex image-based autophagy RNAi screening identifies SMCR8 as ULK1 kinase activity and gene expression regulator. *Elife.* 2017;6:e23063. doi:10.7554/eLife.23063.

182. Shankland SJ, Rule AD, Kutz JN, Pippin JW, Wessely O. Podocyte Senescence and Aging. *Kidney360.* 2023;4(12):1784-93. doi:10.34067/KID.0000000000000284.

183. Kasinath BS, Mariappan MM, Sataranatarajan K, Lee MJ, Ghosh Choudhury G, Feliers D. Novel mechanisms of protein synthesis in diabetic nephropathy--role of mRNA translation. *Rev Endocr Metab Disord.* 2008;9(4):255-66. doi:10.1007/s11154-008-9091-3.

184. Palmer CS, Anderson AJ, Stojanovski D. Mitochondrial protein import dysfunction: mitochondrial disease, neurodegenerative disease and cancer. *FEBS Lett.* 2021;595(8):1107-31. doi:10.1002/1873-3468.14022.

185. Shakya VP, Barbeau WA, Xiao T, Knutson CS, Schuler MH, Hughes AL. A nuclear-based quality control pathway for non-imported mitochondrial proteins. *elife.* 2021;10:e61230. doi:10.7554/eLife.61230.

186. Wrobel L, Topf U, Bragoszewski P, Wiese S, Sztolsztener ME, Oeljeklaus S, et al. Mistargeted mitochondrial proteins activate a proteostatic response in the cytosol. *Nature*. 2015;524(7566):485-8. doi:10.1038/nature14951.

187. Mårtensson CU, Priesnitz C, Song J, Ellenrieder L, Doan KN, Boos F, et al. Mitochondrial protein translocation-associated degradation. *Nature*. 2019;569(7758):679-83. doi:10.1038/s41586-019-1227-y.

188. Kim KH, Son JM, Benayoun BA, Lee C. The mitochondrial-encoded peptide MOTS-c translocates to the nucleus to regulate nuclear gene expression in response to metabolic stress. *Cell Metab.* 2018;28(3):516-24.e7. doi:10.1016/j.cmet.2018.06.008.

189. Cardamone MD, Tanasa B, Cederquist CT, Huang J, Mahdaviani K, Li W, et al. Mitochondrial retrograde signaling in mammals is mediated by the transcriptional cofactor GPS2 via direct mitochondria-to-nucleus translocation. *Mol Cell.* 2018;69(5):757-72.e7. doi:10.1016/j.molcel.2018.01.037.

190. Monaghan RM, Whitmarsh AJ. Mitochondrial proteins moonlighting in the nucleus. *Trends Biochem Sci.* 2015;40(12):728-35. doi:10.1016/j.tibs.2015.10.003.

191. Sripathi SR, He W, Atkinson CL, Smith JJ, Liu Z, Elledge BM, et al. Mitochondrial–nuclear communication by prohibitin shuttling under oxidative stress. *Biochemistry.* 2011;50(39):8342-51. doi:10.1021/bi2008933.

192. Pfanner N, Warscheid B, Wiedemann N. Mitochondrial proteins: from biogenesis to functional networks. *Nat Rev Mol Cell Biol.* 2019;20(5):267-84. doi:10.1038/s41580-018-0092-0.

193. McBride HM, Neuspiel M, Wasiak S. Mitochondria: more than just a powerhouse. *Curr Biol.* 2006;16(14):R551-R60. doi:10.1016/j.cub.2006.06.054.

194. Wei P, Zhang X, Yan C, Sun S, Chen Z, Lin F. Mitochondrial dysfunction and aging: multidimensional mechanisms and therapeutic strategies. *Biogerontology.* 2025;26(4):142. doi:10.1007/s10522-025-10273-4.

195. Feng Z, Hanson RW, Berger NA, Trubitsyn A. Reprogramming of energy metabolism as a driver of aging. *Oncotarget.* 2016;7(13):15410. doi:10.18632/oncotarget.7645.

196. Lionaki E, Gkikas I, Daskalaki I, Ioannidi M-K, Klapa MI, Tavernarakis N. Mitochondrial protein import determines lifespan through metabolic reprogramming and de novo serine biosynthesis. *Nat Commun*. 2022;13(1):651. doi:10.1038/s41467-022-28272-1.

197. Premchandani T, Taksande J, Tatode A, Sheikh S, Qutub M, Hussain UM, et al. Mitochondrial Dysfunction and Glycolytic Shift in the Tumor Microenvironment: Impact on Paclitaxel Efficacy in Cancer Therapy. *Clin Bioenerg*. 2025;1(1):5. doi:10.3390/clinbioenerg1010005.

198. Daehn IS, Duffield JS. The glomerular filtration barrier: a structural target for novel kidney therapies. *Nat Rev Drug Discov*. 2021;20(10):770-88. doi:10.1038/s41573-021-00242-0.

199. Hu H, Liang W, Ding G. Podocyte metabolic reprogramming and targeted therapy. *J Am Soc Nephrol*. 2024;10-1681. doi:10.1681/ASN.0000000917.

200. Müller-Deile J, Schiffer M. The podocyte power-plant disaster and its contribution to glomerulopathy. *Front Endocrinol*. 2014;5:209. doi:10.3389/fendo.2014.00209.

201. Ahmadian E, Eftekhari A, Atakishizada S, Valiyeva M, Ardalan M, Khalilov R, et

al. Podocytopathy: the role of actin cytoskeleton. *Biomed Pharmacother.* 2022;156:113920. doi:10.1016/j.biopha.2022.113920.

202. Gujarati NA, Vasquez JM, Bogenhagen DF, Mallipattu SK. The complicated role of mitochondria in the podocyte. *Am J Physiol Renal Physiol*. 2020;319(6):F955-F65. doi:10.1152/ajprenal.00393.2020.

203. Imasawa T, Rossignol R. Podocyte energy metabolism and glomerular diseases. *Int J Biochem Cell Biol*. 2013;45(9):2109-18. doi:10.1016/j.biocel.2013.06.013.

204. Etchin J, Montero J, Berezovskaya A, Le B, Kentsis A, Christie A, et al. Activity of a selective inhibitor of nuclear export, selinexor (KPT-330), against AML-initiating cells engrafted into immunosuppressed NSG mice. *Leukemia.* 2016;30(1). doi:10.1038/leu.2015.194.

205. Zhao C, Yang Z-y, Zhang J, Li O, Liu S-l, Cai C, et al. Inhibition of XPO1 with KPT-330 induces autophagy-dependent apoptosis in gallbladder cancer by activating the p53/mTOR pathway. *J Transl Med.* 2022;20(1):434. doi:10.1186/s12967-022-03635-w.

206. Fukuda R, Suico MA, Kai Y, Omachi K, Motomura K, Koga T, et al. Podocyte p53 limits the severity of experimental Alport syndrome. *J Am Soc Nephrol*. 2016;27(1):144-57. doi:10.1681/ASN.2014111109.

207. Meehan DT, Delimont D, Cheung L, Zallocchi M, Sansom SC, Holzclaw JD, et al. Biomechanical strain causes maladaptive gene regulation, contributing to Alport glomerular disease. *Kidney Int*. 2009;76(9):968-76. doi:10.1038/ki.2009.324.

208. Kriz W, Lemley KV. A potential role for mechanical forces in the detachment of podocytes and the progression of CKD. *J Am Soc Nephrol.* 2015;26(2):258-69. doi:10.1681/ASN.2014030278.

209. Kalita J, Kapinos LE, Zheng T, Rencurel C, Zilman A, Lim RY. Karyopherin enrichment and compensation fortifies the nuclear pore complex against nucleocytoplasmic leakage. *J Cell Biol.* 2022;221(3):e202108107. doi:10.1083/jcb.202108107.

210. Hoogenboom BW, Hough LE, Lemke EA, Lim RY, Onck PR, Zilman A. Physics of the nuclear pore complex: Theory, modeling and experiment. *Phys Rep.* 2021;921:1-53. doi:10.1016/j.physrep.2021.03.003.

211. Soto-Ponce A, De Ita M, Castro-Obregón S, Cortez D, Landesman Y, Magaña JJ, et al. Targeting CRM1 for Progeria Syndrome Therapy. *Aging Cell.* 2025;24(5):e14495. doi:10.1111/acel.14495.

212. Uddin MH, Zonder JA, Azmi AS. Exportin 1 inhibition as antiviral therapy. *Drug Discov Today.* 2020;25(10):1775-81. doi:10.1016/j.drudis.2020.06.014.

213. Kashyap T, Murray J, Walker CJ, Chang H, Tamir S, Hou B, et al. Selinexor, a novel selective inhibitor of nuclear export, reduces SARS-CoV-2 infection and protects

the respiratory system *in vivo*. *Antivir Res.* 2021;192:105115. doi:10.1016/j.antiviral.2021.105115.

214. Wu M, Gui H, Feng Z, Xu H, Li G, Li M, et al. KPT-330, a potent and selective CRM1 inhibitor, exhibits anti-inflammation effects and protection against sepsis. *Biochem Biophys Res Commun.* 2018;503(3):1773-9. doi:10.1016/j.bbrc.2018.07.112.

215. Groothof D, Shehab NB, Erler NS, Post A, Kremer D, Polinder-Bos HA, et al. Creatinine, cystatin C, muscle mass, and mortality: Findings from a primary and replication population-based cohort. *J Cachexia Sarcopenia Muscle.* 2024;15(4):1528-38. doi:10.1002/jcsm.13511.

216. Schulz A, Schlesener M, Weiss J, Hänsch J, Wendt N, Kossmehl P, et al. Protective effect of female gender on the development of albuminuria in a polygenetic rat model is enhanced further by replacement of a major autosomal QTL. *Clin Sci.* 2008;114(4):305-11. doi:10.1042/CS20070300.

217. Sun Q, Baues M, Klinkhammer BM, Ehling J, Djudjaj S, Drude NI, et al. Elastin imaging enables noninvasive staging and treatment monitoring of kidney fibrosis. *Sci Transl Med.* 2019;11(486):eaat4865. doi:10.1126/scitranslmed.aat4865.

218. Lesley J, Hyman R, Kincade PW. CD44 and its interaction with extracellular matrix. *Adv Immunol.* 1993;54:271-335. doi:10.1016/s0065-2776(08)60537-4.

219. Eymael J, Sharma S, Loeven MA, Wetzels JF, Mooren F, Florquin S, et al. CD44 is required for the pathogenesis of experimental crescentic glomerulonephritis and collapsing focal segmental glomerulosclerosis. *Kidney Int.* 2018;93(3):626-42. doi:10.1016/j.kint.2017.09.020.

220. Kuppe C, Gröne H-J, Ostendorf T, Van Kuppevelt TH, Boor P, Floege J, et al. Common histological patterns in glomerular epithelial cells in secondary focal segmental glomerulosclerosis. *Kidney Int.* 2015;88(5):990-8. doi:10.1038/ki.2015.116.

Appendix

Supplementary Table 1: Complete list of proteins exhibiting significant age-dependent changes in nuclear-to-cytoplasmic (N/C) ratios in primary mouse podocytes

Gene	W 11 N/C ratio	W 80 N/C ratio	fold change	FDR	Category
Atp5me	0.949	22.083	23.258	0.198	C→N
Ndufb9	0.906	14.292	15.777	0.197	C→N
Rmnd1	0.577	8.527	14.785	0.189	C→N
Ndufa2	0.479	6.100	12.736	0.197	C→N
Mff	0.932	11.079	11.891	0.189	C→N
Ndufc2	0.761	6.591	8.660	0.198	C→N
Cox7c	0.452	3.471	7.687	0.197	C→N
Fam177a1	0.426	3.027	7.101	0.189	C→N
Nme3	0.865	3.291	3.805	0.194	C→N
Sec24c	0.769	2.123	2.762	0.194	C→N
Lgalsl	1.555	0.239	6.513	0.194	N→C
Hbb-b2	4.569	0.712	6.416	0.189	N→C
Alad	1.134	0.189	5.995	0.189	N→C
Nudt5	1.193	0.238	5.006	0.189	N→C
Adss1	1.447	0.302	4.794	0.189	N→C
Macrod1	1.449	0.307	4.711	0.189	N→C
Ces1d	1.084	0.231	4.686	0.194	N→C
Acp1	1.233	0.356	3.466	0.195	N→C
Clpp	1.196	0.350	3.421	0.198	N→C
Arhgdia	1.236	0.367	3.367	0.189	N→C
Sdsl	1.923	0.596	3.226	0.189	N→C
Wdr77	1.236	0.405	3.052	0.189	N→C
Pdxk	1.258	0.413	3.043	0.194	N→C
Brox	1.182	0.389	3.036	0.194	N→C
Irf3	1.002	0.360	2.786	0.198	N→C
Dbi	0.725	0.045	16.056	0.135	C→C

Spr	0.433	0.048	8.945	0.135	C→C
Ldha	0.414	0.047	8.841	0.189	C→C
Ttr	0.736	0.084	8.730	0.194	C→C
Serpinb6b	0.832	0.098	8.513	0.189	C→C
Anxa3	0.800	0.114	7.020	0.189	C→C
Nit2	0.565	0.089	6.328	0.189	C→C
Aamdc	0.551	0.094	5.892	0.189	C→C
Eml2	0.614	0.108	5.675	0.189	C→C
Gmfb	0.360	0.064	5.607	0.189	C→C
Cap1	0.644	0.115	5.577	0.189	C→C
Mdh1	0.548	0.098	5.573	0.135	C→C
Serpinb6	0.983	0.177	5.556	0.189	C→C
Etfb	0.702	0.129	5.424	0.194	C→C
Gtf3c4	0.989	0.191	5.168	0.194	C→C
Pkm	0.659	0.132	4.970	0.189	C→C
Ube2k	0.431	0.094	4.577	0.194	C→C
Gsk3a	0.701	0.153	4.575	0.194	C→C
Gclc	0.611	0.136	4.503	0.189	C→C
Bcat2	0.749	0.166	4.501	0.189	C→C
Aldoa	0.397	0.089	4.479	0.189	C→C
Nit1	0.570	0.130	4.376	0.189	C→C
Ywhaz	0.465	0.106	4.368	0.194	C→C
Cfl1	0.527	0.121	4.362	0.194	C→C
Eif5	0.575	0.133	4.333	0.189	C→C
Kyat3	0.984	0.237	4.149	0.194	C→C
Ak1	0.295	0.072	4.114	0.198	C→C
Pdcd5	0.471	0.116	4.044	0.189	C→C
Npepl1	0.487	0.121	4.013	0.194	C→C
Pgam1	0.524	0.132	3.982	0.189	C→C
Atic	0.464	0.117	3.974	0.189	C→C
Ywhaq	0.589	0.149	3.943	0.195	C→C
Ldhb	0.562	0.143	3.938	0.194	C→C
Ube2v1	0.617	0.159	3.892	0.194	C→C

Otub1	0.653	0.169	3.872	0.189	C→C
Pebp1	0.473	0.123	3.846	0.189	C→C
Crk	0.415	0.108	3.841	0.194	C→C
Ppia	0.458	0.122	3.758	0.194	C→C
Arl3	0.455	0.121	3.750	0.194	C→C
Got1	0.477	0.128	3.722	0.189	C→C
Thop1	0.555	0.149	3.719	0.189	C→C
Uba6	0.437	0.118	3.691	0.194	C→C
Wdr13	0.831	0.228	3.644	0.194	C→C
Pcmt1	0.501	0.138	3.634	0.189	C→C
Impa1	0.619	0.175	3.538	0.189	C→C
Gnpda2	0.548	0.160	3.420	0.195	C→C
Aldh7a1	0.623	0.182	3.419	0.189	C→C
Cpne1	0.294	0.086	3.403	0.194	C→C
Rap1gds1	0.917	0.270	3.402	0.194	C→C
Mthfsl	0.868	0.256	3.391	0.195	C→C
Nif3l1	0.385	0.115	3.355	0.197	C→C
Akr1b10	0.727	0.217	3.347	0.194	C→C
Acyp2	0.644	0.193	3.340	0.198	C→C
Anxa5	0.495	0.149	3.327	0.194	C→C
Sars1	0.248	0.075	3.293	0.189	C→C
Acadsb	0.524	0.160	3.285	0.194	C→C
Plekha2	0.842	0.260	3.236	0.194	C→C
Pgk1	0.390	0.123	3.180	0.189	C→C
Apip	0.584	0.184	3.178	0.194	C→C
Anxa6	0.524	0.165	3.175	0.189	C→C
Gspt1	0.497	0.157	3.172	0.189	C→C
Ephx2	0.544	0.173	3.150	0.194	C→C
Umps	0.897	0.287	3.127	0.189	C→C
Tbcb	0.387	0.125	3.104	0.194	C→C
Prdx5	0.443	0.144	3.069	0.189	C→C
Ranbp1	0.389	0.127	3.056	0.194	C→C
Ahcyl2	0.644	0.216	2.979	0.193	C→C

Ppat	0.664	0.227	2.928	0.194	C→C
Arrb1	0.644	0.225	2.862	0.194	C→C
Aldoc	0.899	0.316	2.843	0.194	C→C
Gpd1l	0.516	0.182	2.840	0.189	C→C
Etf1	0.647	0.229	2.824	0.194	C→C
Ciapin1	0.531	0.193	2.747	0.197	C→C
Nqo1	0.838	0.324	2.586	0.194	C→C
Capn2	0.561	0.217	2.584	0.197	C→C
Mif	0.709	0.279	2.540	0.197	C→C
Atp5if1	1.238	22.791	18.412	0.194	N→N
Vdac1	1.418	17.142	12.087	0.198	N→N
Mpc1	2.130	24.684	11.589	0.197	N→N
Vdac2	1.102	12.601	11.439	0.189	N→N
Cox5b	1.247	14.078	11.287	0.194	N→N
Uqcrc1	1.338	14.312	10.699	0.194	N→N
Ndufb8	1.184	11.855	10.016	0.189	N→N
Chchd3	2.894	26.714	9.230	0.189	N→N
Ghitm	1.667	15.200	9.116	0.197	N→N
Vdac3	1.332	12.092	9.080	0.194	N→N
Ndufb10	1.182	10.640	9.001	0.198	N→N
Mtch1	1.995	16.696	8.370	0.189	N→N
Tomm40	2.280	18.558	8.138	0.189	N→N
Ndufb7	1.222	9.710	7.948	0.189	N→N
Pgam5	1.409	10.586	7.513	0.194	N→N
Maoa	2.171	16.202	7.462	0.189	N→N
Vapb	1.072	7.266	6.776	0.189	N→N
Tomm70	1.205	8.064	6.692	0.194	N→N
Cox4i1	1.427	9.292	6.513	0.194	N→N
Spg7	1.011	6.475	6.405	0.194	N→N
Rhot2	1.500	8.981	5.989	0.198	N→N
Slc25a46	1.811	10.393	5.740	0.197	N→N
Micu1	1.604	8.185	5.103	0.194	N→N
Fut8	1.633	7.653	4.685	0.197	N→N

Nphs2	3.651	15.489	4.243	0.197	N→N
Tdrkh	1.770	7.173	4.053	0.194	N→N
Ssr4	1.688	6.617	3.920	0.195	N→N
Ociad1	1.347	5.241	3.891	0.189	N→N
Fkbp8	1.112	4.229	3.805	0.194	N→N
Chchd6	2.317	8.606	3.715	0.189	N→N
Vapa	1.164	4.248	3.650	0.194	N→N
Clpb	1.415	4.692	3.315	0.194	N→N
Q8K207	1.805	5.333	2.954	0.189	N→N
Itprid2	1.062	2.657	2.503	0.197	N→N

C→N= proteins whose nuclear-to-cytoplasmic ratio increased with age (cytoplasm to nucleus shift); N→C = proteins whose nuclear-to-cytoplasmic ratio decreased with age (nucleus to cytoplasm shift); C→C = proteins that became increasingly enriched in the cytoplasmic fraction with age; N→N = proteins that became increasingly enriched in the nuclear fraction with age.

Acknowledgments

This work has been made possible through the support, guidance, and kindness of many individuals, to whom I would like to express my deepest gratitude.

First and foremost, I extend my sincere thanks to my supervisor, Prof. Dr. rer. nat. Tammo Ostendorf. My doctoral journey began with your willingness to offer me this invaluable opportunity. Over the past five years, you have granted me the freedom to explore my scientific interests while providing unwavering guidance and support. Our weekly Monday meetings-discussing experimental progress, challenges, future plans, and even life beyond the lab-were a constant source of motivation. Your professionalism, optimism, and encouragement helped me through many difficult moments. I am deeply grateful for your trust and everything you have done for me. I also wish to express my heartfelt appreciation to Prof. Dr. phil. nat. Gabriele Pradel for kindly agreeing to serve as my co-supervisor and for her continuous support throughout my studies.

I am also grateful to Univ.-Prof. Dr. rer. nat. Wolfram Antonin and Dr. rer. nat. Mohamed Hamed from the Institute of Biochemistry and Molecular Cell Biology for their valuable contributions to this project.

My sincere thanks go to Priv.-Doz. Dr. rer. nat. Ute Raffetseder. Working with you has truly been a pleasure. Your positivity, warm personality, and genuine care for students created an encouraging and inspiring work environment. Thank you for your guidance and constant support.

I was incredibly fortunate to work alongside wonderful colleagues who filled my daily life with joy, encouragement, and strength. Ina V. Martin, words cannot fully express my gratitude to you. You taught me so many things, especially regarding animal experiments, and you were always there to help me solve problems, often saving me at critical moments. Thank you from the bottom of my heart. My sincere thanks also go to Xiyang Liu, Anna Leitz, Rafaela Rawinski, Jialin Wang, and Yili Chen for your help, for listening to my concerns, and for sharing countless discussions. Our Friday Currywurst and coffee breaks were truly comforting moments during my PhD years. I would also like to thank Susanne Scholz, Stephanie Ludwigs, Dagmar Wieland, Gertrud Minartz, and Mihir Pravinbhai Patel for their excellent technical assistance and, even more importantly, for your many personal acts of kindness. Your help-ranging from offering rides, household

items, and travel tips to birthday cakes and language-learning support-brought warmth into my life far away from home. My gratitude also extends to Astrid Fuß, who, although not part of our group, was always willing to help and consistently did so with exceptional dedication.

I am thankful to my dear friend Yunli Li in China, who always understands me without a word.

My deepest gratitude goes to my parents, Fuying Sun and Shaobao Gao, for their unconditional love and support throughout my life. Even though I moved thousands of kilometers away to pursue my studies, you have always been with me in spirit.

As my five-year doctoral journey now comes to an end, the memories shared with all of you will remain with me forever. Thank you-each of you has made my time in Germany truly special, and because of you, I never felt alone.

Date: 11.12.2025

Signature: Yingying Gao

Declaration of Authorship

I, Yingying Gao declare that this thesis and the work presented in it are my own and has been generated by me as the result of my own original research.

Hiermit erkläre ich an Eides statt / I do solemnely swear that:

1. This work was done wholly or mainly while in candidature for the doctoral degree at this faculty and university;
2. Where any part of this thesis has previously been submitted for a degree or any other qualification at this university or any other institution, this has been clearly stated;
3. Where I have consulted the published work of others or myself, this is always clearly attributed;
4. Where I have quoted from the work of others or myself, the source is always given. This thesis is entirely my own work, with the exception of such quotations;
5. I have acknowledged all major sources of assistance;
6. Where the thesis is based on work done by myself jointly with others, I have made clear exactly what was done by others and what I have contributed myself;

Statement of Contributions

Project conceptualization: Prof. Dr. rer. nat. Wolfram Antonin, Prof. Dr. med. Marcus Johannes Moeller, and Prof. Dr. rer. nat. Tammo Ostendorf.

Supervision: Prof. Dr. rer. nat. Tammo Ostendorf and Prof. Dr. phil. nat. Gabriele Pradel.

Experimentation and investigation: Yingying Gao conducted all animal experiments in both mouse and rat models, including sample collection and analyses of serum, urine, and EDTA samples. She performed all immunohistochemistry (IHC) and immunofluorescence (IF) stainings, carried out the majority of IHC data analyses, and acquired approximately half of the IF imaging data. Dr. rer. nat. Mohamed Hamed contributed to the isolation of primary podocytes from mouse glomeruli. In the rat experiments, he performed in vitro drug treatments and quantitative image-based

analyses, including assessment of nuclear pore complex (NPC) numbers, Nup93 signal intensity, nuclear-to-cytoplasmic ratios of XPO1 and p53, as well as quantification of CD44-positive staining and glomerular area. Dr. rer. nat. Ina Verena Martin provided support during animal experiments.

Technical support: Susanne Scholz, Stephanie Ludwigs, Dagmar Wieland, Gertrud Minartz, Mihir Pravinbhai Patel, and Astrid Fuß.

Data curation: Portions of Methods sections 3.3.1 and 3.3.5, Figures 18, 19, 21, 25-28, and 32, Table 8, and Supplementary Table 1 include work conducted by Dr. rer. nat. Mohamed Hamed. All remaining data curation was performed by Yingying Gao.

Data validation: Yingying Gao, Dr. rer. nat. Mohamed Hamed, Prof. Dr. rer. nat. Tammo Ostendorf, and Prof. Dr. rer. nat. Wolfram Antonin.

Visualization: Yingying Gao.

7. Parts of this work have been published before as:

Gao Y, Hamed M, Martin IV, Raffetseder U, Liu X, Leitz A, et al. The nuclear export inhibitor selinexor improves kidney function in a rat model of focal segmental glomerulosclerosis. Am J Physiol Renal Physiol. 2025;329(4):F496-F509. doi: 10.1152/ajprenal.00143.2025.

Kongress-Abstract:

Gao Y, Hamed M, Martin IV, Raffetseder U, Liu X, Leitz A, et al. Nuclear Export Inhibitor Selinexor Improves Kidney Function in a Rat Model of FSGS: FR-PO0767. Journal of the American Society of Nephrology. 2025;36(10S). doi: 10.1681/ASN.2025vr83fc49.

Date: 19.01.2026

Signature: Yingying Gao